Effects of Impact and Vibration on the Performance of a Micromachined Tuning Fork Gyroscope

by

Robert D. White

Submitted to the Department of Mechanical Engineering
in partial fulfillment of the requirements for the degrees of

Bachelor of Science in Mechanical Engineering

and

Master of Science in Mechanical Engineering

at the

MASSACHUSETTS INSTITUTE OF TECHNOLOGY

June 1999

Author .....
Department of Mechanical Engineering
May 21, 1999

Certified by .....
Marc Weinberg
Group Leader, MEMS Analysis and Test, Draper Laboratory
Thesis Supervisor

Certified by .....
Zaichun Feng
Associate Professor
Thesis Supervisor

Accepted by .....
Ain A. Sonin
Chairman, Department Committee on Graduate Students

Effects of Impact and Vibration on the Performance of a Micromachined Tuning Fork Gyroscope

by

Robert D. White

Submitted to the Department of Mechanical Engineering
on May 21, 1999, in partial fulfillment of the
requirements for the degrees of
Bachelor of Science in Mechanical Engineering
and
Master of Science in Mechanical Engineering

Abstract

This thesis demonstrates that tuning fork gyroscopes are sensitive to mechanical vibration in particular frequency bands, and to narrow impact impulses. A vibration test setup has been developed, allowing delivery of mechanical vibration from 1 kHz-30 kHz at levels up to 50 g_{pk}. Theoretical modeling of the gyro response to vibration and impact is compared with experimental results. Erroneous rate measurements caused by vibration and impact are examined and explained. The maximum allowable levels of vibration and impact that the gyro can safely sustain are determined. Particular sensitivity is seen to vibration at the difference between the antiparallel in-plane and out-of-plane modal frequencies, and to impacts with durations of less that 0.1 ms.

Thesis Supervisor: Marc Weinberg
Title: Group Leader, MEMS Analysis and Test, Draper Laboratory

Thesis Supervisor: Zaichun Feng
Title: Associate Professor

Acknowledgments

This thesis was prepared at The Charles Stark Draper Laboratory, Inc., under Draper Laboratory IR& D/CSR project 18547.

Author .....

Robert D. White

I very much appreciate the help of all of the Draper and MIT staff who have assisted me in this work. I am particularly grateful for the advice, experience, and support extended by my thesis supervisors, Dr. Marc Weinberg, Prof. Zaichun Feng, and Tony Kourepenis. Their insights and instruction were invaluable.

I would like to thank all of the other Draper engineers and technicians who have assisted me. Thanks to Rich Elliott, Dave Hom, Tony Petrovich, and Jon Bernstein for their advice on all sorts of technical issues. I also appreciate the help of Phil Rose, Bill Murphy, Bill Harris, Bobby Fields, and Roy Waggoner in repairing test systems, acquiring parts, and advice. Ed McCormack and Peter Chiacchi helped me greatly with building the test fixtures. Paul Magnussen, Chris Clapp, Mike Cappella and Larry Weldon were always available. Thanks to Nathan St. Michel, Omar Miller, Steve Daley, Eli Weinberg, and Matt Borsini for their encouragement and help. I also very much appreciate the good humor and friendship of all involved.

I am very grateful for the patience and support of my friends and family who always met me with a smile, even when my test systems weren't working and they never heard the end of it.

May God be praised for the beauty and complex order of His creation, and for giving us the ability and opportunity to explore His world.

Contents

List of Figures

List of Tables

Chapter 1

Introduction

Micromachined tuning fork gyroscopes are used to measure rotational rate in various sensing applications. This is accomplished by making use of the Coriolis effects caused by rotation of the gyro with respect to inertial space. In order to exploit the physics, a micromechanical structure consisting of two proof masses constrained by beam flexures is utilized. The dynamics of this mechanical structure, along with the associated control and signal conditioning electronics, constitute the electromechanical system which this thesis examines.

Draper Laboratory's tuning fork gyroscope will be used in environments where it will experience mechanical vibration and impact. One of the aims of gyro design is to ensure that the instrument will survive in these environments, and continue to give accurate readings of rotational rate. The intent of this thesis is to examine the sensitivity of the gyro to mechanical vibration and impact.

Theoretical work presented in section 2.2.1 develops a linear model of gyroscope operation. Testing indicates that the model captures the essential dynamics of the mechanical model, although some nonlinear effects are seen. Measurement of Duffing spring effects in the gyro are undertaken as part of the model development. Although cubic spring terms are seen, they modify flexure stiffness by only approximately 0.14 % at nominal displacement amplitudes, and so can usually be neglected. (section 4.3) The only exception to this is during high amplitude vibration at the motor axis resonant frequencies, where nonlinearities will shift the resonant frequency appreciably.

In addition to spring nonlinearities, Coriolis forces are inherently nonlinear, and must be considered as such. (see section 2.2.3)

In addition to the theoretical work, significant work has gone into the development of experimental systems for vibration and impact testing, as described in chapter 3. Two mechanical shakers were purchased, one low frequency electromagnetic shaker, and one high frequency piezoelectric shaker. Using these systems, it was possible to deliver sinusoidal vibrations from 1 kHz levels throughout the bandwidth of the gyro (as high as 30 kHz). Random vibration excitations were also used for testing. For impact testing, a calibrated hammer was utilized. The hammer includes an internal force sensor and various tips which can be used to deliver different types of impacts.

Construction of the experimental apparatus involved substantial design work. In particular, a major effort was made to create stiff mounting fixtures which would not confuse test results by the addition of unmodeled dynamics. Section 3.3 discusses fixture design.

Two main types of testing were conducted. During open loop testing, the gyro was driven only by applied mechanical excitations. This type of testing allowed verification of the model and measurement of critical model parameters. Each unit used in testing underwent Q tests to determine damping, and vibration tests to determine modal frequencies. Spring nonlinearities were computed by measuring the shift in modal frequency with amplitude. Mismatch in flexure springs was determined, showing a 1 or 2 % mismatch, varying from unit to unit. (section 5.3) Finally, response to random vibration at modal frequencies was determined, as well as response to random vibration in particular bandwidths. This data is used to recommend the maximum allowable vibration which the gyro can safely experience without causing any damage to the structure. See chapter 5 for the results of open loop testing.

Closed loop testing was conducted to determine operational errors caused by impact and vibration. In particular, erroneous signals seen at the gyro rate output were measured, as well as shifts in the rate output mean. Rate output is the signal generated by the gyro which gives an estimate of the rotational rate being experienced.

The gyro was most sensitive to low frequency angular vibration at the difference

between the two antiparallel modal frequencies, which generated substantial motion out of the plane due to Coriolis forcing of the antiparallel mode. Vibration at this frequency will quickly saturate the gyro electronics, and produces some errors on rate out. The gyro was also very sensitive to vibration at the in-plane parallel modal frequency, called the *hula* frequency (see section 2.2.2), which caused AC-out to clip and produced errors on rate out. Sufficiently high vibration levels at the hula frequency cause the gyro to shut down completely. Random vibration also produces erroneous measurements on the gyro rate output, most notably at the differences between the various modal frequencies. (See Chapters 6 and 7).

Impact, similarly, can easily saturate the electronics, and produces errors on rate out at the difference between certain natural frequencies. Impact testing indicates strong dependence of gyro response on the duration of the impact pulse. Impact pulses with durations more than 3 times the natural period of the gyro modes will cause little response. Design of gyro mounting structures will be important in reducing impact response, since structure resonances couple strongly into gyro output. Impact testing is discussed in chapter 8.

This work develops a good understanding of the various errors produced by different types of mechanical vibration and impact. Particularly, levels of vibration and impact which will cause saturation of the electronics, loss of gyro operation, and permanent damage to the device are determined. The dependence of the errors on certain system parameters such as spring mismatch and impulse duration are considered.

Chapter 2 presents background information on the gyro, including mechanical modeling and a description of the gyro electronics. Experimental systems are described in Chapter 3. In Chapter 4, a discussion of characterization testing is pursued, including Q testing and measurement of spring nonlinearities. Chapter 5 discusses open loop vibration testing, and compares results with theory. The maximum safe vibration levels are determined. Chapter 6 enters into a discussion of low frequency closed loop vibration, which is most critical to gyro performance under real environmental conditions. Various error signals are discussed and their sources determined. High frequency vibration effects are considered in Chapter 7, focusing on the effects

of sinusoidal vibration at the hula frequency, which causes the most errors. Chapter 8 discusses impact modeling and test results, showing sensitivity to impact and determining various important factors relating to impact response. Particular detail is given regarding the effects of impact pulse duration. In Chapter 9, a summary of all pertinent results is presented, including important estimates of the levels of mechanical excitation that can be safely sustained.

Chapter 2

Background

This chapter covers the background needed to understand the functioning and testing of the tuning fork gyroscope. The physical layout of the microgyro and its associated systems are described. From this physical description, a mechanical model is developed. This model includes fundamental linear dynamics of the gyro. Coriolis effects, vibration inputs, and nonlinear spring elements are also discussed. In addition to the description of the mechanical subsystems, the electrical subsystems are described. These include the micromachined capacitors used for sensing and driving motion, and the control and signal conditioning electronics. The rest of the thesis will draw heavily on the models and terminology defined in this chapter.

2.1 Physical Description

2.1.1 Microlevel Description

The TFG14 is micromachined from single crystal silicon using standard semiconductor fabrication processes and other micromachining techniques. [1, 4] Figure 2-1 is a microscope picture of the physical device.

The mechanical gyro consists of a few functional parts: the two proof masses, the flexures, the basebeam, the inner and outer motor combs, and the sense plates. Section 2.1.1 describes these different subunits and their various roles. All of the

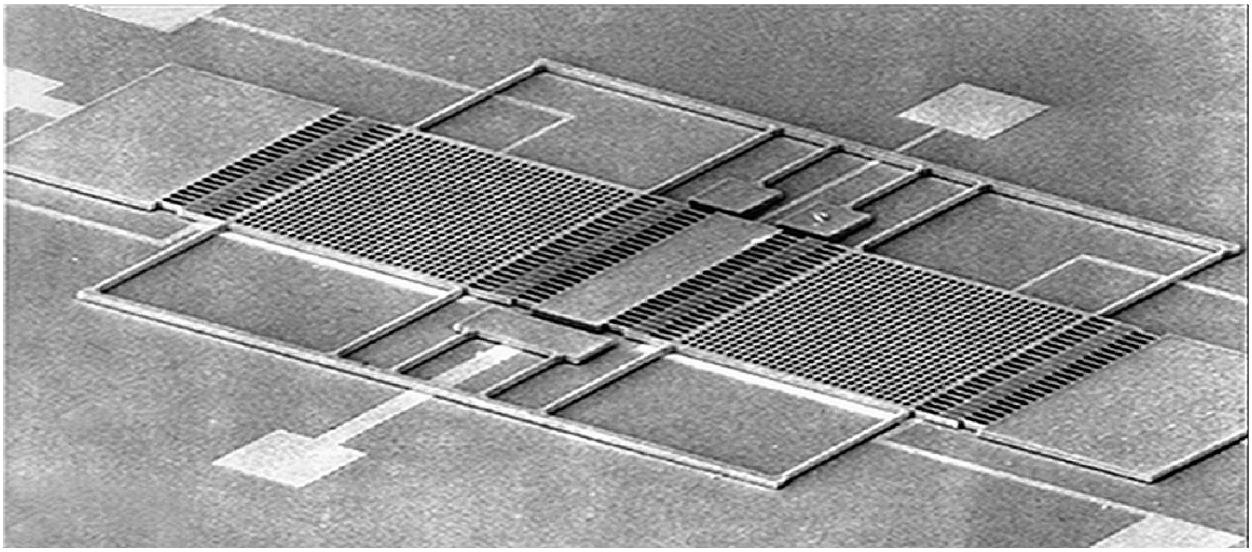

Figure 2-1: Microscope Picture of the Tuning Fork Gyro

structures lie in a single plane, which will be referred to as the *plane of the device*. Motion is possible both in the plane, and perpendicular to the plane of the device. Any such perpendicular motion will be referred to as motion *out of the plane*.

Figures 2-2 and 2-3 give diagrams illustrating the major functional parts of the gyro. The figures also label the three orthogonal directions as *input*, *motor*, and *sense*. These labels will be used throughout this thesis. The names *motor axis* and *drive axis* are used interchangeably.

The two proof masses are plates of silicon through which many square holes have been machined. The masses are physically driven by the gyro system, and create the physics needed to sense rate. The holes exist to allow fluid (usually air) to flow through the proof masses, helping to reduce thin film damping effects. Each proof mass has a mass of approximately $3.6 \cdot 10^{-8}$ kg.

Both proof masses are constrained by flexures, which are beams machined from the silicon wafer. The beams act as springs, bending to allow the proof mass to move both in the plane of the device, and also out of the plane. The beam dimensions determine their stiffness.

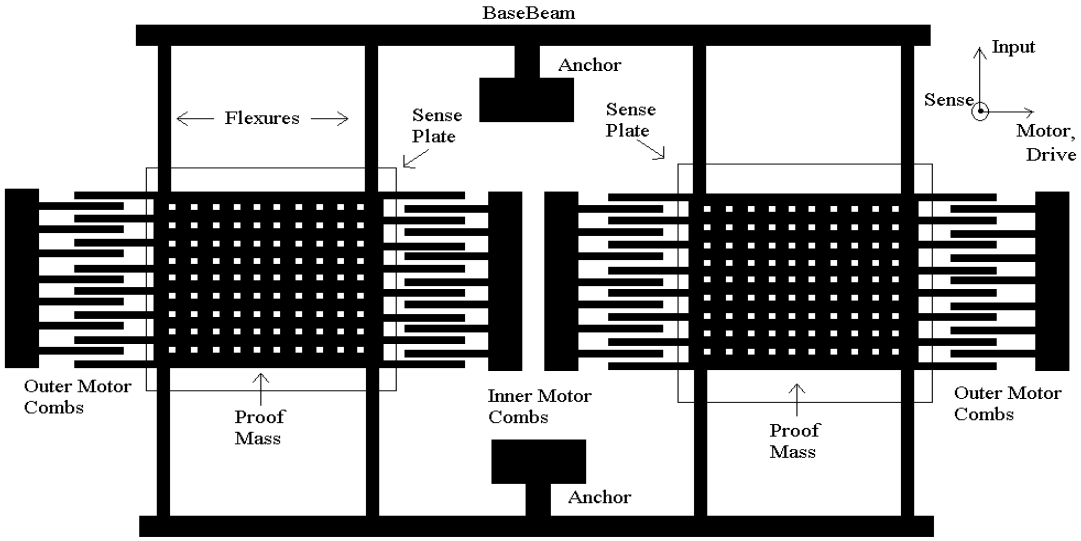

Figure 2-2: Functional Units in the Tuning Fork gyro. Looking down on the plane of the device

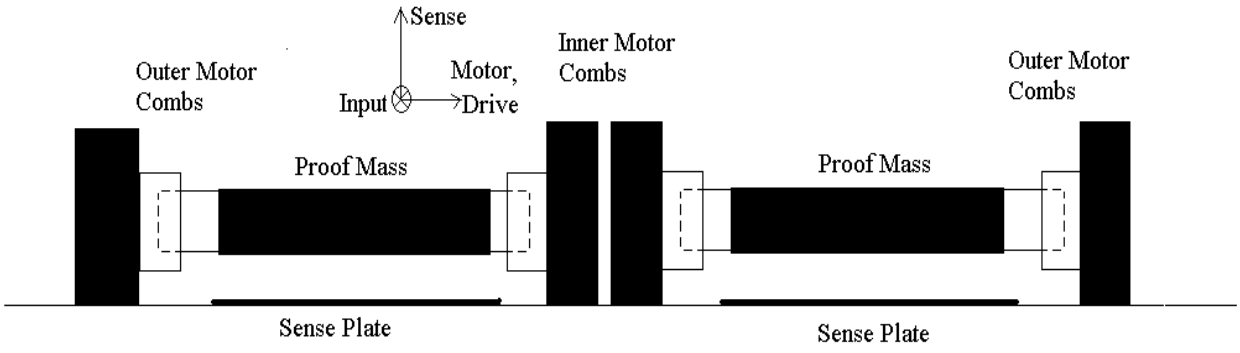

Figure 2-3: Functional Units in the Tuning Fork gyro. View in the plane of the device

Instead of connecting directly to anchors, the flexures connect to a much larger, and thus stiffer, basebeam. The basebeam connects to the substrate at an anchor point, and provides the main support for the gyro structure.

For driving and sensing motion in the plane of the device, the inner and outer motor comb structures are utilized. These structures are anchored directly to the substrate. They consist of a number of long slender fingers which mesh with identical fingers connected to the proof mass. Each side of the proof mass has a set of fingers. Thus, there are 4 sets of interdigitated fingers, two between the masses, and two on the outsides. The interdigitated fingers form capacitors, which allow the gyro to sense and drive motion in the plane.

Below the proof masses there are large, fixed conducting plates, which form a parallel plate capacitor with the proof masses themselves (two capacitors, one for each proof mass). These capacitors are used to sense motion out of the plane.[3]

2.1.2 Packaging and Electronics

The MEMS structure described above is mounted in a lead-less ceramic chip carrier (LCCC). Some LCCC packages are sealed with a vacuum inside, some are left open. When working with an open LCCC, a vacuum pump is used to bring the pressure inside the LCCC down to operating levels.

The LCCC is mounted in a "Kyocera" package, which is approximately 3 cm square. This Kyocera package includes two pre-amplifiers used in sensing in-plane and out-of-plane motion.

The majority of the electronics used in testing gyro operation are housed on the EDM3 board. This board contains the electronics used for readout, driving the gyro, and compensation. The Kyocera package clamps into a "guillotine" connector on the EDM3 board.

The EDM3 board connects via a 21-pin connector and cable to a breakout box. This box receives DC power from a power supply, and has BNC connectors delivering various signals relevant to gyro operation. See figure 3-1 in section 3.1 for a photograph of the EDM3 board and breakout box.

2.2 Mechanical SubSystem

In order to understand gyro operation, a linear mechanical model has been developed. This section describes the derivation of the mechanical model and gives the system matrices in symbolic terms. From the model, the major linear mechanical modes are predicted and defined. A discussion of Coriolis forcing follows, with an accompanying explanation of the mechanism by which the gyro senses rotational rate. After the discussion of the inherently nonlinear Coriolis effects, cubic spring nonlinearities are considered symbolically.

2.2.1 Lumped Element Mechanical Model

Refer to section 2.1.1 for a physical description of the mechanical gyro device, and for definitions of the various terms used here. For theory relating to linear system modeling, consult [5, pp. 13-207] and [7, pp. 439-541]. For a detailed discussion of microgyro modeling, see [3] and [6].

From the physical description, a lumped element mechanical model can be derived. This model deals only with the mechanical properties of the structure; the electrical effects introduced by the capacitors are considered in section 2.3. A number of assumptions are made, drastically reducing the order of the model but still maintaining all essential features of gyro response.

Simplifying assumptions:

1. The proof masses are stiff, and can be considered rigid bodies.

2. The flexures are much stiffer in the input direction than in sense and drive, thus we will assume no motion of the proof masses in the input direction.

3. Due to the translational nature of the excitations experienced by the proof masses, we will assume only translational motion, and not consider rigid body rotation of the proof mass.

4. Electrostatic forces due to DC biasing on the comb drives and the flexure stiffness are together lumped into single linear springs.

5. The basebeam is infinitely stiff. (This assumption is only valid for the low order modes under examination here, for higher order modes compliance of the basebeam is significant.)

6. For motor motion, the basebeam connection to the substrate is assumed to be stiff to rotation, but is given translational compliance.

7. For sense motion, the basebeam connection to the substrate anchor beam is assumed to be infinitely stiff to translation, but to have some torsional compliance, allowing the basebeam to rotate in a rigid fashion about the input axis.

8. Linear damping is assumed. I will assume damping comes from the velocity of the proof mass with respect to the gyro substrate.

Taking these assumptions, there are two directions in which each proof mass can move, giving a total of 4 degrees of freedom, and thus 8 states, for the model. The state variables, therefore, are the position and velocity of each mass in both motor and sense directions. To construct the model, we can consider each axis of motion separately, and then combine the two together, adding appropriate crosscoupling terms.

Figure 2-4 gives a lumped element model for the motor axis alone. Each proof mass is modeled as a mass element, constrained with linear springs and dampers. The flexure spring elements do not connect directly to ground, but rather to the rigid basebeam, which itself connects to ground via the basebeam spring. This spring models the compliance of the basebeam and its anchor structure.

From this lumped element model, the linear motor-axis model can be constructed, which describes motion of the two proof masses in the plane of the device. The following state space representation of the isolated motor axis system is produced. Forcing terms will be considered in section 2.2.3 and 2.2.4. The derivation is carried out in more detail in appendix A.

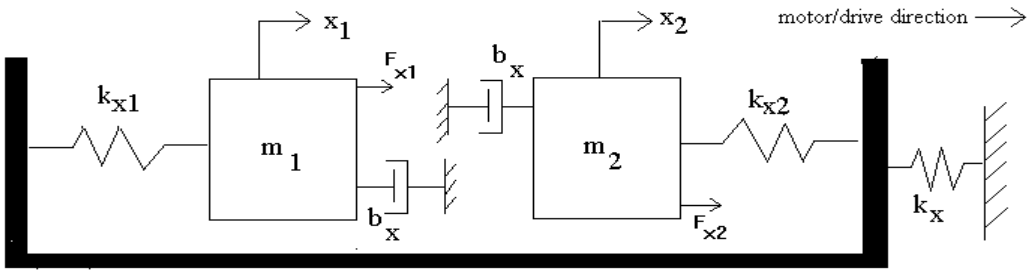

Figure 2-4: Motor Axis Lumped Element Model

$$\frac{d}{dt}\begin{bmatrix} \dot{x_1} \\ x_1 \\ \dot{x_2} \\ x_2 \end{bmatrix} = \begin{bmatrix} -\frac{b_x}{m_1} & \frac{-K_{x11}}{m_1} & 0 & \frac{K_{x12}}{m_1} \\ 1 & 0 & 0 & 0 \\ 0 & \frac{K_{x21}}{m_2} & -\frac{b_x}{m_2} & \frac{-K_{x22}}{m_2} \\ 0 & 0 & 1 & 0 \end{bmatrix} \cdot \begin{bmatrix} \dot{x_1} \\ x_1 \\ \dot{x_2} \\ x_2 \end{bmatrix} \tag{2.1}$$

Where:

$K_{x11} = \frac{k_{x1}k_x + k_{x2}k_{x1}}{k_x + k_{x1} + k_{x2}}$

$K_{x12} = K_{x21} = \frac{k_{x1}k_{x2}}{k_{x1} + k_{x2} + k_x}$

$K_{x22} = \frac{k_{x2}k_x + k_{x2}k_{x1}}{k_x + k_{x1} + k_{x2}}$

The situation for the sense axis is more complex. Again, we will model the proof masses as mass elements, constrained by linear springs. These springs attach to the rigid basebeam, which connects to ground via a torsional spring. The lumped element model is diagrammed in figure 2-5.

From this lumped element model, the state space representation of the sense axis system is derived. The torsional spring stiffness, k_θ is in units of $[N \cdot m/radian]$.

The system equations are given by equation 2.2. Again, forcing terms are not included, they will be considered later in sections 2.2.3 and 2.2.4. The model derivation is carried out in detail in appendix A.

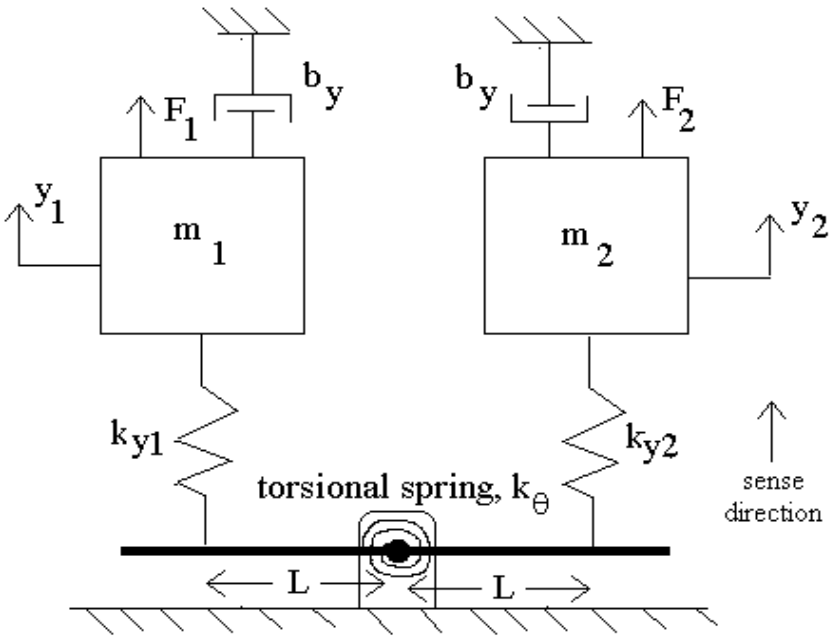

Figure 2-5: Sense Axis Lumped Element Model

$$\frac{d}{dt}\begin{bmatrix} \dot{y_1} \\ y_1 \\ \dot{y_2} \\ y_2 \end{bmatrix} = \begin{bmatrix} -\frac{b_y}{m_1} & \frac{-K_{y11}}{m_1} & 0 & \frac{K_{y12}}{m_1} \\ 1 & 0 & 0 & 0 \\ 0 & \frac{K_{y21}}{m_2} & -\frac{b_y}{m_2} & \frac{-K_{y22}}{m_2} \\ 0 & 0 & 1 & 0 \end{bmatrix} \cdot \begin{bmatrix} \dot{y_1} \\ y_1 \\ \dot{y_2} \\ y_2 \end{bmatrix} \tag{2.2}$$

Where:

$K_{y11} = \frac{k_{y1}k_\theta + L^2 k_{y1}k_{y2}}{k_\theta + L^2(k_{y1}+k_{y2})}$

$K_{y12} = K_{y21} = \frac{-L^2 k_{y1}k_{y2}}{k_\theta + L^2 k_{y1} + L^2 k_{y2}}$

$K_{y22} = \frac{k_{y2}k_\theta + L^2 k_{y2}k_{y1}}{k_\theta + L^2(k_{y1}+k_{y2})}$

Equations 2.1 and 2.2 can be combined to produce a dual axis linear gyro model. This model also includes crosscoupling terms which link motion from one axis to motion of the other axis. Equation 2.3 gives the full system matrix:

$$\frac{d}{dt}\begin{bmatrix} \dot{x_1} \\ x_1 \\ \dot{x_2} \\ x_2 \\ \dot{y_1} \\ y_1 \\ \dot{y_2} \\ y_2 \end{bmatrix} = \left[\begin{array}{cccc|cccc} -\frac{b_x}{m_1} & \frac{-K_{x11}}{m_1} & 0 & \frac{K_{x12}}{m_1} & \frac{b_{xy1}}{m_1} & \frac{k_{xy1}}{m_1} & 0 & 0 \\ 1 & 0 & 0 & 0 & 0 & 0 & 0 & 0 \\ 0 & \frac{K_{x21}}{m_2} & -\frac{b_x}{m_2} & \frac{-K_{x22}}{m_2} & 0 & 0 & \frac{b_{xy2}}{m_2} & \frac{k_{xy2}}{m_2} \\ 0 & 0 & 1 & 0 & 0 & 0 & 0 & 0 \\ \hline \frac{b_{xy1}}{m_1} & \frac{k_{xy1}}{m_1} & 0 & 0 & -\frac{b_y}{m_1} & \frac{-K_{y11}}{m_1} & 0 & \frac{K_{y12}}{m_1} \\ 0 & 0 & 0 & 0 & 1 & 0 & 0 & 0 \\ 0 & 0 & \frac{b_{xy2}}{m_2} & \frac{k_{xy2}}{m_2} & 0 & \frac{K_{y21}}{m_2} & -\frac{b_y}{m_2} & \frac{-K_{y22}}{m_2} \\ 0 & 0 & 0 & 0 & 0 & 0 & 1 & 0 \end{array}\right] \cdot \begin{bmatrix} \dot{x_1} \\ x_1 \\ \dot{x_2} \\ x_2 \\ \dot{y_1} \\ y_1 \\ \dot{y_2} \\ y_2 \end{bmatrix} \tag{2.3}$$

Where all the spring constants are as defined above for equations 2.1 and 2.2.

The linear model presented in equation 2.3 will be used throughout this document. Most of my predictions are based on it. Sections 2.2.3 and 2.2.4 outline the various types of inputs to the mechanical model.

2.2.2 Gyro Normal Modes

From the linear model presented in equation 2.3, the system modes can be computed. Again, simplifying assumptions are made:

1. The two proof masses are the same mass. This is the aim of the fabrication process, and although there is some mismatch in the masses, it should be small.

2. The flexures are symmetrical; thus the linear spring constants $k_{x1} = k_{x2}$ and $k_{y1} = k_{y2}$. Again, this is the aim of the fabrication process, and there will always be some small spring mismatch.

3. Crosscoupling terms (b_{xy}, k_{xy}) between the motor and sense axes are small, and will be neglected in the computation of normal modes.

4. Damping is small (b_x, b_y) and will not affect the mode shapes or model frequencies appreciably. (For these devices Q=10,000-200,000)

Assumption # 3 decouples the two axes, so again we can consider the motor axis modes and the sense axis modes separately. Neglecting damping and assuming perfectly balanced springs and masses produces the following simplified motor model (where $k_{xf} = k_{x1} = k_{x2}$ is the flexure stiffness, and $m = m_1 = m_2$):

$$\frac{d}{dt}\begin{bmatrix} \dot{x_1} \\ x_1 \\ \dot{x_2} \\ x_2 \end{bmatrix} = \begin{bmatrix} 0 & \left(\frac{-k_{xf}^2 - k_x k_{xf}}{k_x + 2k_{xf}}\right) \cdot \frac{1}{m} & 0 & \left(\frac{k_{xf}^2}{2k_{xf} + k_x}\right) \frac{1}{m} \\ 1 & 0 & 0 & 0 \\ 0 & \left(\frac{k_{xf}^2}{2k_{xf} + k_x}\right) \frac{1}{m} & 0 & \left(\frac{-k_{xf}^2 - k_x k_{xf}}{k_x + 2k_{xf}}\right) \cdot \frac{1}{m} \\ 0 & 0 & 1 & 0 \end{bmatrix} \cdot \begin{bmatrix} \dot{x_1} \\ x_1 \\ \dot{x_2} \\ x_2 \end{bmatrix} \tag{2.4}$$

From this, we can compute the four eigenvalues of the system matrix:

$$\begin{bmatrix} j\sqrt{\frac{k_{xf}}{m}} \\ -j\sqrt{\frac{k_{xf}}{m}} \\ j\sqrt{\frac{k_x k_{xf}}{m(2k_{xf}+k_x)}} \\ -j\sqrt{\frac{k_x k_{xf}}{m(2k_{xf}+k_x)}} \end{bmatrix} \tag{2.5}$$

As expected, the eigenvalues are pure imaginary (no damping), and come in conjugate pairs. Thus, there are two eigenfrequencies for the motor axis. Each of these corresponds to an eigenmode. Computing the eigenvectors of the system matrix in equation 2.4, we get, for eigenvalues 1 and 2, the repeated eigenvector:

$$\begin{bmatrix} 1 \\ 0 \\ -1 \\ 0 \end{bmatrix}$$

For eigenvalues 3 and 4, the repeated eigenvector is:

$$\begin{bmatrix} 1 \\ 0 \\ 1 \\ 0 \end{bmatrix}$$

For the tuning fork gyro, the modes are given names: *tuning fork mode* refers to the antiparallel eigenmode described by the first eigenvalue/eigenvector pair. *Hula mode* refers to the parallel eigenmode described by the second eigenvalue/eigenvector pair.

An identical derivation produces the sense axis modes, which also have names. The antiparallel mode is called the *sense mode*, and the parallel mode is called the *out of plane mode*. Again, let

$k_y = k_{y1} = k_{y2}$ and $m = m_1 = m_2$

Then the eigenvalues of the sense axis system matrix (defining the modal frequencies) are:

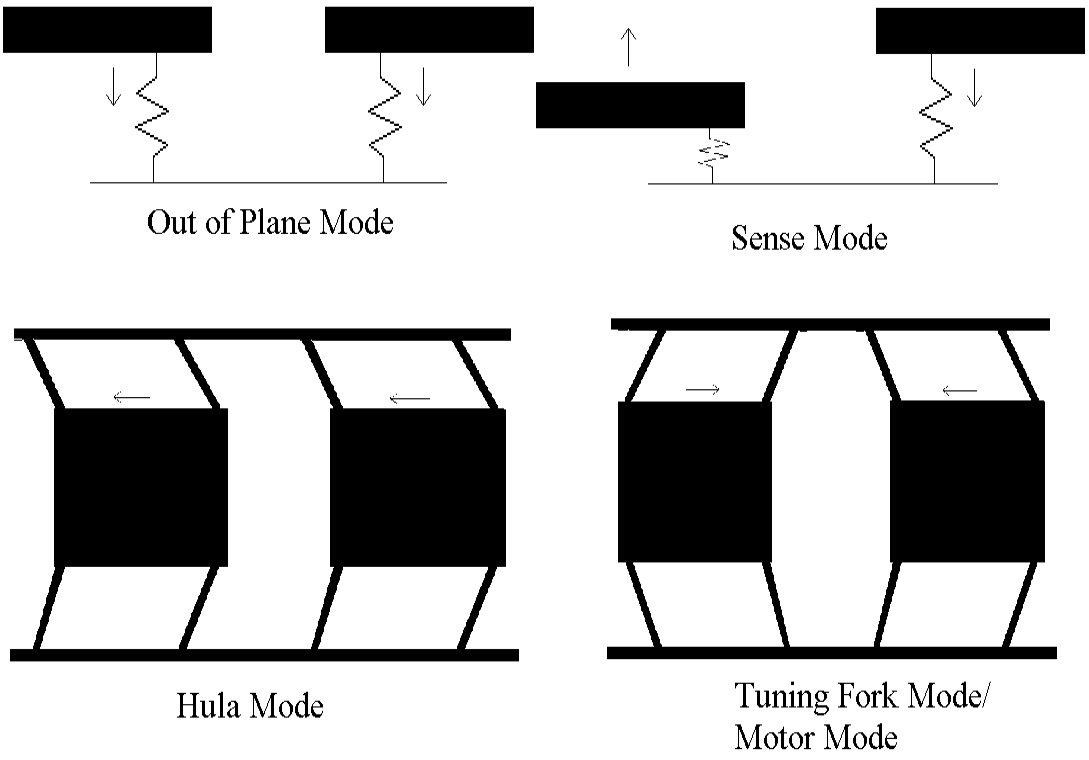

Figure 2-6: Four Major Gyro Modes

$$\begin{bmatrix} j\sqrt{\frac{k_y}{m}} \\ -j\sqrt{\frac{k_y}{m}} \\ j\sqrt{\frac{k_\theta k_y}{(k_\theta+2L^2k_y)m}} \\ -j\sqrt{\frac{k_\theta k_y}{(k_\theta+2L^2k_y)m}} \end{bmatrix} \tag{2.6}$$

Figure 2-6 depicts the motion of each of the four major gyro modes.

During testing, the gyro modal frequencies can be measured. Using this information, it is possible to compute values for k_x, k_{xf}, k_y, and k_θ. Note that any compliance in the basebeam, which was assumed to be infinitely stiff in assumption # 5 above, is lumped in with the various spring constants. Now, with the matched springs and masses assumption used above in equations 2.6 and 2.5, we can set the eigenfrequencies equal to the modal frequencies, producing the relationships relating

mass and spring values to modal frequencies. These relationships, which are used for computing model parameters for each unit, are are given in equations 2.7 through 2.10,

$$k_{xf} = 4\pi^2 f_{tf}^2 \bar{m} \tag{2.7}$$

$$k_x = \frac{8\pi^2 f_{hula}^2 \bar{m}}{1 - 4\pi^2 f_{hula}^2 \frac{\bar{m}}{k_{xf}}} \tag{2.8}$$

$$\bar{k_y} = 4 \cdot f_{oop}^2 \pi^2 \bar{m} \tag{2.9}$$

$$k_\theta = \frac{8\pi^2 L^2 \bar{m} f_{oop}^2 f_{sense}^2}{f_{oop}^2 - f_{sense}^2} \tag{2.10}$$

It is difficult to determine how much the springs are mismatched, so I will use the above relationships to determine parameter values. When it does become necessary to examine spring or mass mismatch (the springs tend to be more mismatched than the masses), I will assume some percentage mismatch and move the two springs apart from the average value computed above. This is done using the relationship in equation 2.11,

$$\begin{aligned} \tfrac{\Delta K}{K} &= \text{mismatch} \\ K_1 &= \bar{K} + \Delta K \\ K_2 &= \bar{K} - \Delta K \end{aligned} \tag{2.11}$$

Except where explicitly mentioned, I will assume perfectly matched springs and masses.

2.2.3 Coriolis Acceleration and Rate Sensing

In order to sense rotational rate, the gyroscope makes use of the Coriolis effect. This is an acceleration in the frame of the device, created by rotation of the entire gyroscope with respect to inertial space. The expression for Coriolis acceleration is,

$$\vec{A}_{Coriolis} = 2\vec{\Omega} \times \vec{v} \tag{2.12}$$

Where:

$\vec{v}$ is the velocity of some object with respect to the frame of the gyroscope.

$\vec{\Omega}$ is the rate of rotation of the frame of the gyroscope with respect to inertial space.

$\vec{A}_{Coriolis}$ is the acceleration of the object with respect to the frame of the gyroscope

See [7, pp. 90-107] for a thorough discussion on coriolis acceleration terms.

The aim of the gyroscope is to accurately determine the rotational rate Ω. During operation, the gyro is driven, using the electrostatic forces generated by the outer motor combs, at the tuning fork frequency. This excites the tuning fork mode. (see figure 2-7). Now, if the gyro experiences a rotation $\vec{\Omega}$, a Coriolis acceleration is produced on the two proof masses, as described by equation 2.12. This acceleration is perpendicular to both the rate vector and the velocity vector. The gyro is most sensitive, in this mode of operation, to rate about the *input axis* (see figures 2-2 and 2-3). Since the tuning fork mode has a velocity in the *motor axis* direction, the Coriolis acceleration is produce in the *sense direction*, which is out of the plane of the device. (see figures 2-2 and 2-3) See [3] for a description of gyro Coriolis physics.

This Coriolis acceleration causes the proof masses to move out of the plane. By sensing out-of-plane motion, it is possible to compute the input rate, Ω. Figure 2-7 depicts the situation during normal gyro operation.

The velocities $\dot{x_1}$ and $\dot{x_2}$ are sinusoidal at the tuning fork frequency. They are also 180 degrees out of phase with each other. Thus, for a time invariant rate, Ω, the Coriolis accelerations will also be oscillatory at the tuning fork frequency, and out of phase with each other. So, while one proof mass is accelerating downwards towards the substrate, the other is accelerating away, and vice versa. This oscillatory motion has the same shape as the sense mode depicted in figure 2-6. However, since we are

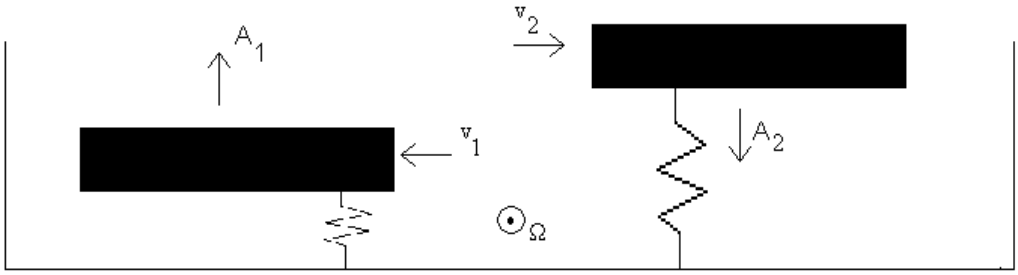

Figure 2-7: Coriolis Acceleration During Normal Gyro Operation

exciting it with an acceleration at the tuning fork frequency, the sense motion will be at the tuning fork frequency, not at the sense frequency.

Now, if the input rate also varies, the situation becomes more complex. However, equation 2.12 always holds. We know that multiplication of two sinusoids produces power at sum and difference frequencies (called *sidebands*):

$$\sin(\omega_1 t)\sin(\omega_2 t) = \frac{1}{2}\cos((\omega_1+\omega_2)t) - \frac{1}{2}\cos((\omega_1-\omega_2)t) \tag{2.13}$$

Thus, an oscillatory input rate, $\Omega(t)$, will produce oscillatory accelerations $A_1(t)$ and $A_2(t)$ with power in the two sidebands. One component will be at the difference frequency, $\omega_{tunefork} - \omega_{rate}$, and one at the sum $\omega_{tunefork} + \omega_{rate}$. This results will become important later on. The situation is described fully in equation 2.14, where we take $\vec{\Omega}(t)$ as the component of rotation perpendicular to the oscillatory tuning fork velocity $\vec{v}(t)$.

$$\begin{aligned} \Omega(t) &= A\sin(\omega_{rate}t) \\ &\textit{and} \\ \vec{A}_{Coriolis} &= 2\vec{\Omega}\times\vec{v}(t) \\ &= 2A\sin(\omega_{rate}t)\times B\sin(\omega_{tunefork}t) \end{aligned}$$

$$A_{Coriolis} = AB\cos((\omega_{tunefork} + \omega_{rate})t) - AB\cos((\omega_{tunefork} - \omega_{rate})t) \quad (2.14)$$

2.2.4 Vibration as an Input to the Linear Model

The intent of this thesis is to determine the sensitivity of the gyro to applied vibration and impact. This section adds vibration of the substrate as an input to the linear model. Taking the state space representation of equation 2.3, we can allow the substrate to translate. Note that all translations (x_1, x_2, y_1, y_2) and their derivatives, as defined in equation 2.1 and 2.2 are defined relative to inertial space. Gyro outputs, however, give the displacement relative to the gyro substrate. Since the substrate is now allowed to translate with respect to inertial space, we need to define a new set of relative displacements:

$$\begin{aligned} x_{1rel} &= x_1 - x_{ss} \\ x_{2rel} &= x_2 - x_{ss} \\ y_{1rel} &= y_1 - y_{ss} \\ y_{2rel} &= y_2 - y_{ss} \end{aligned} \quad (2.15)$$

In addition to the transformation of variables, inputs will be added to the model. Most significantly, acceleration of the substrate in both motor and sense directions will be allowed as an input. These are the first two inputs. Then, additional forces will be allowed on each proof mass, in both the sense and motor directions. Finally, a Coriolis acceleration input (see section 2.2.3) will be added. The Coriolis acceleration is an acceleration input that acts to move both masses in the sense direction in opposite directions. This gives a total of 7 inputs: acceleration of the substrate in both sense and motor directions, 2 additional forces (one sense directed, one motor directed)on each mass, and Coriolis acceleration due to rotation. With these inputs, the state space representation can be formed. Equation 2.16 gives the full system model.

$$\frac{d}{dt}\begin{bmatrix} \dot{x}_{1rel} \\ x_{1rel} \\ \dot{x}_{2rel} \\ x_{2rel} \\ \dot{y}_{1rel} \\ y_{1rel} \\ \dot{y}_{2rel} \\ y_{2rel} \end{bmatrix} = [A] \cdot \begin{bmatrix} \dot{x}_{1rel} \\ x_{1rel} \\ \dot{x}_{2rel} \\ x_{2rel} \\ \dot{y}_{1rel} \\ y_{1rel} \\ \dot{y}_{2rel} \\ y_{2rel} \end{bmatrix} + [B] \cdot \begin{bmatrix} a_{xs} \\ a_{ys} \\ F_{x1} \\ F_{x2} \\ F_{y1} \\ F_{y2} \\ A_{Coriolis} \end{bmatrix} \tag{2.16}$$

Where A is the system matrix, given in equation 2.17, and B is the input matrix, given in equation 2.18. Defining the symbols used:

a_{xs} = acceleration of substrate in the motor direction

a_{ys} = acceleration of substrate in the sense direction

F_{x1}, F_{x2}, F_{y1}, and F_{y2} are additional forces on proof masses 1 and 2 in the sense (y) and motor (x) directions.

$A_{Coriolis}$ is the Coriolis acceleration produced in the sense direction by input rate, as described in section 2.2.3.

All spring constants, K_*, are as defined above for equations 2.1 and 2.2.

Then the state matrix is,

$$A = \left[\begin{array}{cccc|cccc} -\frac{b_x}{m_1} & \frac{-K_{x11}}{m_1} & 0 & \frac{K_{x12}}{m_1} & \frac{b_{xy1}}{m_1} & \frac{k_{xy1}}{m_1} & 0 & 0 \\ 1 & 0 & 0 & 0 & 0 & 0 & 0 & 0 \\ 0 & \frac{K_{x21}}{m_2} & -\frac{b_x}{m_2} & \frac{-K_{x22}}{m_2} & 0 & 0 & \frac{b_{xy2}}{m_2} & \frac{k_{xy2}}{m_2} \\ 0 & 0 & 1 & 0 & 0 & 0 & 0 & 0 \\ \hline \frac{b_{xy1}}{m_1} & \frac{k_{xy1}}{m_1} & 0 & 0 & -\frac{b_y}{m_1} & \frac{-K_{y11}}{m_1} & 0 & \frac{K_{y12}}{m_1} \\ 0 & 0 & 0 & 0 & 1 & 0 & 0 & 0 \\ 0 & 0 & \frac{b_{xy2}}{m_2} & \frac{k_{xy2}}{m_2} & 0 & \frac{K_{y21}}{m_2} & -\frac{b_y}{m_2} & \frac{-K_{y22}}{m_2} \\ 0 & 0 & 0 & 0 & 0 & 0 & 1 & 0 \end{array}\right] \tag{2.17}$$

And the input matrix is,

$$B = \begin{bmatrix} -1 & 0 & \frac{1}{m_1} & 0 & 0 & 0 & 0 \\ 0 & 0 & 0 & 0 & 0 & 0 & 0 \\ -1 & 0 & 0 & \frac{1}{m_2} & 0 & 0 & 0 \\ 0 & 0 & 0 & 0 & 0 & 0 & 0 \\ 0 & -1 & 0 & 0 & \frac{1}{m_1} & 0 & 1 \\ 0 & 0 & 0 & 0 & 0 & 0 & 0 \\ 0 & -1 & 0 & 0 & 0 & \frac{1}{m_2} & -1 \\ 0 & 0 & 0 & 0 & 0 & 0 & 0 \end{bmatrix} \tag{2.18}$$

From the state space representation of equation 2.16, transfer functions relating the relative motion of one proof mass to the substrate can be derived. One particularly useful result is the transfer function from substrate vibration to displacement of one mass. Assuming that the two masses are matched, $m_1 = m_2 = m$, then the following transfer functions can be derived.

$$\frac{X_1}{A_{sx}} = \frac{-m^2 s^2 - b_x m s + m(-K_{x22} - K_{x12})}{m^2 s^4 + 2b_x m s^3 + (b_x^2 + mK_{x11} + mK_{x22})s^2 + b_x(K_{x11} + K_{x22})s - K_{x12}^2 + K_{x11}K_{x22}} \tag{2.19}$$

Where:

X_1 is the Laplace transform of the displacement of the left proof mass in the motor direction relative to the gyro substrate

A_{sx} is the Laplace transform of the acceleration of the substrate in the motor direction relative to inertial space

s is the Laplace transform of $\frac{d}{dt}$

In the case of no spring mismatch, $k_{x1} = k_{x2} = k_{xf}$, and equation 2.19 reduces to

$$\frac{X_1}{A_{sx}} = \frac{-m}{ms^2 + b_x s + \frac{k_{xf}k_x}{k_x + 2k_{xf}}} \tag{2.20}$$

For the sense axis,

$$\frac{Y_1}{A_{sy}} = \frac{-m^2s^2 - b_y ms + m(-K_{y22} - K_{y12})}{m^2s^4 + 2b_y ms^3 + (b_y^2 + mK_{y11} + mK_{y22})s^2 + b_y(K_{y11} + K_{y22})s - K_{y12}^2 + K_{y11}K_{y22}} \tag{2.21}$$

Where:

Y_1 is the Laplace transform of the position of the left proof mass in the sense direction relative to the gyro substrate

A_{sy} is the Laplace transform of the acceleration of the substrate in the sense direction with respect to inertial space

In the case of no spring mismatch, $k_y = k_{y1} = k_{y2}$, and equation 2.21 reduces to

$$\frac{Y_1}{A_{sy}} = \frac{-m}{ms^2 + b_y s + k_y} \tag{2.22}$$

2.2.5 Nonlinear Springs

So far, the model has only considered the Coriolis nonlinearity. Another nonlinearity seen in gyro operation is cubic spring terms. Cubic springs describe spring stiffening or softening effects caused by high amplitudes of motion. Spring softening is caused by the electrostatic capacitor forces, while stiffening is caused by large deflection mechanical beam effects.

The basic cubic spring expression is:

$$F = -kx - k_3x^3 \tag{2.23}$$

Now, if we have a mass-spring system undergoing some sinusoidal motion,

$$x = X\sin(t)$$

then

$$\begin{aligned} F &= -kx - k_3 x^3 \\ &= -kX\sin(t) - k_3 X^3 \sin^3(t) \\ &= -kX\sin(t) - k_3\left(\frac{3}{4}X^3\sin(t) - \frac{1}{4}X^3\sin(3t)\right) \\ &= -(kX + \frac{3k_3X^3}{4})\sin(t) + \frac{k_3X^3}{4}\sin(3t) \end{aligned} \tag{2.24}$$

Assuming that we are moving near resonance, we can neglect the higher harmonic at $3t$, which means that the effective linearized stiffness at this amplitude of motion is

$$\begin{aligned} k_{lin} &= \frac{F}{-x} \\ &= \frac{\left(kX + \frac{3k_3X^3}{4}\right)\sin(t)}{X\sin(t)} \\ &= k + \frac{3k_3X^2}{4} \end{aligned} \tag{2.25}$$

Thus, the nonlinear term moves the resonant frequency by changing k_{lin}:

$$\omega_n = \sqrt{\frac{k_{lin}}{m}} = \sqrt{\left(\frac{k + \frac{3k_3X^2}{4}}{m}\right)} \tag{2.26}$$

where k_{lin} is the linearized stiffness about the amplitude of motion X. If we expand this as a series in X^2, neglecting higher order terms in X^2,

$$\begin{aligned} \omega_n &= \omega_n|_{X^2=0} + \left.\frac{\partial\omega_n}{\partial\left(X^2\right)}\right|_{X^2=0} X^2 + \frac{1}{2}\left.\frac{\partial^2\omega_n}{\partial\left(X^2\right)^2}\right|_{X^2=0} X^2 + \cdots \\ &= \sqrt{\frac{k}{m}} + \frac{1}{2}\left(\frac{k + \frac{3}{4}k_3X^2}{m}\right)^{-\frac{1}{2}}\Bigg|_{X^2=0} \frac{3}{4m}k_3 \cdot X^2 + \cdots \\ &= \sqrt{\frac{k}{m}} + \frac{3}{8m}\sqrt{\frac{m}{k}}k_3X^2 + \cdots \end{aligned} \tag{2.27}$$

So, we should see a linear relationship between the natural frequency ω_n in $radians/s$ and the amplitude squared, X^2, in m^2. Tests of frequency dependence

on amplitude have been conducted. The results, summarized in section 4.3, indicate that the nonlinear spring terms are small, but can be important when trying to drive at the resonant frequency. The high Q of the gyro produces very narrow resonant peaks in the frequency response. Thus, even a small nonlinearity can shift the sensitive frequency band for the device noticeably.

2.3 Electrical SubSystem

The electrical subsystem of the tuning fork gyro can be divided into three main sections: the intrinsic capacitance built into the microstructure, the preamplifiers contained with the gyro in the Kyocera package, and the control and readout electronics housed on the EDM3 board. (see section 2.1.2)

2.3.1 Micromachined Capacitors

There are two types of micromachined capacitors in the tuning fork gyro: interdigitated combs, and parallel plates. Interdigitated comb drives are used to drive and sense motion of the proof mass in the plane of the device (see figure 2-2). Figure 2-8 gives a magnified picture of a section of the comb drive. For a discussion of the electrostatics of parallel plate capacitors, see [2, p. 679].

The capacitance between the two sides is given in equation 2.28,

$$C = 2N\frac{\epsilon_0 A}{g} = 2N\frac{\epsilon_0 lh}{g} \tag{2.28}$$

Where:

N = number of fingers extending from one side of a single proof mass (Note that each comb drive capacitor can therefore be considered as consisting, neglecting fringing effects, of 2N parallel plate capacitors, one for each side of every given proof mass finger)

ϵ_0 = permittivity of free space

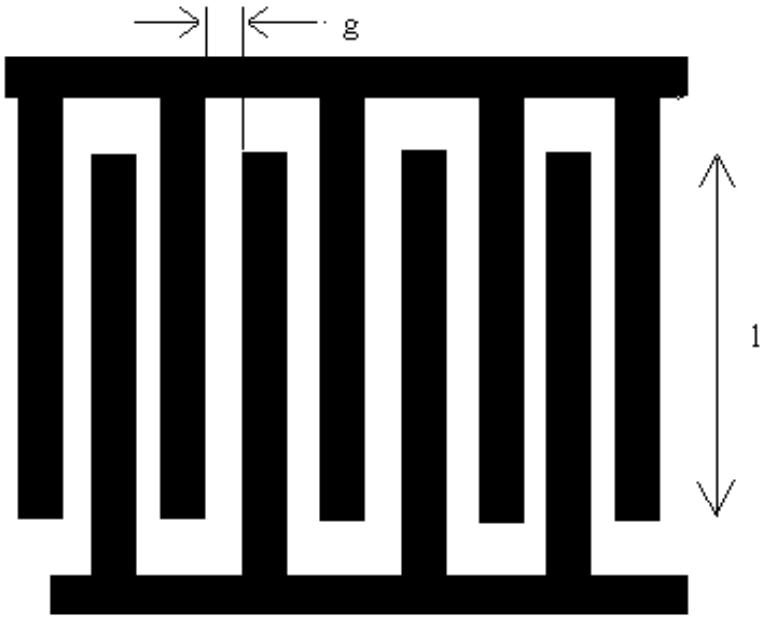

Figure 2-8: Interdigitated Comb Drive Capacitor

A = area of finger overlap

g = gap between fingers

l = length of finger overlap

h = height of finger overlap (thickness out of the plane)

The comb drive capacitors are used to both sense and drive motion in the plane, as discussed in sections 2.3.2 and 2.3.3. For motion out of the plane, the sense parallel plate capacitor is used. Here, the capacitance is between the proof mass, acting as one parallel plate, and a conducting area in the substrate below the proof mass. A parallel plate capacitor has capacitance:

$$C = \frac{\epsilon_0 A}{g} \tag{2.29}$$

Where:

ϵ_0 = permittivity of free space

A = area of parallel plates

g = gap between plates

As discussed in section 2.1.1, the micromechanical structure itself includes 6 capacitors, 3 on each proof mass. Two of these three are comb drives (inner and outer motor combs), and the other is the sense parallel plate capacitor.

2.3.2 Capacitive Sensing

The inner motor combs and the sense plates are used for sensing motion of the proof mass. From figure 2-8 it can be seen that pushing the combs together or pulling them apart will change the finger overlap, l, and thereby change the capacitance. (equation 2.28) Similarly, changing the sense gap (the gap between the parallel plates of the sense capacitor) will change the sense capacitance according to equation 2.29.

These changes in capacitance can be used to sense motion of the proof mass. The constitutive equation for a capacitor is:

$$I = \frac{d}{dt}(CV) = \left(C\frac{\partial V}{\partial t} + V\frac{\partial C}{\partial t}\right) \tag{2.30}$$

For sensing applications, the voltage across the capacitor, V, is held at some DC level, V_{bias}. Thus, $\frac{\partial V}{\partial t} = 0$, and so $I = V_{bias}\frac{\partial C}{\partial t}$. This current flows into a preamp configured as an integrator, as shown in figure 2-9, which produces an output voltage proportional to the integral of the current. Thus, the preamp output voltage depends on the motion of the proof mass, according to equation 2.31,

$$\begin{aligned} V_{out} &= \frac{1}{C_{fb}}\int I\ dt \\ &= \frac{1}{C_{fb}}\int V_{bias}\frac{\partial C}{\partial y}\cdot\frac{dy}{dt}\ dt \\ &= \frac{V_{bias}}{C_{fb}}\int \frac{\partial C}{\partial y}\ dy \end{aligned} \tag{2.31}$$

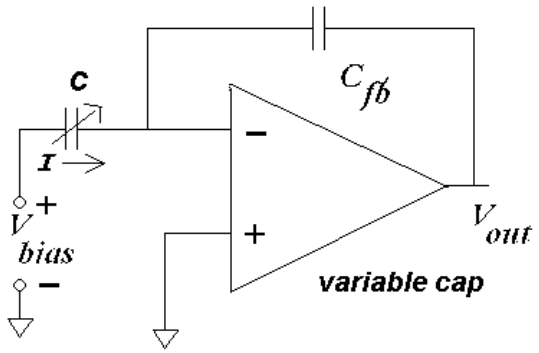

Figure 2-9: Sense Axis Preamp Configuration for Capacitive Sensing

Figure 2-10 presents a capacitive model of the gyro electrostatics. Each proof mass is an electrical node, with three capacitors connecting to it: the outer motor comb, the parallel plate sense capacitor, and the inner motor comb. The outer motor combs are used for creating an electrostatic drive force on the proof masses, and will be considered in section 2.3.3.

The sense capacitors, as described above, change capacitance due to proof mass motion out of the plane. Due to the DC bias on the sense plates, this motion will create a current I according to equation 2.30. The two proof masses are electrically connected, as shown in figure 2-10, so the current flowing into the sense preamp is the sum of the currents from each mass. During normal gyro operation, the sense plates are biased opposite each other, one at $V_{sensebiasleft} = +5\ V$, and the other at $V_{sensebiasright} = -5\ V$. The result of this biasing scheme is rejection of common mode motion in the sense direction. (i.e. if both masses are identical, and both move in the same direction by the same amount, the currents created will exactly cancel each other, and no output will be seen at the sense preamp output terminal). However, during testing I sometimes biased only one of the sense plates, to allow measurement of the motion of a single mass.

From equation 2.31, we only need to know $\frac{\partial C}{\partial y}$ to determine the relationship between V_{out} and sense motion. For one side, from equation 2.29,

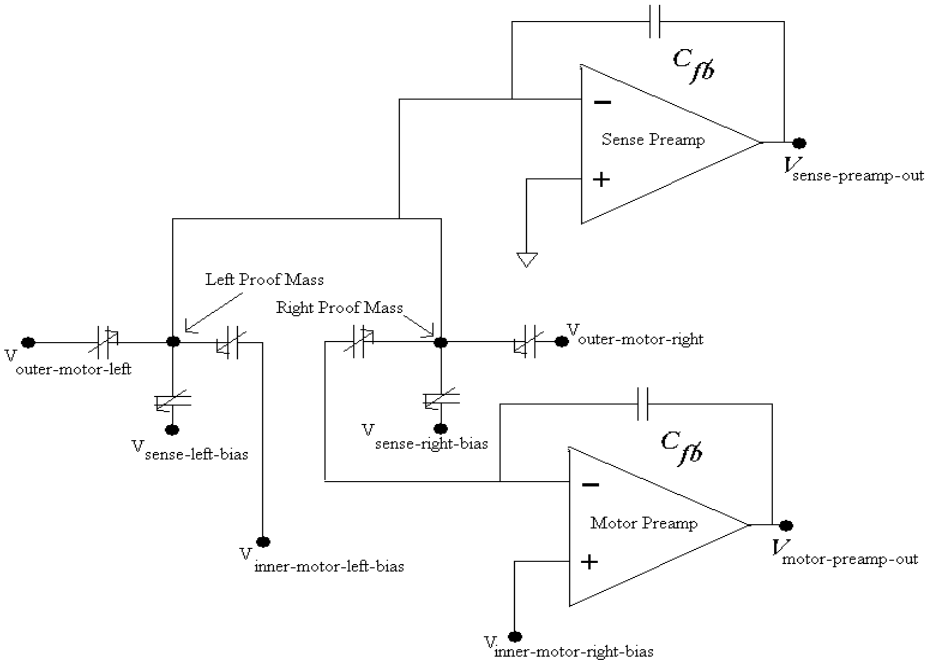

Figure 2-10: Capacitor Gyro Model with Sense and Drive Preamps

$$C = \frac{\epsilon_0 A}{g_1} = \frac{\epsilon_0 A}{y_0 + y} \tag{2.32}$$

So, taking the partial derivative of equation 2.32,

$$\frac{\partial C}{\partial y} = \frac{-\epsilon_0 A}{(y_0 + y)^2} \tag{2.33}$$

Now, we will assume that the motion of the mass, y, is much less than the total gap, y_0, so this reduces to,

$$\frac{\partial C}{\partial y} = \frac{-\epsilon_0 A}{y_0^2} \tag{2.34}$$

Plugging this back into equation 2.31,

$$\begin{aligned} V_{senseout} &= \frac{V_{bias}}{C_{fb}} \int \frac{\partial C}{\partial y}\, dy \\ &= \frac{V_{bias}}{C_{fb}} \int \frac{-\epsilon_0 A}{y_0^2}\, dy \\ &= \frac{V_{bias}}{C_{fb}} \int \frac{-\epsilon_0 A}{y_0^2}\, dy \\ &= \frac{V_{lb}}{C_{fb}} \cdot \frac{-\epsilon_0 A}{y_0^2} y_1 + \frac{V_{rb}}{C_{fb}} \cdot \frac{-\epsilon_0 A}{y_0^2} y_2 \end{aligned} \tag{2.35}$$

Where

V_{rb} = DC bias on the right sense plate

V_{lb} = DC bias on the left sense plate

C_{fb} = sense preamp feedback capacitor

ϵ_0 = permittivity of freespace

A = area of a sense plate

y_0 = nominal sense gap

y_1 = displacement of the left proof mass out of the plane with respect to the substrate

y_2 = displacement of the right proof mass out of the plane with respect to the substrate

From 2.35, we see that if $V_{lb} = -V_{rb}$, then $V_{out} = 0$ for $y_1 = y_2$, rejecting common mode motion. It is important to keep this result in mind when looking at the output from sense-out, as any common mode motion of the proof masses out of the plane will be greatly attenuated. Equation 2.35 also gives us the sense *scalefactor*, $\frac{-V_{bias}\epsilon_0 A}{C_{fb}y_0^2}$ which is the voltage produced at the preamp output for a given *differential* motion of the proof masses out of the plane.

Another important effect that occurs on the sense capacitive readout is *charge injection*. Figure 2-10 shows that the sense preamp is connected to both proof masses, each of which connects to two sets of combs. Thus, any motion of the proof masses *in the plane* will produce a current into the *sense* preamp due to the changing capacitance of the motor combs. This current will depend on the motion of the mass in the plane, and also on the voltage across the motor combs. So, in addition to the integration of the charge injected by motion out of the plane, the sense preamps will also integrate charge injected by motion in the plane. During normal gyro operation, the two masses move in the plane 180 degrees out of phase with each other. Thus, the charges injected due to their motion will exactly cancel. However, any time the proof masses do not move exactly opposite one another in the plane, charge injection into the sense preamp will occur, producing a signal at $V_{senseout}$. One particularly important case where this occurs is during hula motion. If any hula motion is excited, the charge injected from the two inner motor combs will not cancel, but sum. Thus, hula motion produces a large signal at the sense preamp output.

Capacitive sensing of motion in the plane of the device occurs at the left inner motor comb, as shown in figure 2-10. An identical derivation to that shown above, plugging the inner motor capacitance from equation 2.28 into equation 2.31, produces

$$V_{motorout} = 2N\frac{V_{lmb}}{C_{fb}}\frac{\epsilon_0 h}{g}x_1 \tag{2.36}$$

Where

N = number of tines extending from one side of the proof mass

V_{lmb} = DC bias on the left inner motor comb

C_{fb} = motor preamp feedback capacitor

ϵ_0 = permittivity of freespace

h = height of the motor tines

g = gap between the tines

x_1 = motion of the left proof mass in the plane

With the motor sensing system, it is important to note that only the motion of the left proof mass is measured. In addition, there are no charge injection effects in the motor readout.

2.3.3 Capacitive Drive

In addition to their application for sensing motion, the micromachined capacitors in the gyro are used for creating electrostatic forces on the masses. For a capacitor, the electrostatic force attracting the two sides of the cap together is

$$F = \frac{1}{2}V^2\frac{\partial C}{\partial x} = K_t V^2 \tag{2.37}$$

Where:

V = voltage across the capacitor

$\frac{\partial C}{\partial x}$ = partial derivative of the capacitance with respect to motion of the proof mass in the direction of the force

$K_t = \frac{1}{2}\frac{\partial C}{\partial x}$ = *Torquer Constant*, the force produced per volt squared

For the comb drive,

$$\frac{\partial C}{\partial x} = \frac{\epsilon_0 h}{g} \tag{2.38}$$

One very significant result of 2.37 is that force depends on the voltage squared. Thus, to produce a sinusoidal force at some frequency, the applied voltage across the capacitor must be a sinusoidal term plus a DC bias,

$$V = V_{DC} + V_{AC}\sin(\omega t) \tag{2.39}$$

Which will produce a force,

$$\begin{aligned} F &= K_t(V_{DC}^2 + 2V_{DC}V_{AC}\sin(\omega t) + V_{AC}^2\sin^2(\omega t)) \\ &= K_t(V_{DC}^2 + 2V_{DC}V_{AC}\sin(\omega t) + \frac{1}{2}V_{AC}^2 - \frac{1}{2}V_{AC}\cos(2\omega t)) \end{aligned} \tag{2.40}$$

Note that this method produces a force with power not only at the fundamental frequency of the input voltage, but also at the first harmonic.

By choosing the correct frequency ω and amplitudes V_{AC} and V_{DC}, we can drive a particular mode at a defined amplitude. In normal operation, the tuning fork mode is excited, in order to produce the desired Coriolis acceleration as described in section 2.2.3. During testing, modes other than the tuning fork mode were excited by driving a sinusoid at a different modal frequency as an excitation signal to one of the capacitors.

An identical electrostatic forcing effect is seen on the sense parallel plate capacitors, which also must obey equation 2.37. However, the capacitor relationship is different here (see 2.29), producing a different $\frac{\partial C}{\partial y}$. Therefore, for the sense caps, the electrostatic force is

$$F = \frac{1}{2}V^2 \cdot \frac{-\epsilon_0 A}{(y_0 + y)^2} \tag{2.41}$$

Where:

V = voltage across the capacitor

ϵ_0 = permittivity of free space

y_0 = nominal sense gap

y = motion of the proof mass out of the plane

Again, as in the comb drive, the force goes as the voltage squared. However, here the force changes with the gap, $g = y_0 + y$. As this gap goes to zero (i.e. the proof mass moves down towards the sense plate), the force goes to infinity. The result of this is an effect known as *snapdown*. If the proof mass moves too close to the sense plate, the electrostatic force will be greater than the spring restoring force, and the proof mass will be pulled down into contact with the sense plate, where it will stick due to the electrostatics. This could, potentially, destroy the gyroscope. One of the important results addressed in later sections is the maximum vibration allowable before snapdown occurs.

During normal gyro operation, the sense plates have a DC bias on them, which produces a small constant force. Dynamically, this force is not very important unless large enough motions are observed out of the plane to bring the nonlinear effects of 2.41 into play. Thus, for the most part, we will neglect this force. However, sometimes during testing I drive a DC bias plus a sinusoid onto the sense plates to excite motion out of the plane. Although this will not occur during normal gyro operation, it is useful for testing purposes.

2.3.4 Control Loops

There are two separate control chains used during closed loop gyro operation: the motor loop and the sense chain. The sense chain conditions the output from the sense preamp, and generates a rate-out signal, which estimates the rotational rate that the gyro is experiencing. The motor loop deals with signal conditioning of the motor preamp out signal, and creates the drive signal on the outer motor combs.

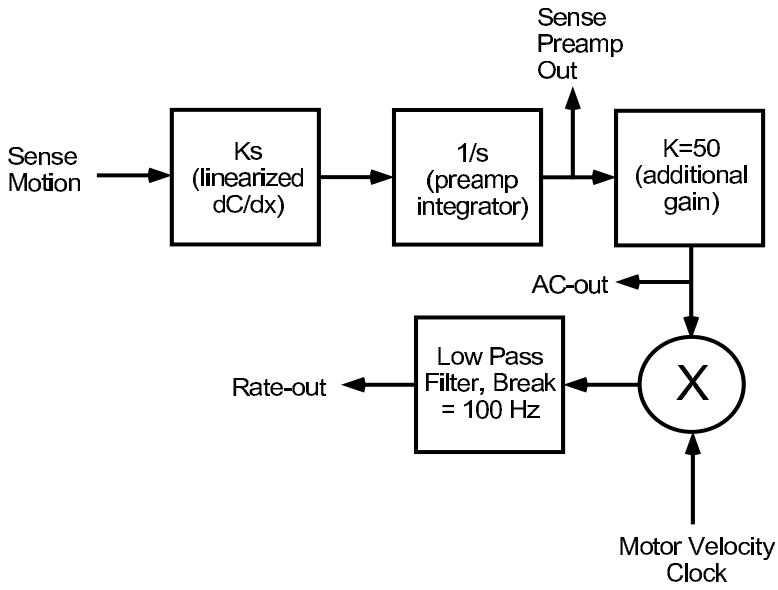

Figure 2-11: Block Diagram of Sense Chain Conditioning Electronics

Figure 2-11 is a block diagram of the sense chain. The differential motion of the proof masses is the input to the first block. The first block represents the sense capacitors. The caps produce a current, which is integrated by the preamp and gained up by a factor K. The signal at this point is the raw signal coming from the sense preamp, called *AC-out*. This signal is used extensively in testing.

AC-out is multiplied by the motor velocity clock, which is a square wave at the frequency of the motor motion, and in phase with motor velocity. The product is low pass filtered. (i.e. AC-out is demodulated by the motor velocity clock). The acceleration of the sense axis due to the Coriolis term, as described in section 2.2.3, is

$$\vec{A}_{Coriolis} = 2\vec{\Omega} \times \vec{v} \tag{2.42}$$

Thus, since the acceleration of the sense axis is in phase with this Coriolis acceleration, the sense acceleration is in phase with the motor velocity, v, for a DC rate, Ω. Acceleration is integrated twice to produce position, so sense position is also in phase with motor velocity. Since the sense preamp gives a voltage proportional to position,

the preamp output voltage will contain energy at the motor frequency (that is, the tuning fork frequency; we always drive the gyro in the tuning fork mode). Thus, demodulating by the motor velocity clock will produce a DC voltage proportional to the sense motion of the proof masses near the tuning fork frequency. It is assumed that any energy at this frequency is due to Coriolis accelerations, and thus the output of the demodulator should be proportional to the input rate, Ω. This is the output of the gyro, *rate-out*. Equation 2.2 in section 2.2.1 gives the full linear dynamic model of the sense axis.

For the current gyro design, the break frequency of the low pass filter is 100 Hz, so the gyro can sense rate inputs at frequencies lower than 100 Hz. Since the major gyro modal frequencies are in the 10-20 kHz range, the 100 Hz bandwidth avoids many errors that might come from other modal responses.

The motor loop produces the velocity clock used to demodulate AC-out, and the drive signal used to keep the motor axis oscillating at the tuning fork frequency. Figure 2-12 is a block diagram of the motor loop. ω refers to the tuning fork frequency, which is the frequency we are trying to drive the gyro at.

There are two fundamental in-plane modes for the gyro, as discussed in section 2.2.2. The hula mode is parallel motion of the masses in the plane, while the tuning fork mode is antiparallel. In order to produce the correct Coriolis accelerations, we drive the gyro in the tuning fork mode. This is accomplished by closing the loop around the motor axis: reading a position signal off of the left inner motor combs, and then driving the outer motor combs with the appropriate motor excitation signal, $V = A\ sq(\omega t) + B$. (A square wave is used rather than a sine wave as it is easier to produce in the electronics.) This signal produces an electrostatic force as described in section 2.3.3. Since the forces generated by the outer combs are attractive, we always drive the tuning fork mode rather than the hula mode, since we pull both masses toward the outside at the same time. (i.e. we drive the outer motor voltages in phase with each other)

Since the device has such a high Q, random noise in the system will excite the modes to some degree. This small motion will be picked up by the inner motor combs,

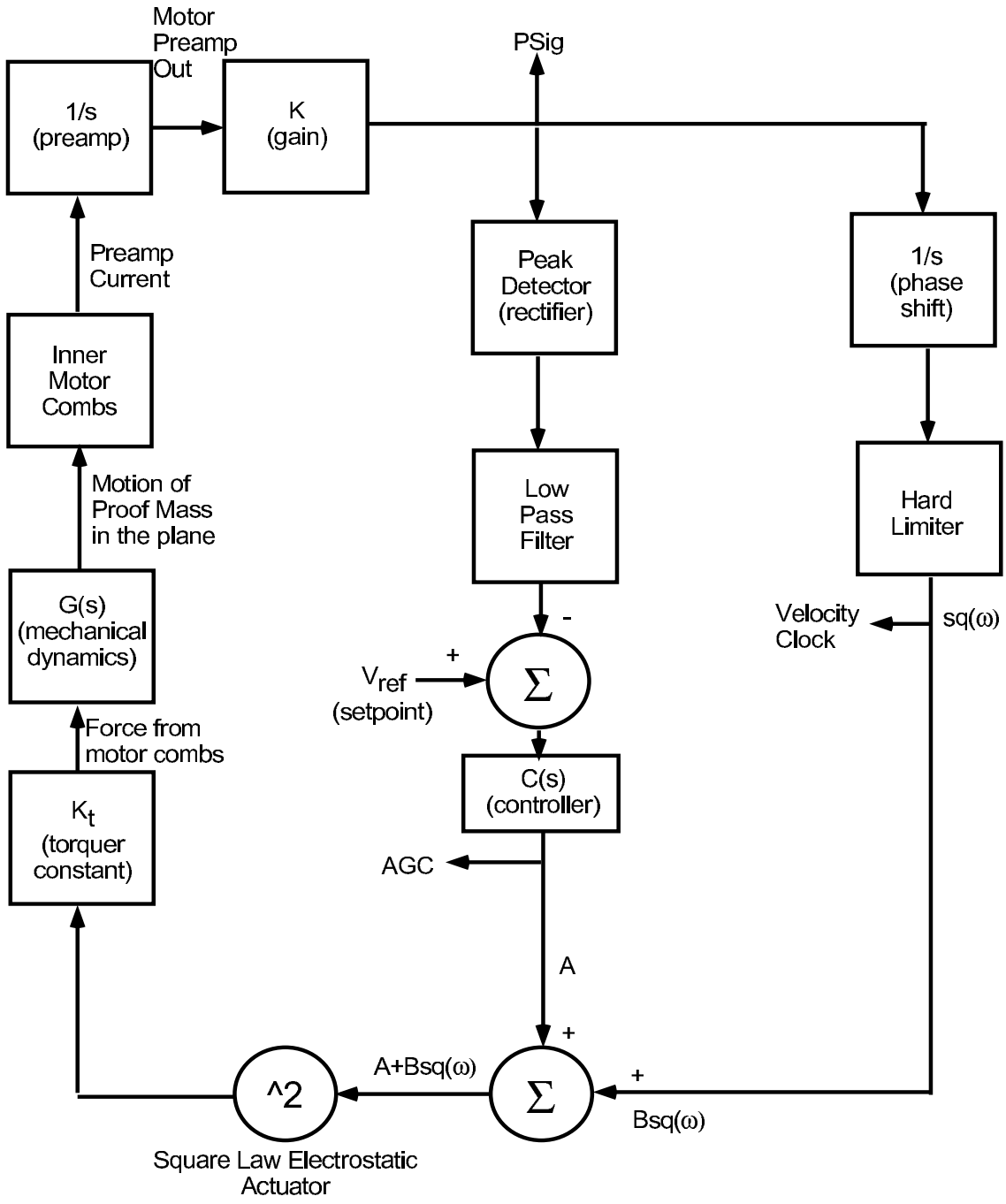

Figure 2-12: Block Diagram of Motor Loop Electronics

and amplified by the motor loop, allowing the gyro to start with no external reference.

Figure 2-12 shows how the position signal (labeled PSig) is hard limited to produce the $sq(\omega t)$ term used in the motor excitation signal, and also shows the controller C(s) which compares actual motion with the setpoint, V_{ref}, to drive the gyro at a defined amplitude. V_{ref} is chosen to reflect the desired drive amplitude.

Other signals of interest are labeled in figure 2-12: AGC, automatic gain control, gives a measure of how much force is being used to keep the motion at the setpoint. PSig is the raw inner motor preamp voltage, multiplied by a constant. This signal indicates the motion of the left proof mass in the plane. The velocity clock is used to demodulate AC-out, as described above in the discussion of the sense chain.

2.4 Maximum Allowable Response

Throughout the remaining chapters, the response of the gyro to various vibrations and impacts will be considered. In order to determine the maximum allowable excitations, we must determine the highest level of gyro response that can be safely sustained. There are three main dangers during gyro operation.

2.4.1 Clipping of AC-out

The first danger to the gyro is clipping of AC-out. If signal levels get too high, the electronics will saturate at the level of the positive or negative supply voltage, generating unpredicted results at gyro outputs. (This effect is referred to as *clipping* of the signal.) The supply voltage has a level of 15 V, so AC-out must not exceed 15 V. There is a gain of 50 between the preamp output and AC-out, so sense preamp output must not exceed 300 mV_{pk}. Equation 2.35 in section 2.3.2 showed that the sense preamp output was related to sense motion by

$$V_{out} = \frac{V_{lb}}{C_{fb}} \cdot \frac{-C_{sl}}{y_0} y_1 + \frac{V_{rb}}{C_{fb}} \cdot \frac{-C_{sr}}{y_0} y_2$$

Where

V_{rb} = DC bias on the right sense plate = +5 V

V_{lb} = DC bias on the left sense plate = -5 V

C_{fb} = sense preamp feedback capacitor = 2.2 pF

C_{sl} = zero displacement left sense capacitance = 3.8 pF

C_{sr} = zero displacement right sense capacitance = 3.8 pF

y_0 = nominal sense gap =2.8 μm

y_1 = displacement of the left proof mass out of the plane with respect to the substrate

y_2 = displacement of the right proof mass out of the plane with respect to the substrate

Where values are given for a standard TFG14, LCCC575. From the equation, then, to produce $V_{out} = 300mV$, requires differential sense motion $y_1 - y_2$ of approximately 0.1 μm. Thus, differential sense motion of 0.1 μm will begin to clip AC-out.

Another common cause of AC-out clipping is large motions of the hula mode. Hula motion causes charge injection into the sense preamp as described in section 2.3.2. The charge injection into the proof mass is caused by changes in the inner motor capacitance (see equations 2.30 and 2.28)

$$I = \frac{V_{lbias} C_{iml}}{x_0} \frac{dx_1}{dt} + \frac{V_{rbias} C_{imr}}{x_0} \frac{dx_2}{dt} \tag{2.43}$$

This current is integrated by the sense preamp to produce

$$V_{out} = \frac{1}{C_{fb}} \left(\frac{V_{lbias} C_{iml}}{x_0} x_1 + \frac{V_{rbias} C_{imr}}{x_0} x_2 \right) \tag{2.44}$$

Where

V_{rbias} = DC bias on the right inner motor = +5 V

V_{lbias} = DC bias on the left inner motor = -5 V

C_{fb} = sense preamp feedback capacitor = 2.2 pF

C_{iml} = zero displacement left inner motor capacitance = 0.45 pF

C_{imr} = zero displacement right inner motor capacitance = 0.45 pF

x_0 = nominal motor comb overlap = 25 μm

x_1 = displacement of the left proof mass in the plane with respect to the substrate

x_2 = displacement of the right proof mass in the plane with respect to the substrate

During hula motion, x_1 and x_2 are opposite one another in phase, so their effects sum. Thus, a hula amplitude (amplitude of one mass, both assumed to have approximately the same amplitude) of 3.75 μm will begin to clip AC-out.

So, to avoid clipping AC-out, we must avoid

- Hula mode motion in excess of 3.75 μm.
- Sense mode motion in excess of 0.1 μm of differential motion.

2.4.2 Physical Contact and Snapdown

Physical contact in the combs can damage the gyro. The maximum allowable displacement of the motor before contact occurs is 25 μm. In the sense direction, the gap is 2.8 μm.

However, prior to contact between the proof mass and the sense plate, snapdown will occur. This occurs when the electrostatic attraction between the sense plate and the proof mass overcomes the restoring force of the mechanical sense flexure. Equation 2.41 gave the force generated by the electrostatics in a parallel plate capacitor as

$$F = \frac{1}{2}V^2 \cdot \frac{-C_{sl}y_0}{(y_0 + y)^2}$$

Where:

V = voltage across the capacitor = 5 V

C_{sl} = zero displacement sense capacitance = 3.8 pF

y_0 = nominal sense gap = 2.8 μm

y = motion of the proof mass out of the plane

Equating this with the spring force to determine the point at which snapdown occurs produces

$$\frac{1}{2}V^2 \cdot \frac{-C_{sl}y_0}{(y_0+y)^2} = -k_y y \tag{2.45}$$

Where k_y is the sense flexure stiffness, which is typically (data taken for LCCC574) approximately 350 N/m. Solving equation 2.45 gives two solutions, one is stable and one unstable. The unstable solution corresponds to snapdown, and lies at $y = 2.5$ μm. So, displacements of this size will cause snapdown. I will consider displacements of more than $2\mu m$ as unacceptable.

One final danger is that the motor loop will lose lock on the tuning fork mode. The design of the motor loop assumes that the majority of the position signal is coming from the tuning fork mode, and feeds back on this signal to drive the tuning fork mode at the desired amplitude of 10 μm. If the hula amplitude is on the same order as the tuning fork amplitude, 10 μm, then the motor loop will begin driving hula mode, or possibly lock up completely. . Section 7.3.4 presents experimental data showing that 10 μm of hula motion causes gyro operation to shut down due to a complete loss of tuning fork motion. This process is reversible, but the gyro power may need to be removed and all mechanical motion given time to damp out before operation is resumed.

Thus, to ensure safe gyro operation, we require that

- Tuning fork motion is less than 25 μm in amplitude.
- Hula motion is less than 10 μm in amplitude.
- Any sense direction motion (sense mode *or* out-of-plane mode) is less than 2 μm in amplitude.

Chapter 3

Experimental Setup

Vibration and impact testing of the gyro required design and acquisition of a number of experimental systems. This chapter describes the various parts of the test setup, and explains how they were used during my experiments. The chapter is organized into sections describing the test electronics, the two shaker systems, fixturing, and measurement equipment (including reference accelerometers).

3.1 Electronics

Figure 3-1 is a photograph of the EDM3 test electronics, on the right, with the breakout box (center) and Labworks shaker (left). The Wilcoxon power amp is in the background, and the kyocera socket with guillotine connectors is shown on the bottom right.

In addition to the EDM3 electronics described in section 2.3.4, much testing was conducted open loop using the *belljar electronics*. The belljar electronics do very little as far as signal conditioning; they simply give access to various gyro signals. Both the sense-preamp-out and motor-preamp-out signals, are available. In addition, the belljar electronics allow an arbitrary voltage to be driven onto the outer motor combs or the sense plates. All testing done using the belljar electronics is *open loop*; the gyro is excited in some way, and the various outputs are measured. No feedback occurs. This is most useful for examining the mechanical response of the gyro without the

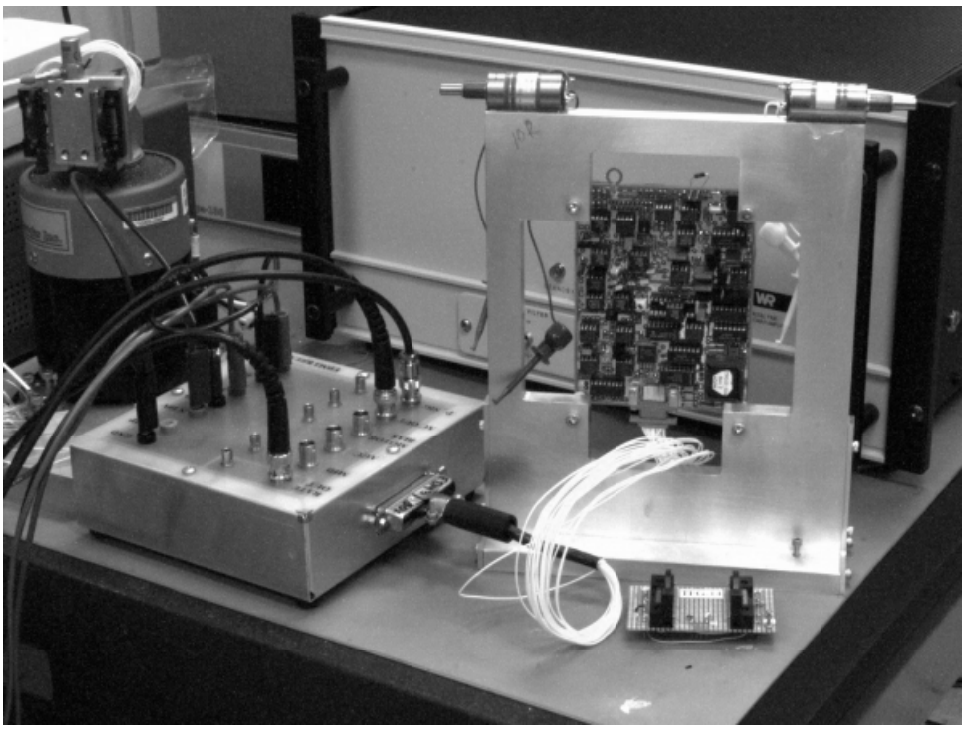

Figure 3-1: Photograph of EDM3 Board with Breakout Box and Cabling

additional complexities created by the closed loop controllers.

Closed loop testing made use of the control loops described in section 2.3.4, with all of the accompanying complexity in signal conditioning and feedback control. Closed loop operation using the test electronics more closely approximates the operation of the gyro in the field.

For all vibration and impact testing, the gyro itself is isolated from the electronics. This reduces the number of variables involved, so that we can be sure that the observed effects are an artifact of gyro response, and not the electronics responding to vibration. To accomplish isolation, a cable was created which plugs into the test structure where the gyro is mounted and carries each gyro signal out to a dummy kyocera package. This dummy package is identical to the gyro package, and so easily mates with any system that the gyro would normally plug into. Using this method, the gyro can be held in the test structure and undergo vibration or impact while the electronics are off to the side.

3.2 Shakers

Two shaker systems have been purchased and utilized in this project. The two shakers differ most dramatically in their operational frequency range. The Labworks ET-126 is an electromagnetic shaker, and operates best in the low frequency range. The Wilcoxon D60H is a piezoelectric shaker, and thus operates best at high frequencies. Summarizing their capabilities:

Electromagnetic Shaker:

nominal operating range = DC-10 kHz

best operating range =1 kHz -5 kHz

maximum acceleration =20 $g_{peak-to-peak}$ above 20 Hz

Piezoelectric Shaker:

nominal operating range = 3-50 kHz

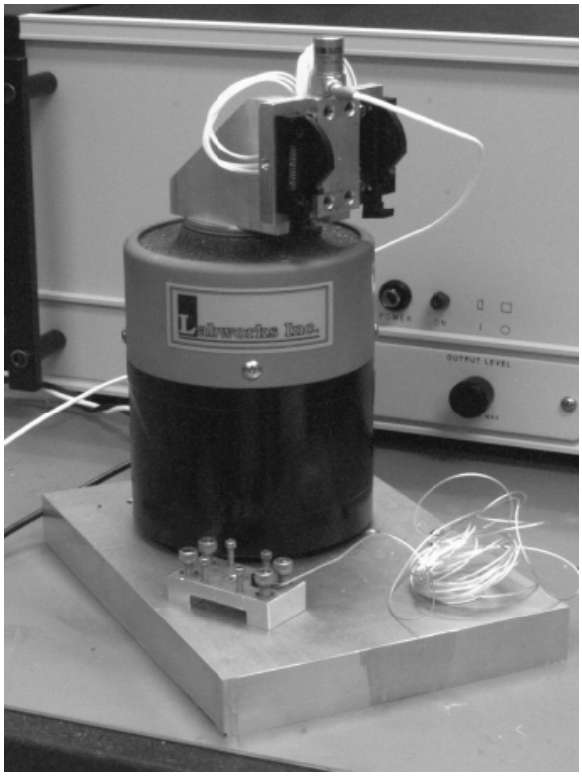

Figure 3-2: Photograph of Labworks Shaker with Fixturing

best operating range	= 3-35 kHz
maximum acceleration	= 1300 $g_{peak-to-peak}$ at resonance,
	about 60-100 $g_{peak-to-peak}$ elsewhere

3.2.1 Labworks ET-126 Electromagnetic Shaker

The Labworks ET-126, pictured in figure 3-2 with test fixturing mounted, consists of a table (to which the test specimen is bolted) attached to a coil. This coil is mounted on a flexible structure, which allows the table and coil to translate. Inside the coil is a ferromagnetic core, which attaches to the base of the shaker. By driving a current through the coil at a particular frequency, a magnetic force is generated between the coil and the core, moving the table back and forth on the flexures. We can model the mechanical structure as a mass-spring-damper system, coupled to an electrical system

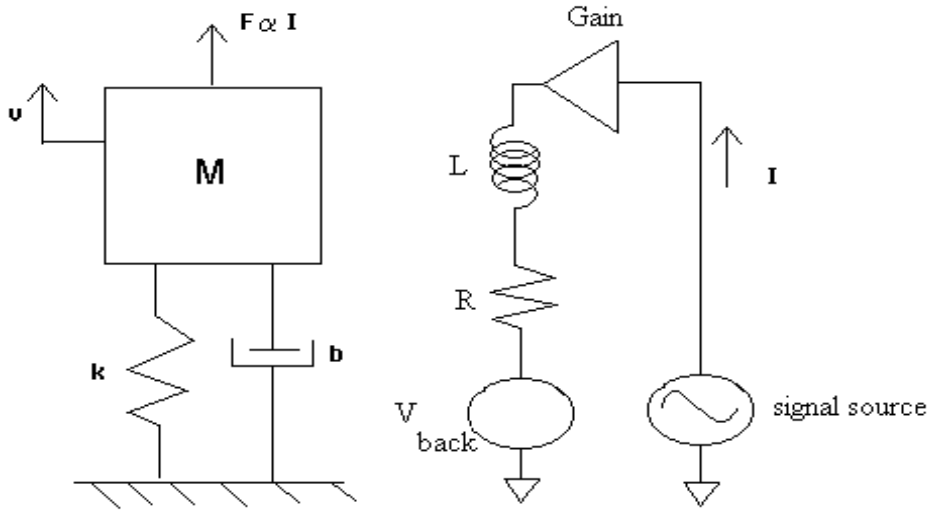

Figure 3-3: Lumped Element Model of the Labworks Electromagnetic Shaker

via a transformer. The result of this model is a second order system, diagrammed in figure 3-3.

Below the shaker resonant frequency of 20.6 Hz, a large displacement is needed for a given acceleration. Thus, below resonance, the shaker is limited by the maximum displacement it can undergo. Below resonance the maximum deliverable acceleration is:

$$a_{max} = X_{max} \cdot \omega^2 = (0.019 m_{pk-pk}) \cdot \omega^2 \tag{3.1}$$

Where the maximum allowable shaker displacement, taken from the manufacturers specifications, is 0.019 m.

At and above resonance, the maximum achievable acceleration is limited by the shaker's maximum output force, and so will depend on the mass loaded on the table. The intrinsic mass of the shaker table is 90 g, and it's maximum output force is 111 N_{pk-pk}. In my case, I have an additional mass of approximately 400 g loaded onto the table. With these limitations, the maximum allowable acceleration is 22.7 g_{pk-pk}. Taking both maximum displacement and maximum force into account, we

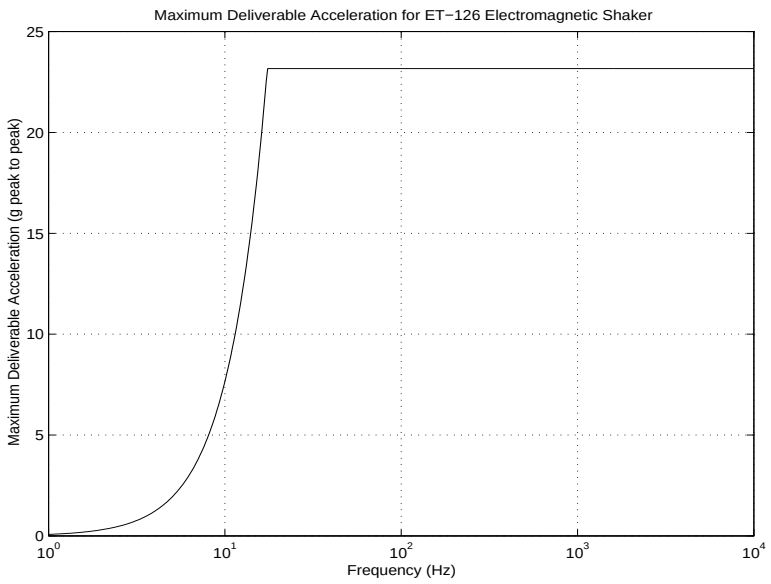

Figure 3-4: Maximum Acceleration Deliverable by ET-126

can summarize the maximum deliverable acceleration as a function of frequency, as is done in figure 3-4.

3.2.2 Wilcoxon D60H Piezoelectric Shaker

The Wilcoxon piezoelectric shaker, pictured in figure 3-5 with fixturing mounted, was used for all high frequency testing during my project. With its large bandwidth, high peak force output, and good frequency response, the D60H is ideal for vibration testing of small structures. Here, again, the same issues are encountered in determining maximum deliverable acceleration. Below resonance, the shaker is displacement limited. Above resonance the shaker is limited by maximum allowable force.

However, the maximum force obtainable from piezoelectric materials is very high (for this stack, 4000 N_{peak}). Thus, within the operating range described, it is unlikely that this limit will be reached before the power amp gives up. Indeed, that is what happens for much of the operating range.

The D60H can be modeled using lumped parameters. Mechanically, there is a mass-spring-damper system corresponding to the intrinsic mass, damping, and com-

Figure 3-5: Photograph of Wilcoxon Shaker with Fixturing

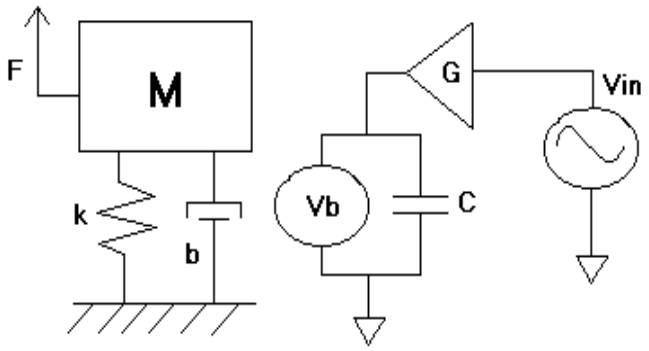

Figure 3-6: Lumped Element Model of the Wilcoxon Piezoelectric Shaker

pliance of the piezoelectric stack and accompanying mounting table. Electrically, the piezoelectric material acts like a capacitor in parallel with a transformer which transforms voltage across the capacitor into force on the table mass. This is diagrammed in figure 3-6. Note that since the power amplifier is modeled as an ideal voltage source, the degree of freedom contributed by the capacitor is removed. As long as we do not tax the power amplifier too heavily, we can make the assumption that it does act as a voltage source, which reduces the complexity of the shaker model. Since this model is to be used only for determining appropriate operating ranges, it is not terribly critical and so the assumption will be made.

Using this model, and the parameters determined from testing, it is possible to produce a transfer function relating acceleration of the table to the input voltage.

Using these parameter values:

m=0.090+0.400	Mass of the table and a 400 g load. $[kg]$
k=$2.28 \cdot 10^9$	Deduced from fundamental resonance. $[N/m]$
b=500	Computed damping ratio by measuring width of resonance. $[N/(m/s)]$
G=20.4	Measured. Gain of the power amp.
C=0.011	Given in specs $[\mu F]$
k2=1.1	Given in specs. Force per volt in transducer. $[N/V]$

A theoretical prediction of the frequency response can be generated, as shown in

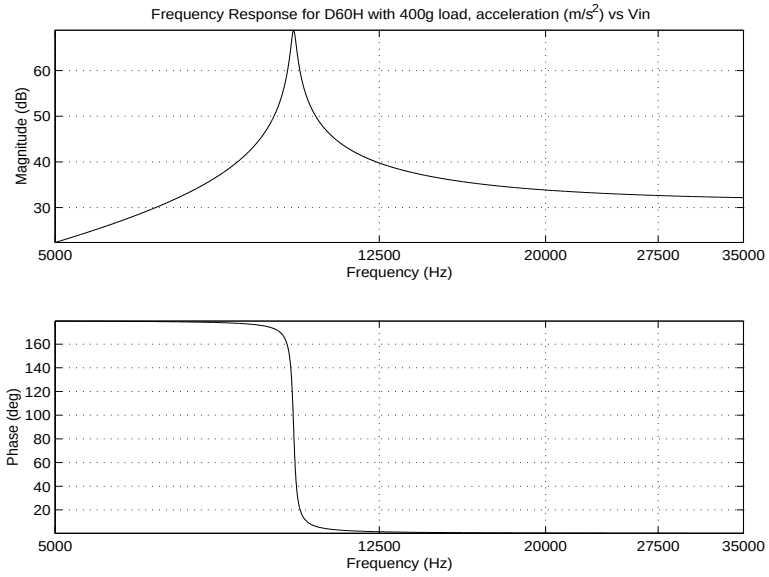

Figure 3-7: Theoretical Frequency Response of D60H, 400 g load on table

figure 3-7.

The maximum deliverable acceleration is limited by two parameters. The power amp must not be overtaxed, and the maximum force in the spring (i.e. the piezo stack) must not exceed 4000 N_{peak} (according to shaker specs). Unfortunately, Wilcoxon has not been able to supply good information about the PA8C power amplifier; they have not tested the maximum output power, current, and voltage measurements when driving a capacitive load such as the piezo shaker. However, my testing indicates that the PA8C can be safely run to $130V_{peak}$ over the 10-22 kHz range. Assuming that this voltage will be available throughout the frequency range, and making sure that we avoid overforcing the shaker (again, we must not exceed 4000 N), then the maximum output acceleration curve can be generated. This curve is presented in figure 3-8.

The curve in figure 3-8 assumes a 400 g mass attached to the table (this is the mass of my test fixturing). A maximum acceleration of 2340 $g_{peak-peak}$ is achievable at resonance.

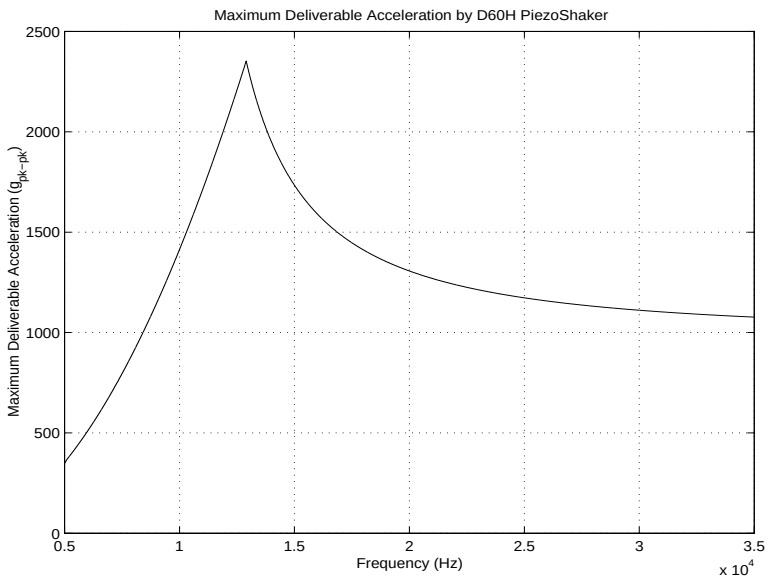

Figure 3-8: Theoretical Maximum Deliverable Acceleration, D60h with 400 g load

3.3 Fixturing Issues and Designs

The tuning fork gyro, as discussed in section 2.1.2, is mounted in a kyocera package, along with the preamps. For vibration testing, only hardmounted gyros are used. These gyros are hardmounted into a flatpack. However, the flatpack has no means of mechanical connection to a shaker; it simple has the pins for the electrical connection. Thus, is was necessary to build test fixtures to clamp the flatpack down to the shaker table, with electrical connectors to bring out all of the signals to the test electronics.

Much effort has gone into designing and testing the fixturing. It is crucial that the gyro flatpack mount stiffly to the shaker table, providing a clean acceleration signal to the gyro. There are a number of issues associated with this:

1. There must be no major fixture modes in the frequency bands of interest.

2. The fixture must minimize any transverse motion of the gyro.

3. The fixture must allow high acceleration of the table.

4. The fixture should allow the gyro to be mounted in at least two (sense and

drive) axes.

5. The fixture must allow easy electrical connection to the gyro electronics.

To accomplish these goals, a number of design criteria must be met:

1. High stiffness of structure. (Most importantly, we need to avoid bending modes)
2. Solid mount to the gyro flatpack.
3. Highly symmetrical structure minimizes transverse motion.
4. Low moment of inertia reduces transverse motion and fixture modes.
5. Low mass allows high acceleration.
6. Either separate fixtures or a reconfigurable fixture must be used to allow 2 axis mounting.
7. Cabling should allow mating with all existing gyro electronics.

Three iterations of fixturing moved from simple, bolted together fixtures to solid aluminum fixturing. The final two fixtures bolt onto the shaker tables using the shaker bolt pattern. These two fixtures will be referred to as the *overhung fixture* and the *sense axis fixture*. Figure 3-5 is a photograph of the Wilcoxon piezoshaker with the overhung fixture mounted. Figure 3-2 shows the Labworks shaker with the sense axis fixture mounted on brackets. The overhung fixture orients the gyro such that the motor axis experiences the primary shaker vibration; it is only used on the Wilcoxon piezoshaker. The sense axis fixture orients the gyro so that the sense axis experiences the primary vibration, and can also be used on the Labworks shaker with mounting brackets to deliver vibration in the motor direction.

Electrical connection is made to the gyro using the guillotine connectors, which lead to a 21pin miniature connector which the dummy cable plugs into (section 3.1), allowing mating with all existing gyro test electronics. Solid mechanical connection to the gyro is accomplished by screwing down from above the flatpack, pressing it

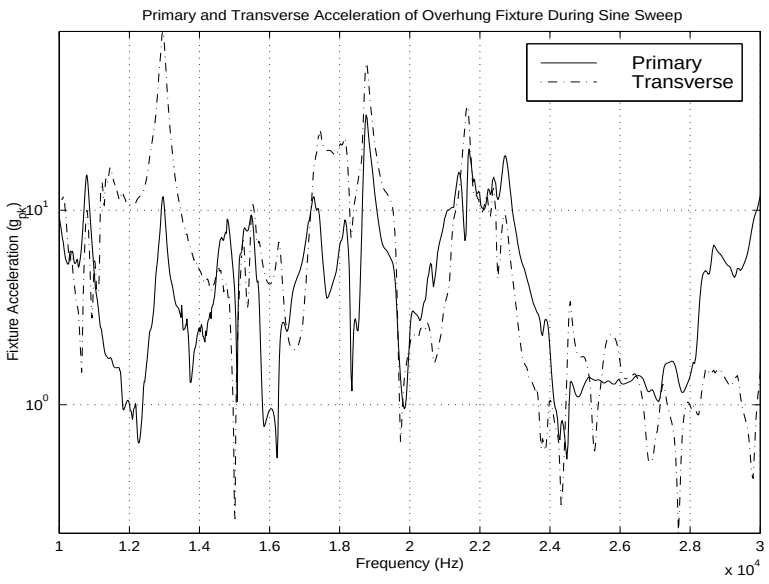

Figure 3-9: Measured Primary and Transverse Acceleration of the Overhung Fixture

tightly against the fixture base. Both fixtures are very symmetrical about the center of the shaker table, and both lie low, giving a low center of mass. With an adapter plate, the fixtures can be used on either shaker. Mechanical drawings of the fixtures appear in appendix B.

3.3.1 Transverse Acceleration

One of the initial aims of the fixturing was to reduce transverse acceleration. Ideally, we would want to shake the gyro in a single direction at a time in order to isolate particular effects. However, it became apparent throughout the fixturing design that this would not be possible. Thus, in any test there is always substantial transverse acceleration in addition to the primary vibration. Figure 3-9 shows the acceleration in the primary and transverse accelerations for the overhung fixture during a single constant voltage frequency sweep of the piezoshaker.

As can be seen in the figure, the transverse acceleration is the same order of magnitude as the primary acceleration. At times, it even exceeds the primary. Thus, we cannot generate vibration in a single direction at a time.

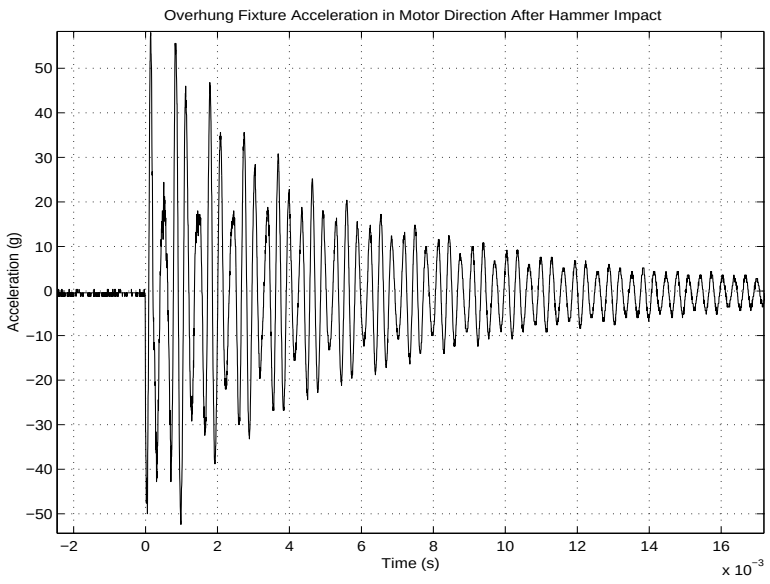

Figure 3-10: Time Data for Acceleration of Overhung Fixture after a Hammer Impact

3.3.2 Fixture Modes

A number of fixture modes have been observed, despite all attempts to limit low frequency modes in the fixture design. These are not necessarily problematic to testing, but it is important to know where they lie so that we can identify the source of these frequencies if they are seen in the gyro outputs. In order to avoid problems due to distortion in shaker vibration, modes were measured by recording fixture acceleration data with the reference accelerometer after the fixture modes were excited by a hammer impact (see section 3.5.3).

Figures 3-10 and 3-11 show typical time acceleration data and a PSD of that data for a hammer impact to the overhung fixture. The figure shows the fixture ringing down. For the PSD, only frequencies from DC to 12 kHz are shown, since no large spikes are seen above this frequency.

From similar data taken for both fixtures major fixture modes can be determined. Table 3.1 summarizes the fixture modes for the overhung fixture. Sense fixture modes are summarized in table 3.2. Each modal frequency is listed, along with a description of the type of impact needed to excite the mode, and the types of acceleration pro-

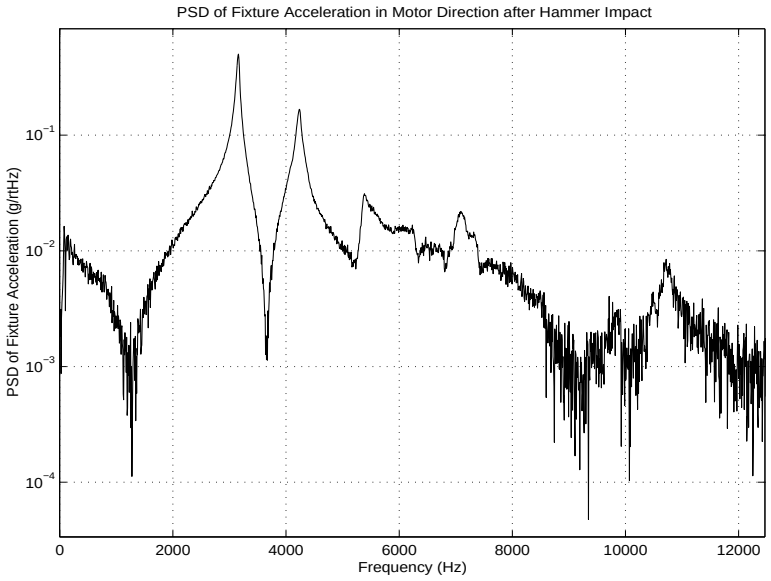

Figure 3-11: PSD of Overhung Fixture Impact Acceleration Data

duced. The nomenclature I have used refers to one fixture axis as sense and one as motor. These names are taken from the mounted gyro; the sense and motor directions are defined for the gyro, and so can be used to refer to fixture orientation in reference to the orientation of the mounted gyro package.

It will be important to refer to tables 3.1 and 3.2 later on when looking at gyro response. We will see some of the frequencies listed appearing in gyro output. An impact to the fixture will cause the fixture to ring at the above frequencies, and so the gyro will be excited by an acceleration signal containing most of its power at the fixture modal frequencies.

3.4 Signal Distortion

Another test issue to be considered is distortion in the acceleration signal. This seems to be inherent to the shaker, and there is really no way to reduce distortion. According to Wilcoxon, piezoelectric shakers can significantly distort input signals due to their nonlinear transfer functions, hysteresis, and sharp resonances. Indeed, major

3160 Hz	Fundamental mode, excited by impacts to either the sense or motor axis. Acceleration at this frequency is strong in the readings of both accelerometers.
4240 Hz	Another powerful mode excited by both types of impact and seen on both accelerometers.
5380 Hz	Acceleration of this mode is higher in the sense axis direction, but is more powerfully excited by an impact in the motor axis direction.
11.240 kHz± 100 Hz	Excited by sense impact; visible exclusively in the sense acceleration.
12.96 kHz	Excited by either motor or sense impacts, but acceleration seems to be entirely in the sense axis direction.
22.2 kHz ± 100 Hz	Small spike seen only in sense acceleration, but excited by both types of impact
26-28 kHz	"Messy" peak spread over these frequencies. Excited only by motor axis impact, but visible in both acceleration signals.

Table 3.1: Overhung Fixture Modes Determined from Impact Tests

9150 Hz ± 20 Hz	Second largest peak, fairly clean
10.7 kHz ± 50 Hz	Smaller peak, but still clearly a mode
13.8 kHz ± 50 Hz	Much smaller peak, but still visible
15.8 kHz ± 50 Hz	Much smaller peak, but still visible
20.17 kHz ± 10 Hz	Strongest mode, clean and narrow peak
26.4 kHz ± 50 Hz	Smaller peak, but still clearly a mode

Table 3.2: Sense Fixture Modes Determined from Impact Tests

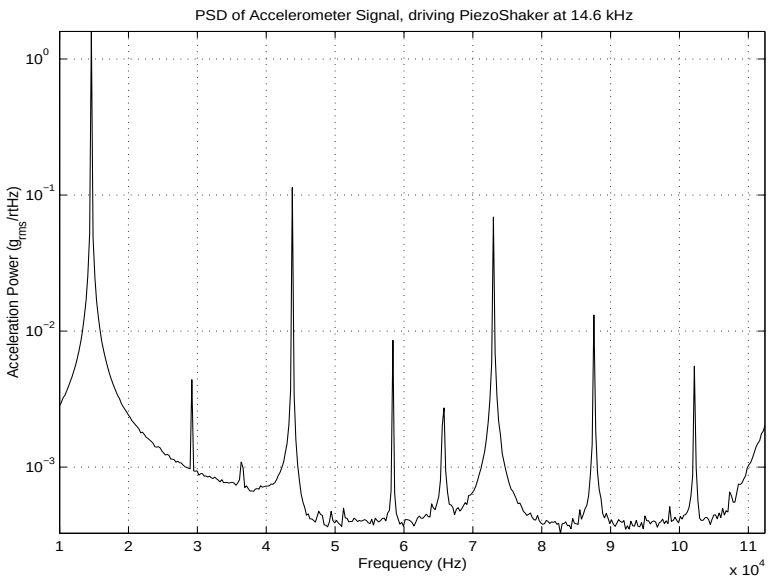

Figure 3-12: PSD of Shaker Acceleration while driving D60H with 14.596 kHz sinusoid

distortion of the signal generator signal is seen at some frequencies. This is unfortunate, since distortion adds energy to the acceleration signal at frequencies other than the one being driven. For this reason, it is important to use the accelerometer signal as a reference, rather than the shaker input. Figure 3-12 gives an example of the power spectrum of a distorted acceleration signal, as measured by the reference accelerometer. The driving signal into the power amp was a clean 14.6 kHz sine wave. Tests indicate that the power amp output is also clean, so distortion is being created either by the shaker or the accelerometer. Endevco is confident that their accelerometer would not produce this much distortion. Since piezoshakers are known to produce distortion, it seems reasonable to assume that the source of the problem is, indeed, the shaker. Distortion increases with higher peak acceleration, as one would expect.

While it is important to be aware that distortion of the acceleration signal is occurring, this is not fatal to testing. At many frequencies, distortion is not high, especially at low vibration amplitudes. Also, many gyro effects are limited to very narrow frequency bands, so distortion at higher harmonics of the fundamental vi-

bration will not interfere with testing. Still, it is important to recognize that some distortion is occurring, and to think about how this will affect tests on a case by case basis.

3.5 Measurement Equipment

A number of pieces of equipment were used for measuring gyro and fixture response during testing. This section describes the major pieces of test equipment.

3.5.1 Standard Test Equipment

Two pieces of standard test equipment were used for measuring and recording data. The Tektronix digitizing oscilloscope, TDS510A, was used for recording time domain data. It has a maximum sampling frequency of 500 MHz, well above the gyro frequencies. The scope has an internal floppy drive for recording the trace data, which can then be processes as needed. The major limitations of the scope are its resolution, which will sometimes cause recorded data to appear quantized, and the size of the memory, which limits the length of data that can be recorded.

In addition to the scope, the HP Dynamic Signal Analyzer, 35665A, was used for frequency domain data acquisition. The signal analyzer can be used as a function generator, and so can be used for swept sine frequency response measurements. It can also be used to take PSDs of an incoming signal. Again, the 35665A is equipped with an internal floppy drive, which was used for recording PSD and frequency response plots.

3.5.2 Endevco and Wilcoxon Accelerometers

Since there are many fixtures modes and some distortion in the acceleration signals, if is important to have a reference accelerometer mounted on the test structure. Two reference accelerometers have been used during testing: the Wilcoxon 736, and the Endevco 2250A-10.

	Wilcoxon 736	Endevco 2250A-10
Scale Factor (mV/g)	100	10
Sensor Bandwidth (kHz)	17	15
Mass (g)	21	0.4
Mounting Scheme	Screw Stud	Adhesive
Mounting Stiffness (N/m)	$3.5 \cdot 10^8$	High (cyanoacrylate)
Mounting Bandwidth (kHz)	20	> 200
Maximum Acceleration (g)	500	1000

Table 3.3: Comparison of Wilcoxon and Endevco reference accelerometers

Wilcoxon's accelerometer was packaged with the piezoshaker. It is a stud-mounted accelerometer, with a sensitivity of 100 mV/g, and a nominal 17 kHz bandwidth. The Endevco accelerometers are much smaller, adhesive mounted, and have a nominal 15 kHz bandwidth. Table 3.3 compares the two accelerometers.

The most significant difference between the accelerometers is their size and mounting scheme. Mounting the Wilcoxon accelerometer on a stud essentially creates a mass-spring system, which functions as a mechanical low pass filter. The high mass and relatively low stiffness of the mounting stud create a break frequency in the neighborhood of 20 kHz, for accelerometer motion parallel to the stud. Figure 3-13 illustrates the situation.

Perhaps even more significant than parallel motion is cantilever motion of the Wilcoxon accelerometer. If the accelerometer is mounted on a surface which moves perpendicular to the stud, the mounting stud acts as a cantilever beam, bending with a much lower stiffness than it did longitudinally. Bending adds a number of additional dynamics to the accelerometer motion, which will be coupled into the measured acceleration signal. Figure 3-14 shows how motion of the structure can induce a rocking motion of the accelerometer. The spring represents the flexible mounting stud, the mass represents the bulk of the accelerometer.

Most notably, bending of the mounting stud will cause the accelerometer not only to translate, but also to rotate. This rotation could cause the accelerometer to sense acceleration perpendicular to the actual direction of fixture motion.

For this reason, the Endevco accelerometers were preferable for use as reference

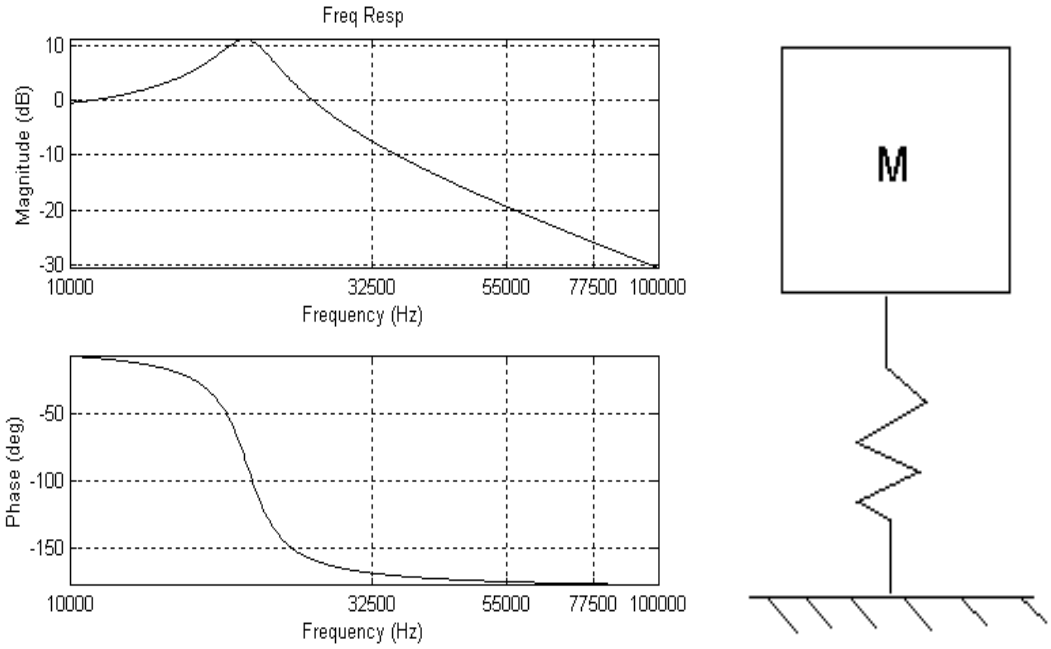

Figure 3-13: Stud-mounted Accelerometer acts as a Mechanical Lowpass

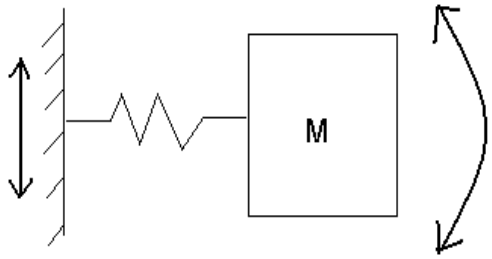

Figure 3-14: Cantilever Situation for Stud-mounted Accelerometer

accelerometers. Their small size and mounting scheme also allow them to be mounted very close to the gyro package. This should allow more accurate measurement of the excitation experience by the gyro itself.

3.5.3 Modally Tuned Impulse Hammer

PCB's GK291B is used for delivering a mechanical impulse to a structure. The hammer consists of 3 parts. Its body is similar to that of a small conventional hammer. Just before the "head" of the hammer, there is a force sensor which gives a voltage out proportional to the force experienced during impact (2.33 mV/N). Screwed into the sensor is the impact tip. A number of different tips are available. They range from a hard tip that is simply a disc of steel, to soft tips capped with a rubber dome. Different tips will give different types of impulse. A softer tip delivers a lower amplitude, longer duration impulse, which will have more low frequency content. Hard tips deliver a higher amplitude, shorter impulse with more power at high frequencies.

The force sensor in the hammer has a break frequency of 8 kHz. It cannot, therefore, be used to measure frequency content above this level. Since the main gyro modes lie in the 10-20 kHz band, the hammer sensor will not be used to measure the power delivered at these frequencies. Instead, measurements of the input will be taken from the Endevco reference accelerometers. The force sensor itself has been used only to estimate the overall power of a particular impact, and as a trigger for capturing time domain data on a digital scope. Figure 3-15 shows typical force sensor output for a single impact.

3.6 Complete Experimental System

For mechanical tests the shakers and the impact hammer are used to generate a mechanical excitation to the test fixture, which transmits it to the gyro. The shakers and the fixture have their own dynamics, which contribute to the final excitation seen by the gyro. Using the reference accelerometers, the mechanical excitation is measured as accurately as possible. Gyro response is observed during the test.

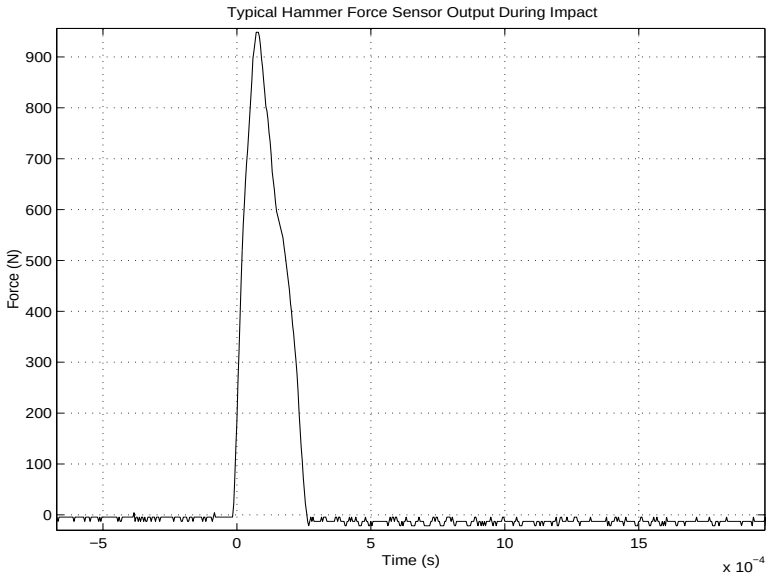

Figure 3-15: Typical Hammer Force Sensor Output

During electrical tests, electronics such as the belljar electronics are used to deliver an electrical excitation to the gyro. Again, gyro response is observed. Through these tests we can explore the dynamics of the mechanical gyro coupled with the system electronics.

Figure 3-17 shows a block diagram of the entire experimental setup. A photograph of the test bench, showing the digital scope, shakers, power amps, electronics, and power supplies appear in figure 3-16.The configuration will be modified for various tests; I may use one or the other shaker, or different data acquisition systems. Notice that tests can be run closed loop using the reference accelerometer; it is possible to have the signal analyzer drive the shaker to a particular acceleration amplitude by feeding back the accelerometer signal. This technique was used for some tests where we wanted to maintain a particular vibration amplitude.

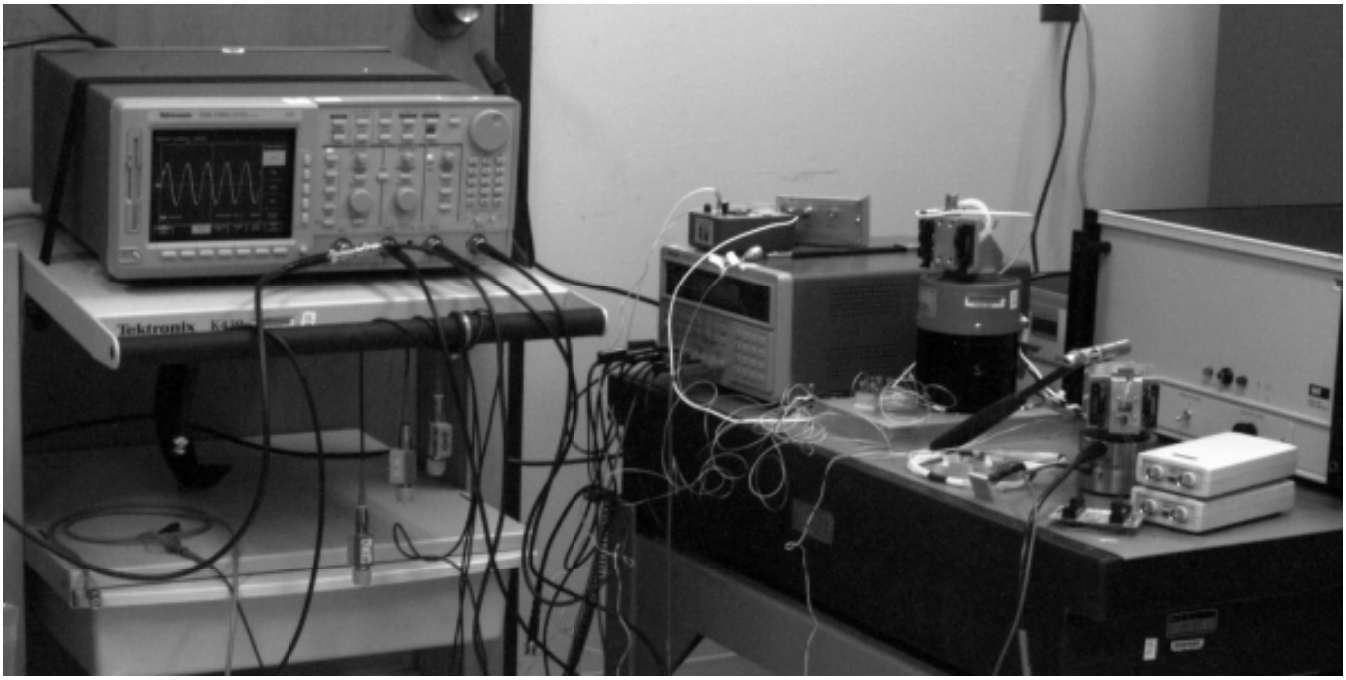

Figure 3-16: Photograph of Test Area

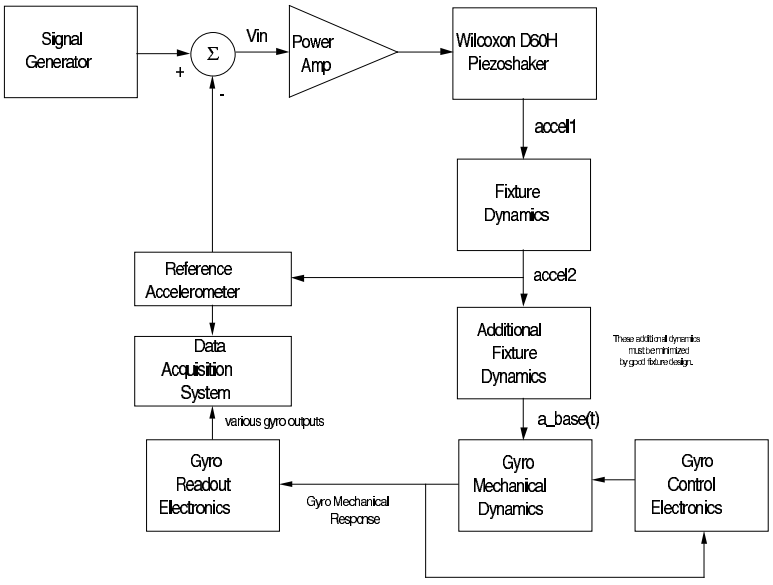

Figure 3-17: Block Diagram of One Configuration of the Experimental Setup

Chapter 4

Characterization Testing

A number of different tests have been conducted to characterize the test units prior to vibration and impact testing. This chapter will describe the different characterization tests, their aims, and the theory behind their interpretation.

4.1 Baseline Testing

For each gyro, baseline testing is conducted to determine central parameters. These tests are conducted with the gyro running closed loop and undergoing no vibration. The parameters measured here allow computation of most of the lumped element values used in the mechanical models of section 2.2.1, determination of the scale factors for the various capacitive sensors and drives, (sections 2.3.1, 2.3.2, 2.3.3), and measurement of overall gyro performance.

1. *Modal frequencies* allow computation of many mechanical model parameters
2. *Scale factor* testing gives a measure of sensitivity to rate, which lumps many model parameters together.
3. *Bias measurements* give a normal operation level of various gyro outputs, thus indicating whether the gyro is functional.

The modal frequencies of the gyro can be determined by looking at a PSD of AC-out and the motor position signal. The motor position signal gives the motion of

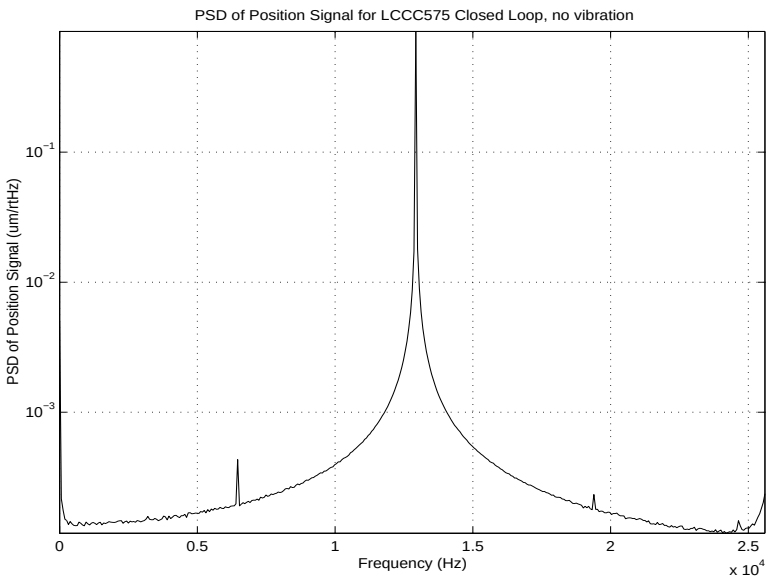

Figure 4-1: PSD of Position Signal for LCCC575 showing Tuning Fork Frequency

the left proof mass in the plane, and so is almost a perfect sine wave at the tuning fork frequency. Figure 4-1 gives a PSD showing the predominance of tuning fork frequency in the position signal.

Since AC-out is the sense preamp output multiplied by a constant gain, it contains information not only about sense modes but also about in-plane modes due to charge injection effects. (section 2.3.2) Thus, all four major modes are sometimes visible in AC-out. A typical example of a PSD of AC-out is given in figure 4-2

The two large peaks in the PSD at roughly 6.5 kHz and 19.5 kHz are artifacts of the electronics. The two smaller peaks, at 12.930 kHz and 14.670 kHz, are the tuning fork and sense modal frequencies, respectively. The tuning fork mode is intentionally excited by the motor loop, and, due to mismatches in the two sides of the gyro, injects some charge into the sense preamp, producing a small signal on AC-out. The sense frequency is preferentially sensed by the sense chain, so any small motion caused by crosscoupling is seen at AC-out. Depending on the unit, hula and out-of-plane can also be excited. Since out-of-plane is rejected by the sense chain, it is usually not visibile on AC-out. Hula motion is not intentionally excited, but sometimes can be

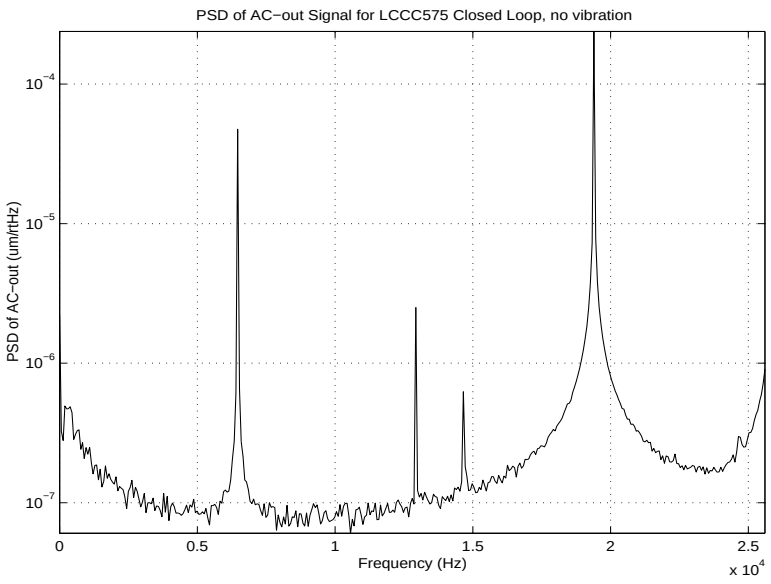

Figure 4-2: PSD of AC-out for LCCC575 showing modal frequencies and excitation signal

excited by spring mismatch. In this particular unit, no hula spike is seen in AC-out.

From these two PSDs, and, as needed, narrowband power spectra of AC-out and the motor position signal, all of the closed loop modal frequencies can be determined. From the modal frequencies, many of the mechanical model parameters are computed. Section 2.2.2 gives the relevant relationships.

In addition to modal frequencies, scale factor is measured during baseline testing. The gyro and EDM3 board are mounted on a servo controlled rate table. The gyro is set up for normal operation, and the rate-out signal is measured while the gyro is undergoing +1 rad/s and -1 rad/s rotation. Scale factor is therefore directly computed as

$$SF = \frac{V_{rateout1} + V_{rateout2}}{2rad/s} \tag{4.1}$$

Where $V_{rateout1}$ is for a rotation of +1 rad/s, and $V_{rateout2}$ is for a rotation of -1 rad/s.

Every unit used in vibration and impact tests has undergone baseline testing. This gives much of the information needed for modeling and prediction of response,

and also ensures that the unit is fully functional.

4.2 Q Tests

In addition to the spring values determined from modal frequency measurements, the gyro models developed in section 2.2.1 necessarily include damping. Damping is very important to accurately measure, as it determines how quickly transients will damp out, and also the final steady state response for an input near resonance.

Q measurements were conducted by exciting a particular gyro mode, such as the hula or sense mode, and then abruptly setting the input to zero. At this point, we start recording the gyro motion, and watch the amplitude ring down. The time constant associated with the ring-down allows computation of Q. Q tests are done open loop; the damping value we are looking for is a mechanical property of the gyro.

There are two Qs for each unit, one associated with the motor axis damping term b_x (see section 2.2.1), and one associated with sense axis damping, b_y. From Q, damping is computed,

$$b_x = \frac{\sqrt{\bar{k_x}\bar{m}}}{Q_x} \tag{4.2}$$

and, likewise,

$$b_y = \frac{\sqrt{\bar{k_y}\bar{m}}}{Q_y} \tag{4.3}$$

The envelope of ringdown, from the models in section 2.2.1, is

$$X(t) = X_0 e^{\frac{-f_{mode}\pi}{Q}t} \tag{4.4}$$

Where:

$X(t)$ = envelope of the ringdown

X_0 = initial amplitude of the excited mode

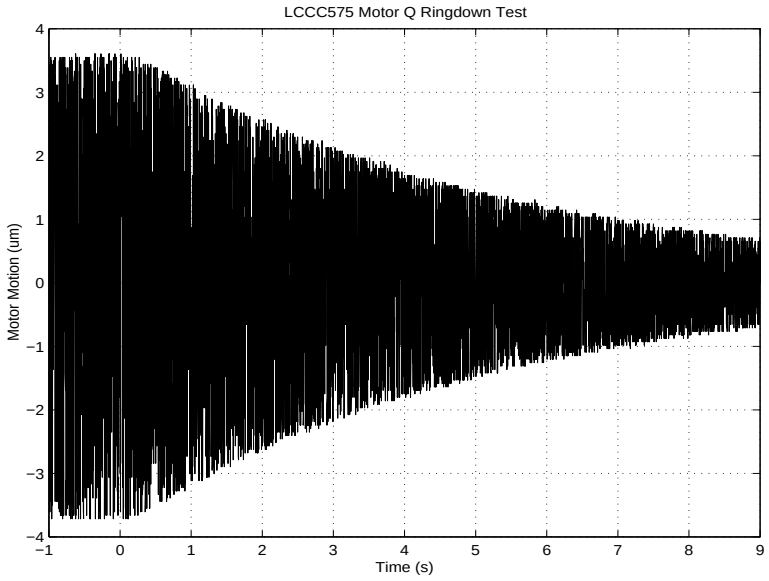

Figure 4-3: Position Signal during Ringdown Motor Q Test, LCCC575

f_{mode} = cyclic frequency of the excited mode, detrmined from baseline tests

Q = Q for either the sense or motor axis, depending on which mode is being driven

The particular mode being used for the Q test can be excited either with vibration at the modal frequency (vibration is best at exciting the parallel modes: hula and out-of-plane), or with an electrostatic force delivered using the outer combs for in-plane modes or the sense plates for out-of-plane modes.

Electrostatics were used to excite the tuning fork mode for motor Q tests because they give a cleaner excitation and are more similar to real gyro operation. However, it is difficult to sense and drive on sense at the same time since there is only one set of sense caps; therefore I use a mechanical vibration excitation for sense Q tests.

Typical data is shown in figure 4-3. Excitation is turned off at t=0 s. Figure 4-4 shows the envelope and the bestfit exponential. The exponent of the exponential determines Q according to equation 4.4. For this particular case, the motor Q comes out to be 217,700.

Similar data has been taken for every test unit, summarized in table 4.1.

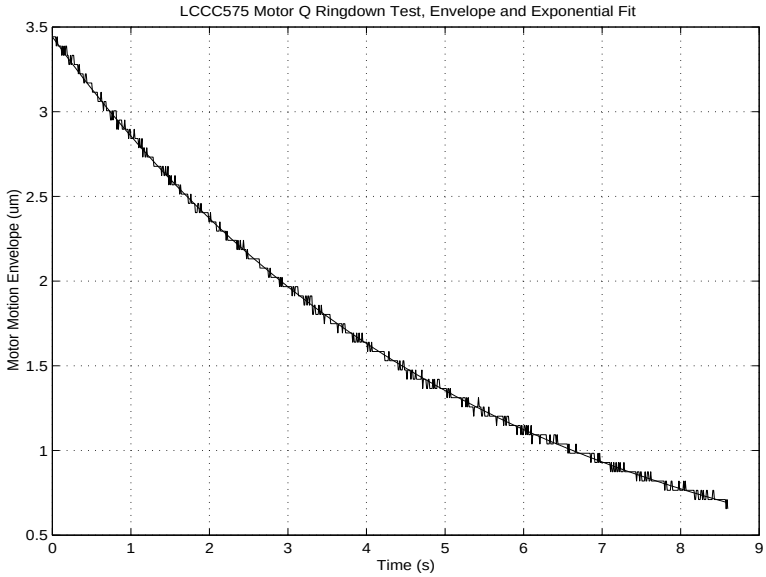

Figure 4-4: Envelope and Exponential Fit for Ringdown Motor Q Test, LCCC575

Unit	Motor Q	Sense Q
LCCC560		11.500
LCCC561	162,200	12,000
LCCC574	173,000	12,100
LCCC575	217,700	15,600
LCCC576	188,230	14,100
LCCC577	198130	22,300

Table 4.1: Summary of all RingDown Q Tests

4.3 Nonlinear Spring Testing

As discussed in section 2.2.5, cubic spring nonlinearities exist in the mechanical gyroscope. These are most obviously manifested as a shift in resonant frequency due to a change in amplitude of motion. The computations in section 2.2.5 indicate that there should be a linear relationship between the resonant frequency (that is, the driving frequency corresponding to maximum response), and the amplitude of motion squared. Equation 4.5 gave the relationship for small amplitudes X,

$$\omega_n \approx \sqrt{\frac{k}{m}} + \frac{3}{8m}\sqrt{\frac{m}{k}}k_3 X^2 + \cdots \tag{4.5}$$

As mentioned in section 2.2.5, beam effects cause spring stiffening with increasing amplitude of motion. Electrostatic forces in the capacitors, on the other hand, cause softening due to the inherently nonlinear nature of the forces in a parallel plate capacitor (see equation 2.41). Although the comb drive caps are not as inherently nonlinear, experimental results indicate that spring softening occurs on the motor axis as well.

Due to electrostatic spring softening, the resonant frequency will decrease with the amplitude of motion. This effect produces a characteristic *shark fin* structure in the frequency response curve, as frequency is swept downward while driving at a constant force amplitude. As frequency is decreased, we approach the mechanical resonance and the amplitude of the response increases. Larger amplitudes cause a downward shift in effective resonant frequency, so that, instead of dropping back down to a lower amplitude, we stay at the high magnitude. At some point the frequency gets too low and the driving frequency drops below the nonlinear resonance, causing the amplitude of the response to fall sharply.

A typical example of cubic spring softening can be seen in a test conducted on LCCC561 motor axis. In this test, we do a narrowband vibration sweep near the hula frequency. At low drive amplitudes, a clean resonance is seen at 13.035 kHz. However, for vibration amplitudes resulting in large enough motion, nonlinear spring softening is evident. Figure 4-5 shows the frequency response from vibration input

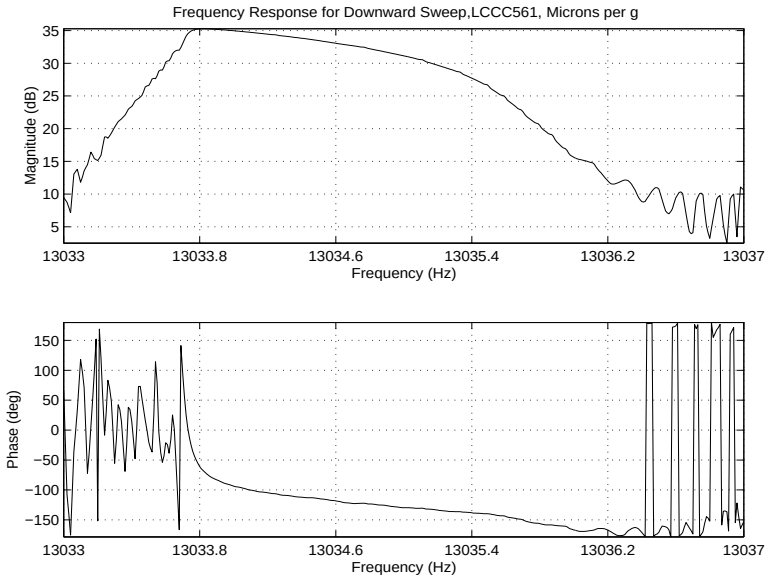

Figure 4-5: Frequency Response for LCCC561 Showing Spring Softening Shark Fin

in [g] to motion of the proof mass in the plane [μm]. The phase looks terrible away from resonance because the signal was too small and lost in noise.

If the drive frequency is swept up instead of down, no shark fin is observed. During a upward sweep, significant amplitude is not built up until we reach the linear resonant frequency. The amplitude of motion created at this point softens the spring, thus decreasing the effective resonant frequency. However, since we are sweeping up, the next frequency step brings us to a higher frequency, so the nonlinearity does not increase response.

Figure 4-6 shows the linear fit of amplitude of motion squared vs. resonant frequency. Equation 4.5 predicts this linear relationship, and gives the relationship needed to determine the cubic spring constant. With the linear fit given in the figure, $Y = AX + B$, the cubic spring constant, from equation 4.5, is

$$k_3 = B \cdot A \cdot \frac{8m}{3}$$

The mass of the gyro proof mass, m, is $3.6{\cdot}10^{-8}$ kg. Taking into account the units

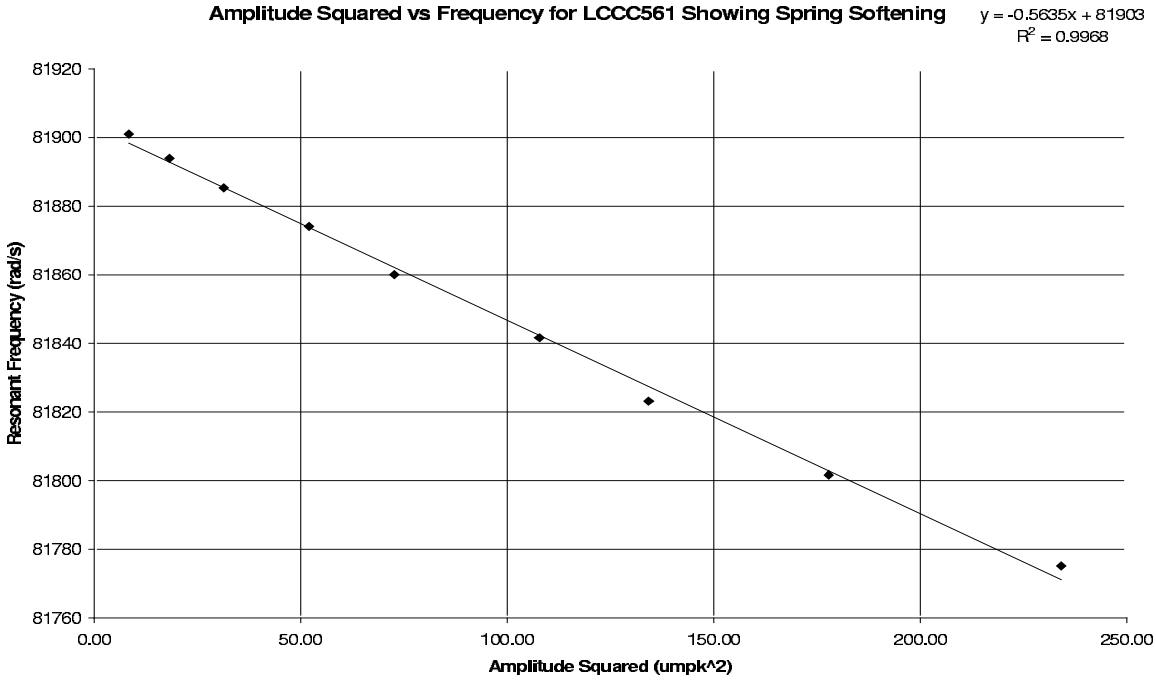

Figure 4-6: Linear Fit for Determination of LCCC561 Spring Softening

Unit	Motor Flexure Linear Stiffness $\frac{N}{m}$	Cubic Spring Term $\frac{N}{m^3}$	Percent Change in Stiffness at 10 μm amplitude
LCCC561	288.8	-4.4·10^9	0.15%
LCCC574	220.2	-3.1·10^9	0.14%
LCCC575	237.7	-3.4·10^9	0.14%

Table 4.2: Summary of all Motor Cubic Spring Softening Tests

as appropriate, k_3 is computed. For LCCC561 motor axis, the spring softening cubic spring constant is $k_3 = -4.4 \cdot 10^9 \frac{N}{m^3}$, resulting in a total change in spring stiffness of $-0.44 \frac{N}{m}$ when the gyro is running at the nominal amplitude of 10 μm. This represents a change in spring stiffness of only 0.15% (recall that the linear motor flexure spring stiffness can be computed from tuning fork frequency as described in section 4.1, for this unit it comes out to be 288.8 N/m). In general, all the cubic spring nonlinearities are quite small, and can usually be neglected in the model. Table 4.2 gives the results for identical tests conducted on three test units.

In all cases, the cubic spring softening causes only about 0.14 % change in spring

stiffness when the gyro is running at nominal amplitudes of 10 μm. Thus, it is safe to neglect the cubic spring effects in the models, although remembering that this can cause a shift in resonant frequency of a few hundredths of a percent.

Chapter 5

Open Loop Vibration Testing

Open loop vibration testing of the tuning fork gyro helped to verify the linear model developed in section 2.2.1, and to explore the mechanical response of the gyro plant to vibration. This section goes through some computations of the expected response to both sinusoidal and random vibration. Theoretical results are compared to experiment.

For open loop testing the gyro was plugged into the belljar electronics, which allow arbitrary signals to be placed on the motor drive combs, inner motor combs, and sense plates. Output signals such as motor position and sense preamp-out are examined under different conditions. (see section 3.1) Open loop operation is simpler to understand, since there is no feedback and no signal conditioning.

5.1 Summary

There are a few essential conclusions drawn from the results outlined in this chapter:

- The mechanical models of section 2.2.1 predict the correct order of magnitude for gyro open loop response to both sinusoidal and random open loop vibration. However, substantial differences are seen between expected and observed response, at worst on the order of a factor of 3.
- Response of anti-parallel modes gives an estimate of motor and sense spring

mismatch. Spring mismatch is between 0 and 2%.

- Estimates for the maximum safe levels for both random and sinusoidal vibrations near each modal frequency are presented.

- It is important to consider not only gyro resonant modes, but also modal response of the mounting structure. In addition to gyro modal frequencies, fixture modal frequencies are seen in gyro response. This will be true not only for this test fixture, but for any mounting system used during normal gyro operation.

- The time constant for the growth of gyro response to vibration is on the order of 1 s for the motor axis, and 0.1 s for the sense axis.

5.2 Open Loop Modeling

In order to compute the expected response of the gyro to vibration, transfer functions are derived. Taking the model of section 2.2.1, the frequency response for the motion of the left proof mass due to vibration of the substrate can be computed.

For these computations, assumptions have to be made about axis cross-coupling and spring and mass mismatch. I will assume that cross coupling between the two axes can be neglected, and that mismatch in the masses is also negligible.

To simplify the equations, the following substitutions are made for the motor axis (refer to section 2.2.1 and 2.2.2 for the definition of the lumped element values and the equations deriving them from modal frequencies):

$$\begin{aligned} K_{x11} &= \frac{k_{x1}k_x + k_{x2}k_{x1}}{k_x + k_{x1} + k_{x2}} \\ K_{x12} &= K_{x21} = \frac{k_{x1}k_{x2}}{k_{x1} + k_{x2} + k_x} \\ K_{x22} &= \frac{k_{x2}k_x + k_{x2}k_{x1}}{k_x + k_{x1} + k_{x2}} \end{aligned} \tag{5.1}$$

Similarly, for the sense axis model:

$$
\begin{aligned}
K_{y11} &= \tfrac{k_{y1}k_\theta + L^2 k_{y1}k_{y2}}{k_\theta + L^2(k_{y1}+k_{y2})} \\
K_{y12} = K_{y21} &= \tfrac{-L^2 k_{y1}k_{y2}}{k_\theta + L^2 k_{y1} + L^2 k_{y2}} \\
K_{y22} &= \tfrac{k_{y2}k_\theta + L^2 k_{y2}k_{y1}}{k_\theta + L^2(k_{y1}+k_{y2})}
\end{aligned}
\tag{5.2}
$$

With these substitutions and assumptions, the transfer function becomes, as described in section 2.2.1 and appendix A,

$$
\frac{X_1}{A_{sx}} = \frac{-m^2 s^2 - b_x m s - m(K_{x22} + K_{x12})}{m^2 s^4 + 2b_x m s^3 + (b_x^2 + mK_{x11} + mK_{x22})s^2 + b_x(K_{x11} + K_{x22})s - K_{x12}^2 + K_{x11}K_{x22}} \tag{5.3}
$$

Where:

X_1 is the Laplace transform of the displacement of the left proof mass in the motor direction relative to the gyro substrate

A_{sx} is the Laplace transform of the acceleration of the substrate in the motor direction relative to inertial space

s is the Laplace transform of $\frac{d}{dt}$

In the case of no spring mismatch, $k_{x1} = k_{x2} = k_{xf}$, and equation 2.19 reduces to

$$
\frac{X_1}{A_{sx}} = \frac{-m}{ms^2 + b_x s + \frac{k_{xf}k_x}{k_x + 2k_{xf}}} \tag{5.4}
$$

For the sense axis,

$$
\frac{Y_1}{A_{sy}} = \frac{-m^2 s^2 - b_y m s - m(K_{y22} + K_{y12})}{m^2 s^4 + 2b_y m s^3 + (b_y^2 + mK_{y11} + mK_{y22})s^2 + b_y(K_{y11} + K_{y22})s - K_{y12}^2 + K_{y11}K_{y22}} \tag{5.5}
$$

Where:

Y_1 is the Laplace transform of the position of the left proof mass in the sense direction relative to the gyro substrate

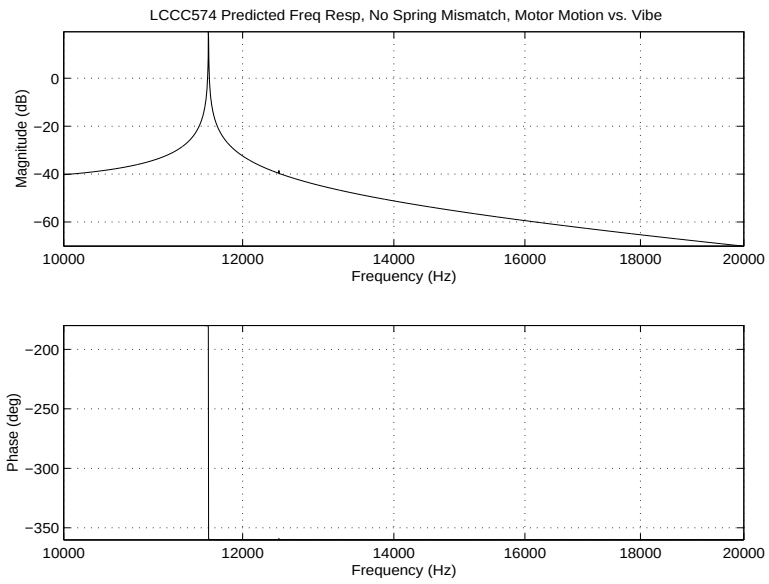

Figure 5-1: Predicted Frequency Response for Motor Vibration, no spring mismatch

A_{sy} is the Laplace transform of the acceleration of the substrate in the sense direction with respect to inertial space

In the case of no spring mismatch, $k_y = k_{y1} = k_{y2}$, and equation 2.21 reduces to

$$\frac{Y_1}{A_{sy}} = \frac{-m}{ms^2 + b_y s + k_y} \tag{5.6}$$

However, spring mismatch cannot be neglected, especially since a small mismatch can have a dramatic effect on the frequency response. With no mismatch, the antiparallel modes are not excited by vibration. Addition of any small mismatch allows them to be excited. Thus, the level of steady state response for the antiparallel modes gives an indication of spring mismatch.

Figure 5-1 gives the frequency response for the motion of the left proof mass in the plane due to motor axis vibration in the plane, for the case of no spring mismatch. Figure 5-2 is the same transfer function, but with 2% spring mismatch in the motor flexures. The model parameters were determined from the Q and frequency data for LCCC574. In both cases, the magnitude units are dB $\mu m/g$.

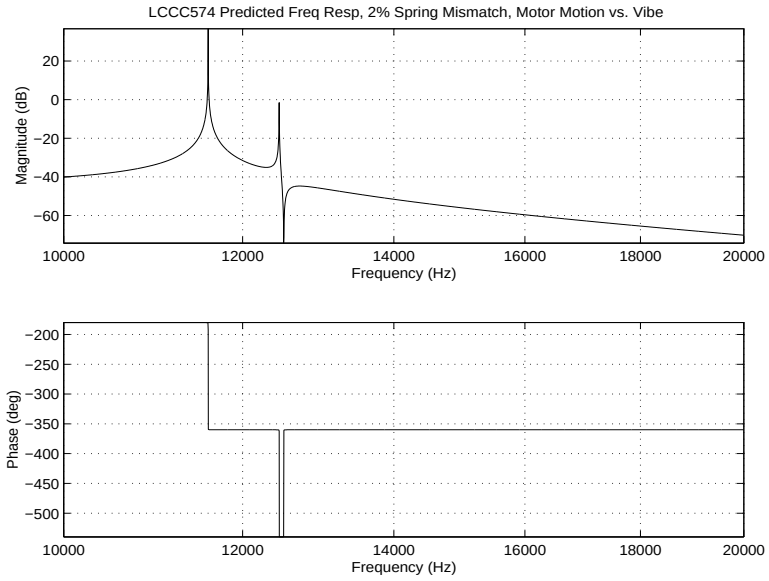

Figure 5-2: Predicted Frequency Response for Motor Vibration, 2% spring mismatch

Similarly, figure 5-3 gives the frequency response for the motion of the left proof mass out of the plane due to sense axis vibration. This is for the case of no spring mismatch. Figure 5-4 shows the frequency response with a 2% spring mismatch in the sense flexures. In both cases, the magnitude units are dB $\mu m/g$.

The frequency response functions shown in figure 5-1 through 5-4 are used for predicting the steady state response to vibration throughout the rest of this chapter.

5.3 Sinusoidal Vibration

Sinusoidal vibration testing of open loop gyro operation shows high sensitivity to mechanical vibration at the hula and out of plane frequencies. The gyros have a much lower, but still measurable, sensitivity to vibration at tuning fork and sense frequencies. The gyro is insensitive to vibration at every other frequency in my test range.

Gyros LCCC561, LCCC574, and LCCC575 were subjected to sinusoidal vibration throughout the range of shaker operation. Response was seen only at the modal

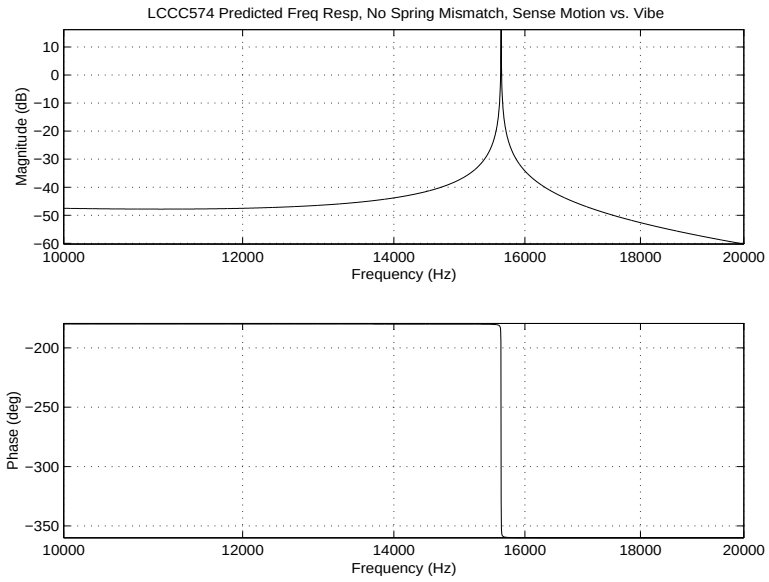

Figure 5-3: Predicted Frequency Response for Sense Vibration, no spring mismatch

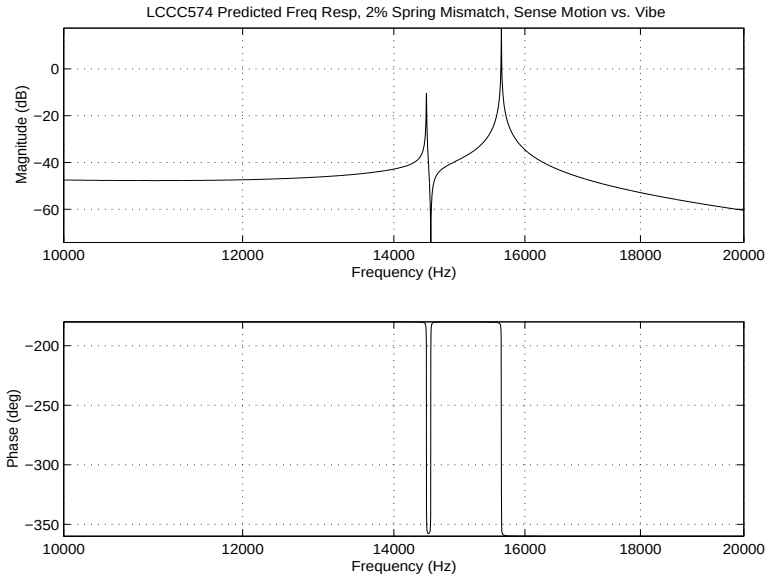

Figure 5-4: Predicted Frequency Response for Sense Vibration, 2% spring mismatch

Unit	Hula Mode (μm/g)	Tuning Fork Mode (μm/g)	Sense Mode (μm/g)	Out-of-Plane Mode (μm/g)	Deduced Flexure Spring Mismatch
LCCC561, predicted	214	2%: 9.21		9.87	
LCCC561, measured	63			0.63	
LCCC574, predicted	300	1%: 8.62 2%: 16.5	1%: 0.41 2%: 0.84	12.03	
LCCC574, measured	826	7.54	0.30	4.36	motor: ~0.9% sense: ~0.72%
LCCC575, predicted	331	1%: 8.85 2%: 16.87	1%: 0.35 2%: 0.72	14.00	
LCCC575, measured	501	0.44	0.69	10.83	motor: ~0.05% sense: ~1.95%

Table 5.1: Summary of Steady State Open Loop Sinusoidal Vibration

frequencies. The measured steady state response, along with the predicted response level, is recorded in table 5.1. Recall from section 4.3 that cubic spring nonlinearities cause the resonant frequency to decrease with amplitude, as seen in the sharkfin plots shown in that section. In the table, the steady state response is recorded at the nonlinear resonance; this is the frequency where the largest gyro response is seen. Measurements were taken at a number of different vibration levels, and averaged to get the results shown in table 5.1. All predicted responses come from the transfer functions given in equations 5.3 and 5.5. The gain is computed at the resonant frequency. Predictions given in the table for anti-parallel frequency response are given for a spring mismatch of 1% and 2% as noted.

Qualitatively, these results agree well with my mechanical model of the gyro. (see section 5.2) With perfectly matched springs and masses, it should be impossible to excite the antiparallel (tuning fork and sense) modes with mechanical vibration of the substrate. However, since the gyros are not perfectly balanced, there will be some response at the antiparallel resonances, but this response is much smaller than the response seen at the parallel resonances. From the measured response of the anti-parallel modes, we can deduce the spring mismatches for both units along both axes, as noted in the table.

The steady state vibration levels seen are on the correct order of magnitude pre-

dicted by the models, but do not agree as well as might be hoped. The worst errors are seen in sinusoidal vibration of the parallel modes for LCCC574 and LCCC561. In the case of LCCC574, the model underestimates response. For LCCC561, response is lower than predicted. These results indicate that response levels predicted from the linear models should be taken as approximate. In determining safe levels of gyro operation, we should take the highest response level seen between predicted and measured values.

From these results it is evident that a sinusoidal vibration at a resonant frequency could quickly destroy the gyro. As described in section 2.4, displacement amplitudes of greater than 25 μm in the motor direction will cause the combs to contact. Hula motion of amplitudes greater than 10 μm can cause the motor loop to lose lock (see section 7.3.4).In the sense direction, displacements of greater than 2 μm can cause snapdown. According to the data in table 5.1, the largest marginally safe vibration at the resonant frequencies is on the order of

- Hula Frequency : 0.012 $[g]$
- Tuning Fork Frequency :2.5 $[g]$
- Sense Frequency : 2.9 $[g]$
- OOP Frequency : 0.1 $[g]$

5.4 Random Vibration

Random vibration of the fixture and gyro causes the structure to resonate, and thus drives gyro proof-mass motion. Although the input to the shaker system is white noise, shaker and fixture frequency response shapes the input into a more complex spectrum. This acceleration signal is what ends up driving the mechanical gyro plant. The sharp gyro resonances can again be seen to shape the signal, and so the resulting output clearly shows the gyro fundamental modes. In addition, any fixture resonances in the band are excited, and drive the gyro. Thus, strong fixture resonances can also

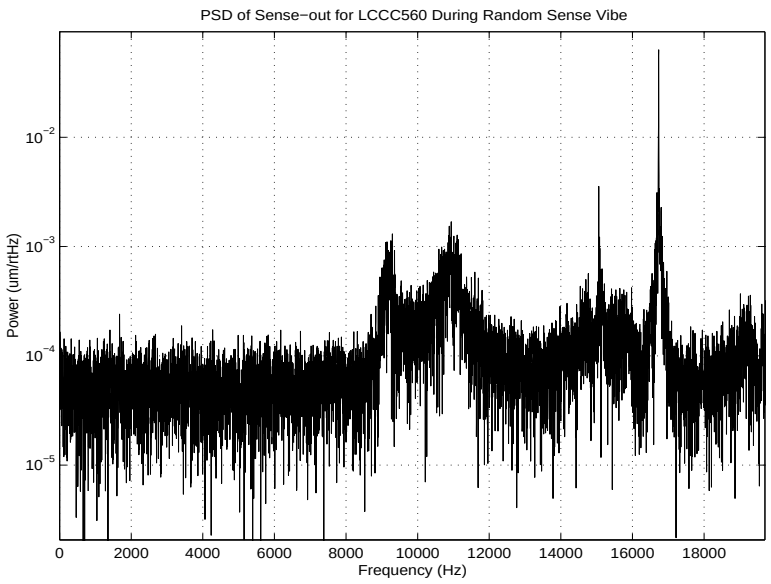

Figure 5-5: PSD of Sense Preamp Out for LCCC560 during Random Vibration in Sense Fixture

be seen in gyro response. Figure 5-5 is a PSD of the sense preamp-out signal for gyro LCCC560 during a random vibration test. The gyro was mounted in the sense axis fixture which experienced $7.64 \cdot 10^{-3}$ $g/\sqrt{Hz}$ white noise delivered by the Wilcoxon piezoshaker.

The two high frequency spikes in the PSD, at 16.729 kHz and 15.061 kHz, are the out-of-plane and sense frequencies, respectively. Both of these modes are excited by random vibration, although the response at out-of-plane is much greater than the response at sense, as predicted by the mechanical model. (See section 5.2)

The lower frequency spikes, which are wider and less cleanly defined, come from two of the strong fixture modes. Recall from section 3.3.2 that there are two strong sense fixture modes at 9.179 and 10.730 kHz. These are the two strongest fixture modes in the lower frequency band (below gyro resonances). This is an important result to be aware of; any gyro operating under real environmental conditions will respond not only at its own resonances, but also any resonances of the structure on which it is mounted.

In addition to examining the frequency spectrum of gyro motion, steady state response to random vibration (modeled as white noise) was measured. Again, the models of section 5.2 are used to predict gyro response. We take the frequency response curves from section 5.2, multiply them by the white noise spectrum, and integrate across the resonant peaks to determine the total power output expected at a given frequency. Equation 5.7 gives the relationship:

$$X_{rms}^2 = \int_{\omega_1}^{\omega_2} |H(j\omega)|^2 S(\omega)\ d\omega \tag{5.7}$$

Where:

X_{rms} = Root Mean Square value of the response in the frequency band $[m_{rms}]$

ω_1, ω_2 = Frequency band of interest, such as the band around a particular modal frequency. $[rad/s]$

$H(j\omega)$ = Transfer function from substrate acceleration to proof mass motion derived from the mechanical model $[m/g]$

$S(\omega)$ = single sided PSD of the input acceleration spectrum in units of $[g^2/Hz]$

Measurements of the gyro response at a particular modal frequency due to random vibration were taken using the spectrum analyzer described in section 3.5.1. The reference accelerometer measured the delivered acceleration level. Modal spikes in the PSD of sense and motor preamp outputs were integrated to get the total RMS level of motion at the various frequencies.

Table 5.2 summarizes the results, and compares them with predicted response levels. For the antiparallel modes, the spring mismatches computed in section 5.3 from sinusoidal steady state response were used. Again, the measured results are on the right order of magnitude, but errors are considerable.

Using the data in table 5.2, the maximum safe random vibration level sustainable at the gyro resonant frequencies can be determined. Just as above in section 5.3, displacement amplitudes of greater than 25 μm in the motor direction will cause the

Unit	Hula Mode (μm/(g/√Hz))	Tuning Fork Mode (μm/(g/√Hz))	Sense Mode (μm/(g/√Hz))	Out-of-Plane Mode (μm/(g/√Hz))
LCCC561, predicted	**82.99**	**3.47**	**0.68**	**14.69**
LCCC561, measured	**56.39**	**2.65**	**0.75**	**2.86**
LCCC574, predicted	**99.93**	**2.52**	**0.48**	**17.01**
LCCC574, measured	**234.49**	**2.52**	**2.04**	**10.48**
LCCC575, predicted	**106.05**	**0.14**	**0.88**	**18.03**
LCCC575, measured	**195.38**	**0.27**	**7.82**	**21.56**

Table 5.2: Summary of Steady State Open Loop Random Vibration

combs to contact. Hula amplitudes of greater than 10 μm can cause motor loop to lose lock (see section 7.3.4). In the sense direction, displacements of greater than 2 μm can cause snapdown. (see section 2.4) Thus, the largest allowable random vibration level in a particular resonant frequency band is on the order of

- Hula Frequency : 0.04 $\left[g/\sqrt{Hz}\right]$
- Tuning Fork Frequency :7 $\left[g/\sqrt{Hz}\right]$
- Sense Frequency : 0.2 $\left[g/\sqrt{Hz}\right]$
- OOP Frequency : 0.1 $\left[g/\sqrt{Hz}\right]$

5.5 Ring Up Tests

Vibration can cause substantial gyro steady state response, to a level which is potentially damaging to the gyro structure. However, the gyro does not build up to its steady state response level immediately. The time constant associated with growth of the steady state response depends on gyro damping. From the linear model, the response should grow according to equation 5.8,

$$x(t) = A\left(1 - e^{-t/\tau}\right) \tag{5.8}$$

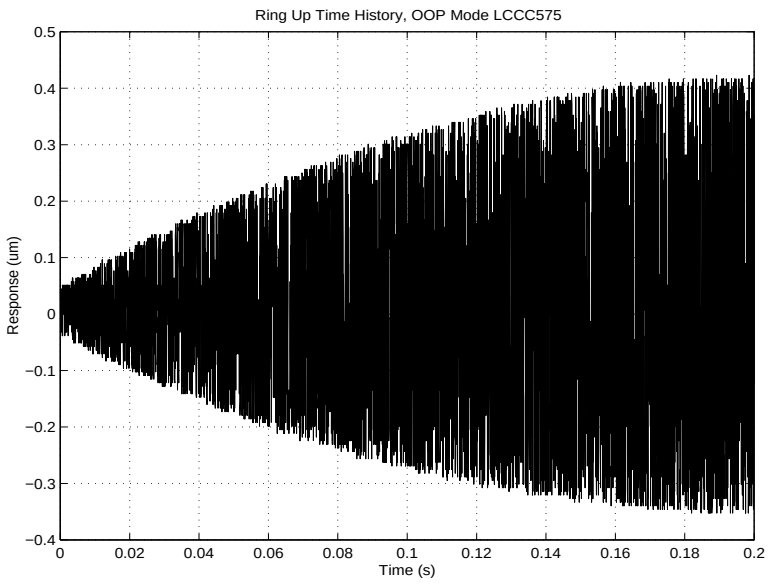

Figure 5-6: OOP Ring Up Time History of LCCC575

Where the time constant, τ is related to Q by

$$\tau = \frac{Q}{f_n \pi} \tag{5.9}$$

Where:

f_n = natural frequency for the mode under consideration.

Q = Q for the axis under question

Q and modal frequencies are known for each test unit, so time constants for the growth of gyro response to vibration can be directly computed. Open loop transient ring-up testing of the gyros was conducted to verify these predictions. To test ring up time, the gyro was run open loop. The gyro starts at rest. At t=0 a sinusoidal vibration at either the hula or out-of-plane frequency was initiated, and a time history of gyro response recorded. Figure 5-6 is a typical response curve. Note that although the graph looks filled in, it is really just many cycles of a growing sinusoid.

From this sort of data, the envelope of the growing response can be found. The envelope should have the form of equation 5.8. Finding the best values for the pa-

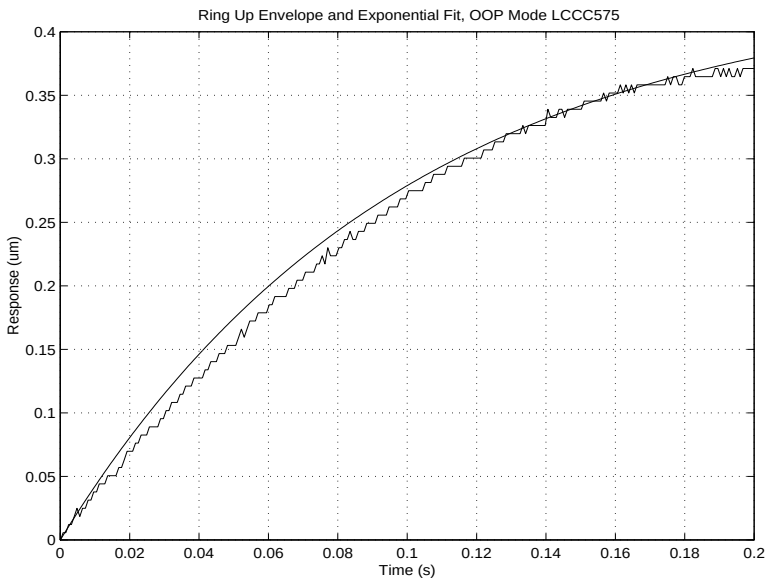

Figure 5-7: LCCC575 OOP Ring Up Envelope and Best Exponential Fit

rameters A and τ is non-trivial, but can be done iteratively by guessing a value for A, then taking natural logs to produce:

$$\ln(A - x) = -(1/\tau)\, t \tag{5.10}$$

With an initial guess for A, a least squares linear fit will produce the best choice for τ. At this point, we update the value of A, and recompute the least squares. If the fit improves, we keep moving A in the same direction. If the error increases, we move A in the other direction by a smaller amount. This procedure is repeated, converging on the best value for A and τ. By using this algorithm, ring-up time constants for various units have been measured. Figure 5-7 shows the envelope for the data in figure 5-6, as well as an exponential fit. Table 5.3 summarizes the predicted and actual time constants for various ringup tests.

The data in table 5.3 is important because it gives an idea of how long a gyro can survive high vibration levels; if the duration is much shorter than the time constant, the response will not have time to build up to dangerously high steady state levels. Agreement between measured and predicted values is decent, but there are some

Unit	Motor Q	Predicted Hula Ringup Time Constant (seconds)	Measured Hula Ringup Time Constant (seconds)	Sense Q	Predicted OOP Ringup Time Constant (seconds)	Measured OOP Ringup Time Constant (seconds)
LCCC561	**162,000**	**3.48**	**3.71**	**12,000**	**0.21**	**0.34**
LCCC574	**173,000**	**4.80**	**1.31**	**12,100**	**0.25**	
LCCC575	**217,700**	**5.80**		**15,600**	**0.30**	**0.10**

Table 5.3: Summary of Ring Up Tests

errors, particularly for the hula test of LCCC574. Still, the ringup time for motor response is on the order of 1 s. For the sense axis, the time constant is on the order of 0.1 s.

Chapter 6

Low Frequency Closed Loop Vibration Testing

During normal gyro operation, the gyro runs closed loop, feeding back the motor position signal via the motor loop. Both the motor loop and sense chain systems were described in section 2.3.4. While running closed loop, the mechanical plant of the gyro is the same as before, thus the results of chapter 5 still apply. Now, however, feedback is used to drive certain types of motion.

In particular, the motor feedback loop works to keep the motor axis oscillating in tuning fork mode at an amplitude of 10 μm. This motion is necessary for correct operation of the sense chain, which assumes a particular level of Coriolis acceleration. As described in section 2.2.3, Coriolis acceleration depends on the motion of the masses in the plane. A large amplitude of in-plane motion will create higher Coriolis accelerations for a given rate. (see equation 2.12) Thus, constant amplitude motor motion is a requirement for the gyro to accurately sense rate.

Secondly, the signals available for measurement during closed loop operation are different than during open loop. The most significant closed loop gyro output is the *rate-out* signal, which is the estimate of rotational rate experienced by the gyro. Achieving a good estimate of rate is the final goal of gyro operation. Rate-out is generated, as described in section 2.3.4, by multiplying the sense-preamp output by the motor velocity clock, and low pass filtering the product. The low pass filter has

a break frequency of 100 Hz.

In addition to rate-out, both the motor and sense preamp outputs are available, gained up by some amount. The motor preamp-out gives a direct measure of in-plane motion of the left proof mass. We call this the *position signal* or *psig*. The sense preamp-out gives a measure of the differential motion of the two masses out of the plane, and also includes charge injection effects (see section 2.3.2). The gained up sense-preamp output is available, and will be referred to as *AC-out*.

All of these effects must be considered to understand closed loop vibration testing, and will contribute to the results described in this chapter and in chapters 7 and 8.

Particular concerns were raised about the sensitivity of the TFG14 to low frequency random and sinusoidal vibration. Low frequency vibration is more prevalent in the gyro operating environment. To investigate low frequency effects, four hard-mounted unbalanced TFG14-14s underwent sinusoidal vibration testing in the 1-3 kHz range using the Labworks electromagnetic shaker. Two of these units were subjected to random vibration in the 0-6 kHz range, using the same shaker. Results indicate substantial sensitivity to sinusoidal angular vibration at the difference between the sense and drive frequencies, but very low sensitivity to vibration at any other frequency in the range. No response was seen to the levels of vibration delivered at other frequencies (5 g_{pk-pk} sinusoidal).

Vibration at the difference frequency, probably resulting in structure rotation at the same frequency, can quickly saturate the sense preamp output (at levels between 5 g_{pk-pk} and 10 g_{pk-pk} depending on the unit). However, little response is seen on rate-out, since the difference frequency is on the order of 1 kHz, a full decade above the 100 Hz bandwidth of the gyro.

Random vibration testing indicates that some false rate measurements are generated on rate-out at the difference between the hula and drive frequencies, and the difference between sense and drive. However, most of the rate measured by the gyros during random vibration seems to be real rotation of the test structure. For the most part, the gyros are insensitive to the levels (0.1–0.01 $g_{rms}/\sqrt{Hz}$, which is about 1-10 g_{rms} in a 6 kHz bandwidth) of random vibration we are able to deliver using the

LabWorks shaker. This is discussed in section 6.3.

6.1 Summary

There are a few essential conclusions drawn from the results outlined in this chapter:

- Vibration at the difference between the sense and drive frequencies, creating rocking of the structure at this frequency, excites sense mode motion due to Coriolis effects. This can quickly saturate the AC-out electronics. (see section 2.4.1)
- Vibration at this difference frequency ($\omega_{sense} - \omega_{tunefork}$)causes some small errors on rate-out at the difference frequency and the sense frequency.
- Vibration at this frequency also has a small, but measurable, effect on the mean of rate-out.
- Much of the signal on rate-out seen during low frequency random vibration comes from real rotation of the test structure at structure resonances.
- Random vibration excites the hula and sense modes (particularly hula), due to high frequency components in the applied random vibration. These couple through into rate out and are demodulated, creating errors on rate-out at the difference between tuning fork and hula, and tuning fork and sense.
- No sensitivity was seen to low frequency components of random vibration.

6.2 Sinusoidal Vibration at the Difference Between Sense and Drive

Low frequency (0-3 kHz) sinusoidal vibration testing of 4 TFG-14 units has been conducted. Results indicate that the units are sensitive to vibration at the difference between the sense and drive frequencies. This sensitivity is only seen in a band of

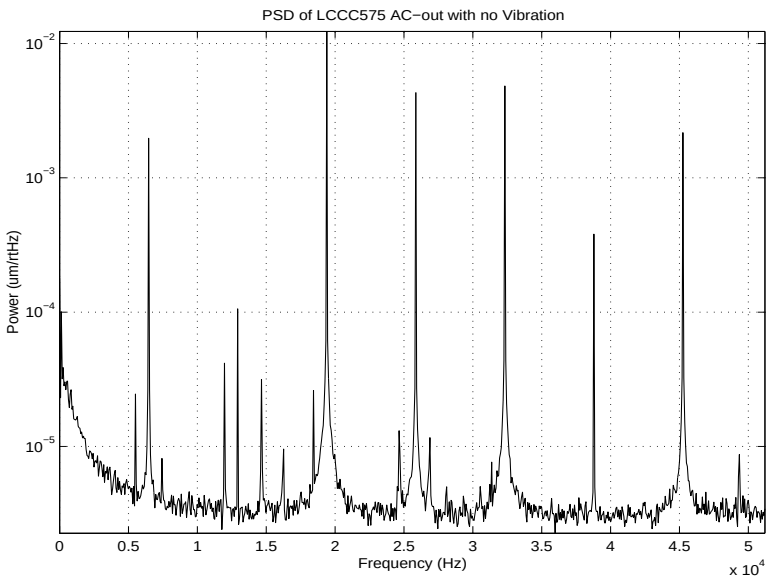

Figure 6-1: PSD of AC-Out for LCCC575 running Closed Loop, with No Vibration

about 2–3 Hz around the difference frequency. Sinusoidal vibration at this frequency causes significant motion of the proof masses in the sense mode, even at fairly low accelerations. Some units were more sensitive than others. As much as $3.6{\cdot}10^{-2}$ μm_{rms} differential motion was seen (LCCC575 with a 6.2 g_{pk-pk} drive).

Figure 6-1 shows a PSD of AC-out for LCCC575 while running with no vibration. Figure 6-2 shows the PSD when the unit is experiencing a 6.2 g_{pk-pk} sinusoidal vibration at the difference between the sense and drive frequencies (1.740 kHz). Note that there is a lot more energy at the sense frequency, 14.932 kHz, during vibration. The total size of the spike is 0.037 μm_{rms}. The PSD units, as noted, are $\mu m/\sqrt{Hz}$, where the voltage read off of AC-out has been multiplied by the appropriate scale factors (see section 2.3.2) to produce a measure of differential motion of the proof masses in μm.

The high sensitivity to vibration at $\omega_{sense} - \omega_{motor}$ was seen on all 4 gyros tested. Table 6.1 summarizes the results for sinusoidal vibration of the four test units at the difference frequency. For each unit, I give the sensitive frequency (which matches perfectly with $f_{sense} - f_{motor}$), the level of vibration delivered during the test, the size

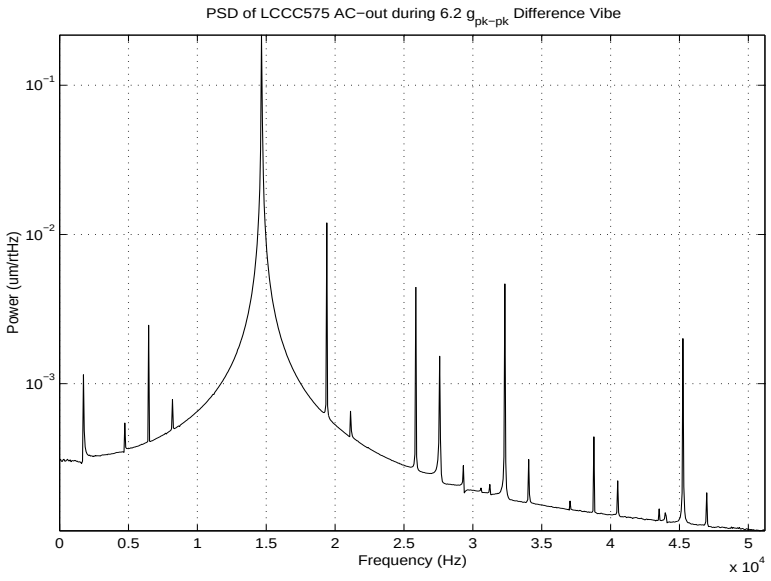

Figure 6-2: PSD of AC-out for LCCC575 during Sinusoidal Vibration at 1742 Hz

of the sense mode spike in AC-out with no vibration, and the sense mode response during vibration.

It seems likely that sinusoidal vibration at the difference frequency is causing an oscillating rotation of the shaker at the vibe frequency. That is, it seems that the entire structure is rocking back and forth at the vibe frequency. This rotation will create a Coriolis acceleration in the frame of the device equal to the product of the angular rate of the structure with respect to inertial space and the velocity of

UNIT	Frequency (Hz)	Level of Vibration (g_{pk-pk})	Power at Sense Frequency in AC-out with no vibe (μm_{rms})	Power at Sense Frequency in AC-out with vibe at diff. (μm_{rms})	Power at Sense Frequency in AC-out during vibe per input g ($\mu m_{rms}/g_{pk-pk}$)
LCCC574	**1965**	**10.0**	**$4.0 \cdot 10^{-5}$**	**$5.90 \cdot 10^{-3}$**	**$5.92 \cdot 10^{-4}$**
LCCC575	**1742**	**3.7**	**$6.0 \cdot 10^{-6}$**	**$3.70 \cdot 10^{-2}$**	**$9.99 \cdot 10^{-3}$**
LCCC576	**1660**	**2.0**	**$1.0 \cdot 10^{-5}$**	**$1.80 \cdot 10^{-2}$**	**$8.97 \cdot 10^{-3}$**
LCCC577	**1858**	**5.0**	**$2.0 \cdot 10^{-5}$**	**$1.60 \cdot 10^{-2}$**	**$3.23 \cdot 10^{-3}$**

Table 6.1: Summary of Sense Mode Response to Vibe at Difference Frequency

the proof mass in the frame(mostly at the drive frequency). See section 2.2.3 for a description of Coriolis effects. Thus, if the vibration is at the difference between drive and sense, the sideband created by the multiplication will be exactly at the sense modal frequency. Due to the large mechanical gain at this frequency, we will create substantial motion in the sense mode, which is the response we are seeing in AC-out. This is the simplest available mechanism for generating substantial excitation at the sense frequency due to a signal at the difference frequency. The hypothesis is supported by the computations of sections 6.2.1 and 6.2.2.

$$
\begin{aligned}
A_{Coriolis}(t) &= m\Omega(t) \times v(t) \\
&\text{where} \\
\Omega(t) &= \Omega_0 \sin((\omega_{sense} - \omega_{tunefork})t) \\
v(t) &= V_0 \sin(\omega_{tunefork} t) \\
&\text{so} \\
A_{Coriolis}(t) &= 2\Omega_0 V_0 (0.5 \cos((\omega_{sense} - \omega_{tunefork} + \omega_{tunefork})t) \cdots \\
&\quad - 0.5 \cos((\omega_{sense} - \omega_{tunefork} - \omega_{tunefork})t)) \qquad (6.1)
\end{aligned}
$$

The Coriolis acceleration from equation 6.1 has a component exactly at the sense resonant frequency,

$$A_{Coriolis}(t) = \Omega_0 V_0 \cos(\omega_{sense} t) \qquad (6.2)$$

The hypothesis that the sense mode is being excited by Coriolis effects is supported by the fact that no response to vibration at the difference frequency is seen during open loop operation. In open loop operation, there is no velocity of the proof masses in the frame and so no Coriolis accelerations develop.

In addition, the accelerometer measuring acceleration in the sense direction (orthogonal to the main acceleration direction) measures acceleration levels as high as 50% of the primary acceleration. If the structure is rocking, substantial transverse

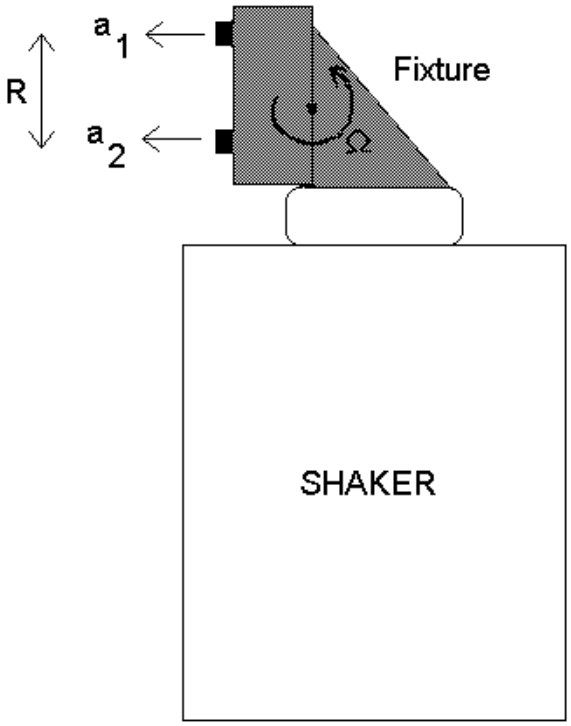

Figure 6-3: Experimental Setup for Determining Rocking of Motor Axis Fixture on Labworks Shaker

accelerations such as this should be seen.

6.2.1 Measurement of Fixture Rocking

To measure the table rocking, sideways accelerations of the fixture were measured at two different points. By assuming that all sideways motion of the table comes from rocking (i.e. the bearings are too stiff to allow substantial sideways translational motion), the magnitude of the rocking motion can be computed. Figure 6-3 shows the setup with the locations of the accelerometers, and defines the various variables. In figure 6-3, these variables are diagrammed:

R = vertical distance between the two accelerometers

a_1 = horizontal acceleration measured by the top accelerometer

a_2 = horizontal acceleration measured by the bottom accelerometer

Ω = angular rotational rate of the structure

R is known, a_1 and a_2 are measured. The two unknowns are the location of the center of rotation and the angular rate. However, if we assume all sideways motion comes from the rotation of the fixture, and that the rotation is sinusoidal at the same frequency as the input, we can compute the angular rotation of the structure and the position of the center.

Although the position of the center of rotation does not affect computations of the rotation levels (only the distance between the accelerometers, R, comes into the expression for Ω), the center of rotation can still be computed. If this model of rigid body rotation is correct, the center should be in the same place for different acceleration levels. Thus, I will compute not only the level of rocking, but also the position of the center of rotation.

In doing this, there is one ambiguity: the center of rotation could be between, above or below the positions of the accelerometers. The center should not be above the accelerometers, as is clear from the distribution of mass. Computations were carried out assuming locations between and below the accelerometers. If we assume the center of rotation is between the two, we get better agreement for tests at different frequencies. Also, there is one test where there is no solution for the center of rotation below the accelerometers. Thus, concluding that the center of rotation is somewhere between the two accelerometers, equation 6.3 below gives the solution:

$$\begin{aligned} \Omega &= \frac{a_1 + a_2}{R\omega} \\ R_1 &= \frac{a_1}{\Omega\omega} \\ R_2 &= \frac{a_2}{\Omega\omega} \end{aligned} \tag{6.3}$$

Where:

ω = frequency of the input to the shaker

Vibe Frequency (kHz)	Vibe Level ($g_{pk\text{-}pk}$)	a_1 ($g_{pk\text{-}pk}$)	a_2($g_{pk\text{-}pk}$)	Ω ($(rad/sec)_{pk\text{-}pk}$)	R_1 (cm)
1.97	**9.99**	**3.31**	**3.31**	**0.239**	**1.10**
1.74	**3.69**	**1.44**	**0.700**	**0.0871**	**1.50**
1.66	**2.01**	**0.781**	**0.379**	**0.0495**	**1.50**
1.86	**5.00**	**1.86**	**1.35**	**0.122**	**1.30**

Table 6.2: Data and Computation of Table Rocking for Various Conditions

R_1 and R_2 are the vertical distance from accelerometer 1 and accelerometer 2 (respectively) to the center of rotation

Four gyros were tested with vibration at their difference frequency, as described in section 6.2. For each of the four test situations, the accelerations a_1 and a_2 were recorded. Since there was often distortion in the sideways acceleration signal, acceleration at the input vibration frequency was determined by integrating the spike in the PSD. Using equation 6.3, the rotation and position of the center of rotation has been computed for each case. Table 6.2 describes the results.

$$R = 2.2cm$$

Note that to a very good degree of accuracy, the rotation of the table, Ω, is linearly related to the magnitude of the input vibration, regardless of frequency. The linear fit is shown in figure 6-4, giving rotation of 0.024 (rad/s)/g. Also, note that the position for the center of rotation from run to run is fairly constant, which makes sense. Both of these facts strongly support the idea that all of the sideways acceleration is, indeed, coming from rotation of the fixture. A comparison of the level of fixture rocking computed from this method with the level needed to excite the observed gyro sense mode motion is given in section 6.2.2.

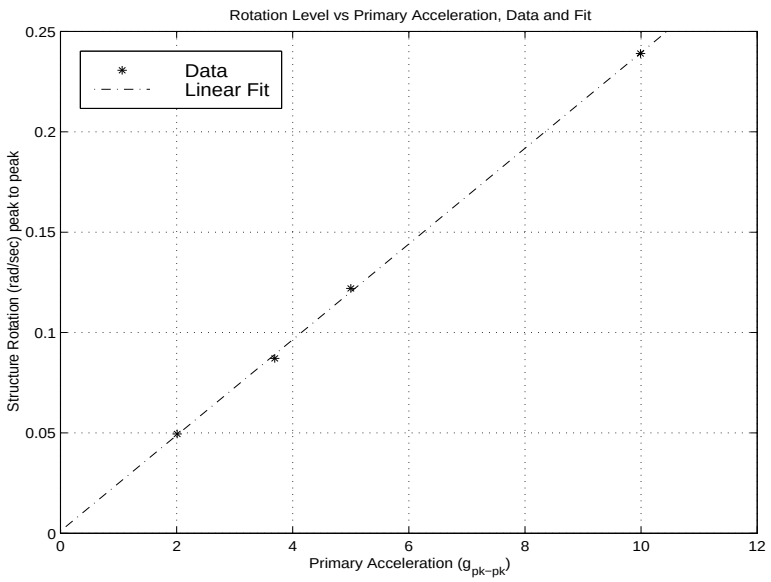

Figure 6-4: Computed Fixture Rotation vs. Primary Acceleration

6.2.2 Expected Sense Mode Response due to Rocking

With this estimate of the fixture angular vibration, we can compute the expected response of the sense mode due to Coriolis forcing. Assuming matched masses and springs, we can derive the transfer function relating the Coriolis acceleration input to the differential motion of the two proof masses out of the plane. (recall that this differential motion is what we see on AC-out). From the full linear model of equation 2.16, the transfer function given in equation 6.4 is derived,

$$\frac{Y_\Delta}{A_{Coriolis}} = \frac{2m}{ms^2 + b_y s + \frac{k_y k_\theta}{k_\theta + 2k_y L^2}} \tag{6.4}$$

A plot of the frequency response from Coriolis acceleration to differential sense motion is given in figure 6-5. A Coriolis acceleration delivered at the sense resonance produces a 9.40 dB gain, that is, 2.95 $\mu m/(m/s^2)$ of differential motion, using the parameter values for LCCC575. This magnitude will vary slightly from unit to unit depending on damping.

Equation 6.5 gives the magnitude of Coriolis acceleration produced at the sense

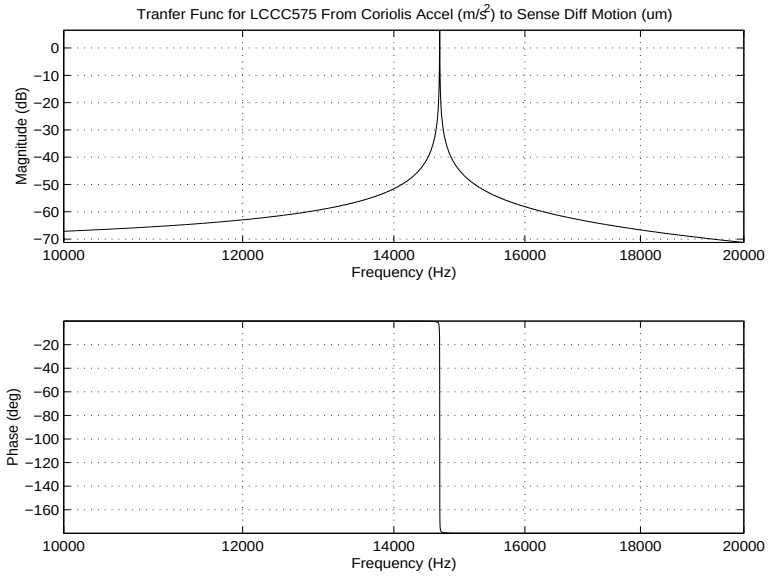

Figure 6-5: Transfer Function relating Sense Differential Motion to Coriolis Acceleration

frequency. From table 6.2, the rotation of the table is 0.024 (rad/s)/g, and during closed loop operation the motor displacement amplitude is 10 μm, giving a velocity amplitude of

$$V_0 = X_0 \omega_{tunefork} = (10\mu m)(12.450kHz) \cdot (2\pi) = 0.78 \;\; m/s$$

The mass of the proof mass, m, is $3.6 \cdot 10^{-8}$ kg. From this we can compute the expected motion of the sense mode due to Coriolis accelerations generated by fixture rocking. The predicted results are compared with measured results in table 6.3. Equation 6.5 gives the magnitude of the component of Coriolis acceleration at the sense frequency.

$$A_{Coriolis}(t) = \Omega_0 V_0 \cos(\omega_{sense} t) \tag{6.5}$$

In all cases, the measured response was lower than the predicted. However, the predictions assume that the Coriolis acceleration is being delivered precisely at peak

Unit	Primary Acceleration (g_{pk})	Rocking Motion ($(rad/sec)_{pk}$)	Produces Coriolis Acceleration $(m/s^2)_{pk}$	Predicted Sense Motion (μm_{pk})	Observed Sense Motion (μm_{pk})	Necessary Frequency Deviation to Produce Error
LCCC574	**5.00**	**0.120**	**0.0939**	**0.254**	**0.00834**	**0.14%**
LCCC575	**1.86**	**0.0443**	**0.0347**	**0.102**	**0.0523**	**0.0067%**
LCCC576	**1.00**	**0.0240**	**0.0189**	**0.0574**	**0.0255**	**0.0079%**
LCCC577	**2.51**	**0.05.99**	**0.0467**	**0.215**	**0.0226**	**0.024%**

Table 6.3: Comparison of Predicted and Measured Sense Mode Response Assuming Coriolis Drive from Rocking

resonance. Since the Q of the gyro is so high, the resonant peak is very narrow, and any small deviation from the exact resonant frequency vastly reduces the response.

The last column of table 6.3 gives the percentage deviation from the sense frequency needed to produce the measured response. The frequency deviations required range from 1 Hz for LCCC575 and LCCC576, to 18 Hz for LCCC574. These are well within the resolution of the frequency generator; vibrations were within 1 Hz at worst of the true resonance. The errors may come from the inaccurate measurements of table rocking taken from accelerometer readings. More work should be done to determine whether all of the observed sense motion is truly coming from table rocking. However, it does seem plausible that a substantial part of the response is generated by Coriolis effects.

6.2.3 Rate-out Due to Vibe at Difference Frequency

Excitation of the sense mode has an effect on rate-out measurements. Vibration at the difference frequency creates two new components of rate-out: one component at the vibe frequency, and a smaller one at the sense frequency. A PSD of rate out with no vibration for LCCC575 is shown in figure 6-6. Figure 6-7 shows the PSD during the 3.7 g_{pk-pk} vibe at the difference frequency (1.742 kHz).

To determine whether the 0.16 $(deg/s)_{rms}$ spike seen in rate-out at the difference between sense and tuning fork in figure 6-7 comes from real motion of the sense axis, we must compute the expected motion of the sense axis due to rocking. From this, we can compute the expected output on rate-out.

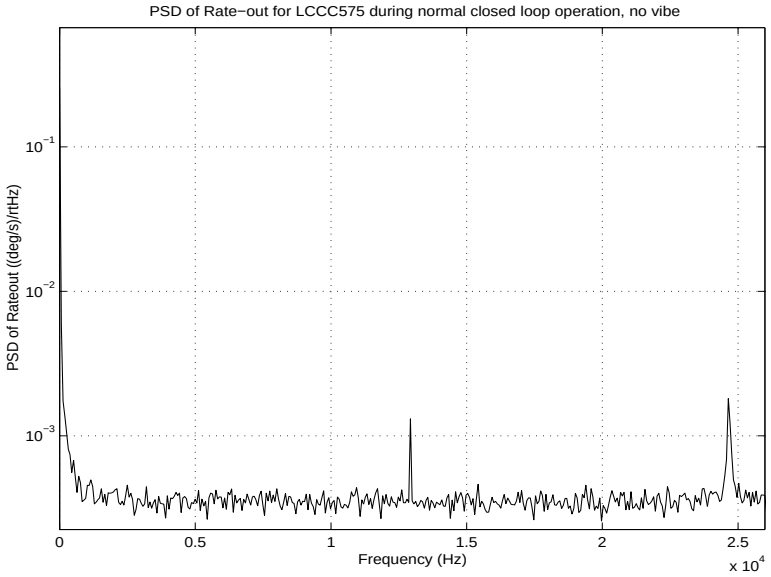

Figure 6-6: PSD of Rate-out for LCCC575 with no Vibe

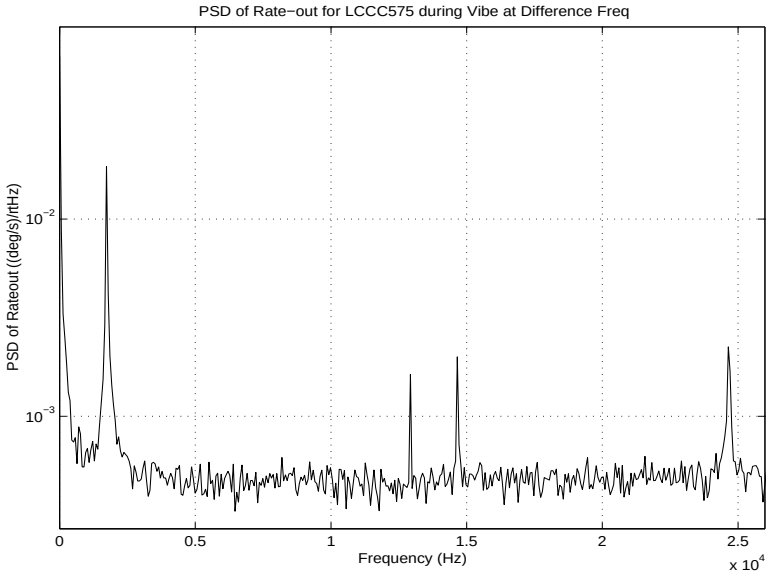

Figure 6-7: PSD of Rate-out for LCCC575 with 3.7 g_{pk-pk} Vibe at Difference Frequency

A 3.7 g_{pk-pk} vibration, such as that experienced by LCCC575 during the test, corresponds to $\Omega_0 = 0.089 rad/s$ of rotation.

$$\Omega_0 = (0.024(rad/s)/g)(3.7 g_{pk-pk}) = 0.089(rad/s)_{pk-pk}$$

This produces a Coriolis acceleration with magnitude of $6.94 \cdot 10^{-2}$ $(m/s^2)_{pk-pk}$ according to equation 6.5.

$$A_{Coriolis}(t) = \Omega_0 V_0 \cos(\omega_{sense} t) = (0.089 rad/s)(0.78 m/s) = 6.94 \cdot 10^{-2} (m/s^2)_{pk-pk}$$

For LCCC575, we saw that the gain at resonance for the sense mode is 2.95 μm_{pk-pk} of differential motion for 1 $(m/s^2)_{pk-pk}$ applied Coriolis acceleration. Thus, the vibration creates 0.2 μm_{pk-pk} of differential sense motion at the sense resonant frequency.

At low frequencies, the transfer function gives a gain of $2.34 \cdot 10^{-4}$ μm of differential sense motion per (m/s^2) applied Coriolis acceleration. A rotation of 1 deg/s produces a Coriolis acceleration of magnitude $3 \cdot 10^{-2}$ $(m/s^2)_{pk}$ resulting in $3.2 \cdot 10^{-6}$ μm_{pk} of sense motion.

$$X_0 = (1(deg/s)_{pk})(\pi/180\ rad/deg)(0.78 m/s) \times (2.34 \cdot 10^{-4} \mu m/(m/s^2)) = 3.2 \cdot 10^{-6} \mu m_{pk}$$

Now, the difference frequency for LCCC575 is 1.742 kHz, which is 17.4 times the gyro bandwidth of 100 Hz, or 1.74 decades. Thus, since the low-pass demodulator filter is a four pole filter, we expect an attenuation of -111 dB between the output generated by a low frequency rotation and that generated by rotation at the difference frequency, as shown in figure 6-8. The low frequency scale factor for LCCC575 is

$$13.9 mV/(deg/s) = 13.9 mV/3.2 \cdot 10^{-6} \mu m_{pk} = 4340 V/\mu m_{pk}$$

so the scale factor at 1.742 kHz should be

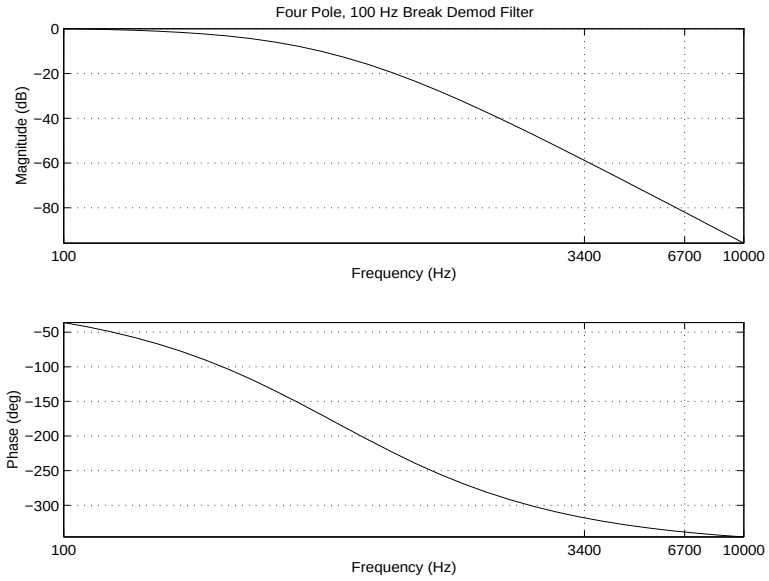

Figure 6-8: Four Pole Low Pass Filter on Sense Demod

$$(4340V/\mu m_{pk}) \times (-111dB) = 12.2mV/\mu m_{pk}$$

Above we computed that the Coriolis forces were exciting 0.2 μm_{pk-pk} of sense mode motion during vibration. From above, this should result in 1.2 mV_{pk} at rate-out. The actual spike in rate-out measured from the PSD in figure 6-7 is 3.2 mV_{pk}.

Given the approximations made in the ideal four pole filter and the magnitude of both rocking and transfer function gain at resonance, this constitutes good agreement. It is reasonable to conclude that the erroneous signal in rate out is coming from normal functioning of the sense chain demodulator operating on sense mode response to rocking.

$$0.1\mu m_{pk} \times 5.6\ mV/\mu m_{pk} \times (1/13.9)\ (deg/s)/mV\ = 0.043deg/s$$

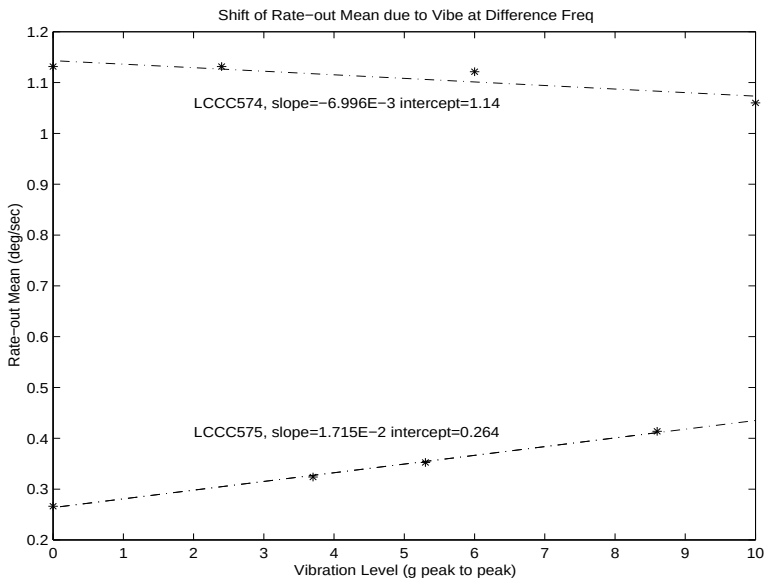

Figure 6-9: Rate-out Mean for LCCC574 and LCCC575 During Difference Frequency Sinusoidal Vibe

6.2.4 Shifts in the Mean of Rate-out

Sinusoidal vibration at the difference frequency has very little effect on the mean of rate out. Rate out mean will only change if the energy at the tuning-fork frequency in AC-out changes. There is no particular reason why vibration at the difference frequency should strongly influence the tuning-fork amplitude, although substantial sense motion could cause some changes due to cross-axis coupling in the mechanical model. However, cross-axis coupling effects are small, and so there should be very little shift in the mean of rate-out. Figure 6-9 shows how rate-out mean changes with the amplitude of vibration at the difference frequency for two units.

The rate-out mean trends fairly linearly with applied vibration at the difference, but does not shift very much even with the relatively large sinusoidal vibrations applied.

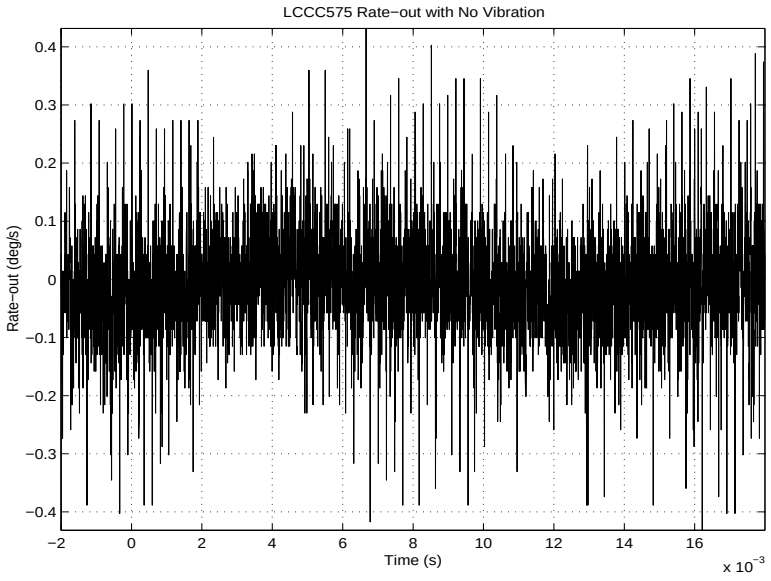

Figure 6-10: Rate-out for LCCC575 with No Vibration

6.3 Low Frequency Random Vibration

Random vibration in the 0-6 kHz low frequency band causes significant output on rate-out. However, it is likely that much of the low frequency rate measured during low frequency random vibration is caused by real rotation of the test structure. Erroneous rate measurements are seen at the difference between drive and hula.

6.3.1 Examples of Time Domain Rate-out Signal

Figure 6-10 shows rate-out for LCCC575 with no vibration. Figure 6-11 shows rate-out with random vibration in a 0-6.4 kHz band at 1.25 g_{rms}.

Similar results are obtained for LCCC574, showing a tenfold increase in the mean square value of rate-out with a 1.25 g_{rms} vibration in the 0-6.4 kHz band. Most of this is due to low frequency components which are almost certainly real rotation of the structure. (see section 6.3.3)

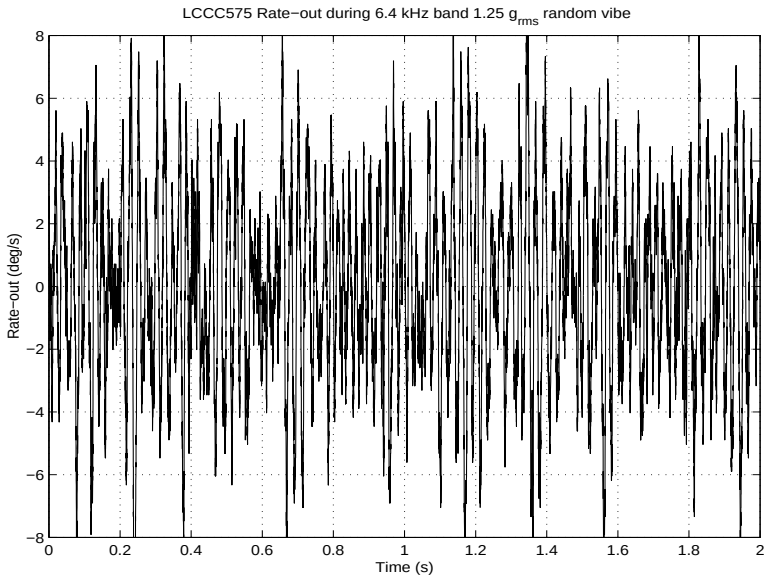

Figure 6-11: Rate-out for LCCC575 during 6.4 kHz band, 1.25 g_{rms} random vibration

6.3.2 Major Frequency Components of Rate-out

There are a few major frequency components seen in the PSD of the rate-out signal during random vibration. Figure 6-12 is a PSD of rate-out during random vibration for LCCC575.

The major frequency components, and the power at each (integral of the spike with respect to frequency), are listed below (taken from PSDs such as that in figure 6-12):

LCCC574, during 1.4 g_{rms} 0-6.4 kHz band random vibe

870 Hz +/- 10 Hz, 0.401 $(deg/s)_{rms}$

190 Hz +/- 10 Hz, 1.94 $(deg/s)_{rms}$

40 Hz +/- 10 Hz, 8.66 $(deg/s)_{rms}$

LCCC575, during 1.25 g_{rms} 0-6.4 kHz band random vibe

1740 Hz +/- 20 Hz, 0.020 $(deg/s)_{rms}$

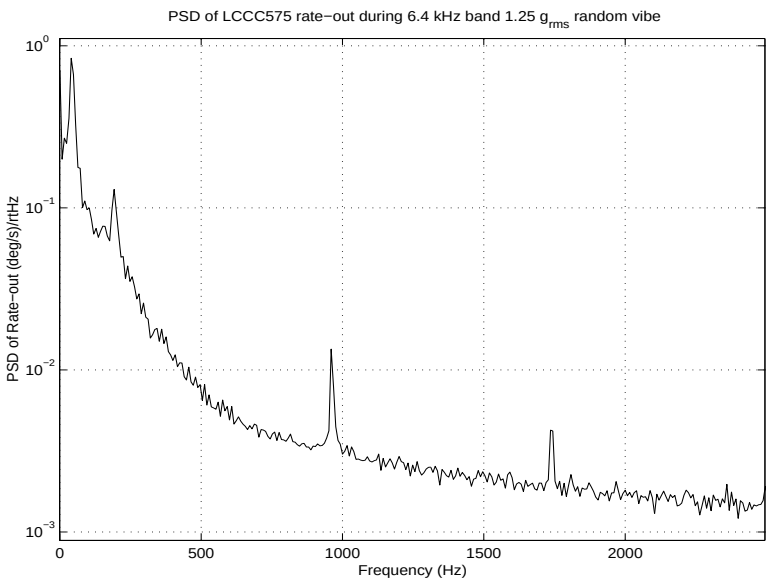

Figure 6-12: PSD of Rate-out for LCCC575 during 6.4 kHz band, 1.25 g_{rms} random vibration

960 Hz +/- 10 Hz, 0.050 $(deg/s)_{rms}$

190 Hz +/- 10 Hz, 0.72 $(deg/s)_{rms}$

40 Hz +/- 10 Hz, 3.49 $(deg/s)_{rms}$

6.3.3 Components due to Real Rotation of Test Structure

The 190 Hz and 40 Hz components are common to both units. This suggests that they come from the environment (which is common to both units) rather than from the units themselves. Indeed, they seem to come from motion (probably rotation) of the test structure at those frequencies (i.e. there is a spike in the accelerometer outputs at those frequencies indicating large structure motion). Figure 6-13 shows a PSD of the sense axis accelerometer signal, which should give an indication of the magnitude of structure rotation.

In figure 6-13, we clearly see the 190 Hz and 40 Hz spikes, indicative of rotation of the structure (most sideways motion of the structure should be due to rotation

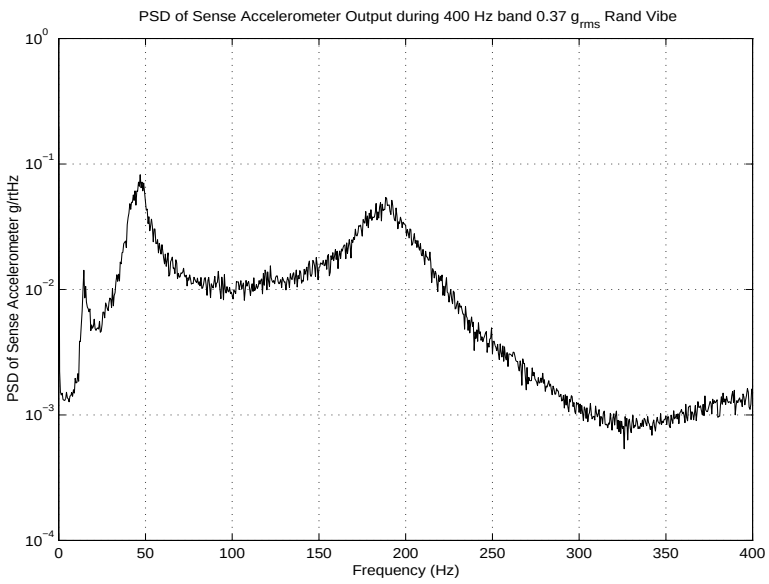

Figure 6-13: PSD of Sense Accelerometer during 400 Hz band, 0.37 g_{rms} random vibration

since the shaker is more compliant to rotation than sideways translation). Thus, we can conclude that these two spikes come from real rotation of the test structure, and should therefore appear in rate-out.

6.3.4 Rate-out Components due to Other Gyro Modes

The 870 Hz and 960 Hz signals seen in the rate-out spectrum for LCCC574 and LCCC575 are exactly at the difference between motor and hula frequencies. This occurs because the small amount of vibration energy at the hula frequency is enough to excite the high-Q hula mode. Motion at hula gets coupled into AC-out due to charge injection effects, as described in section 2.4.1. Equation 6.6 repeats the equation relating hula motion to AC-out given in section 2.4.1.

$$V_{out} = \frac{1}{C_{fb}} \left(\frac{V_{lbias} C_{iml}}{x_0} x_1 + \frac{V_{rbias} C_{imr}}{x_0} x_2 \right) \tag{6.6}$$

Where

V_{rbias} = DC bias on the right inner motor = +5 V

V_{lbias} = DC bias on the left inner motor = -5 V

C_{fb} = sense preamp feedback capacitor $\approx$ 2.2 pF

C_{iml} = zero displacement left inner motor capacitance $\approx$ 0.45 pF

C_{imr} = zero displacement right inner motor capacitance $\approx$ 0.45 pF

x_0 = nominal motor comb overlap $\approx$ 25 μm

x_1 = displacement of the left proof mass in the plane with respect to the substrate

x_2 = displacement of the right proof mass in the plane with respect to the substrate

During hula motion, x_1 and x_2 are opposite one another in phase, so their effects sum. Thus, hula motion creates a signal on AC-out with scale factor 80 mV/μm of hula amplitude.

When the hula frequency gets demodulated by the velocity clock, we get a signal on rate-out at the difference between hula and drive, which is low enough frequency not to be completely attenuated by the low pass filter.

There is a substantial spike at the hula frequency, for both units, in both AC-out and the position signal. This spike is not evident when no vibration is being delivered.

The 1740 Hz spike for LCCC575 is the difference between the sense and drive frequencies. This is caused by motion of the sense axis in the sense mode driven by the random vibration. Again, the difference frequency appears at rate-out due to the demodulation with the motor velocity clock. LCCC574 is not as sensitive to vibration driving the sense mode, as demonstrated in table 5.1 of section 5.3. Thus, it does not exhibit an erroneous rate-out signal at $\omega_{sense} - \omega_{tunefork}$.

Chapter 7

High Frequency Closed Loop Vibration Testing

Since the four lightly damped gyro modes lie in the high frequency band between 10 kHz and 20 kHz, the gyro is very sensitive to high frequency vibration. Section 5 describes the open loop mechanical response of the various modes to both sinusoidal vibration and random vibration in the gyro modal band. This chapter explores the effects of high frequency vibration on the closed loop operation of the gyro.

The effects of high frequency vibration on rate-out measurements are discussed. Changes in rate-out mean, as well as frequency components appearing on rate-out, will be examined. The maximum sustainable vibration levels which will not clip AC-out (that is, saturate the electronics due to a high AC-out signal) will be considered. Also, measurements of vibration levels that cause the motor loop to lose lock are presented. In all the tests discussed here, the gyro was mounted in the Wilcoxon piezoelectric shaker, running closed loop using the EDM3 electronics.

7.1 Summary

There are a few essential conclusions drawn from the results outlined in this chapter:

- Random vibration in the band containing all four gyro modes excites every

mode, but due to sensing schemes and mechanical gains the sense and hula frequencies are predominant on AC-out.

- Random vibration creates an erroneous rate-out component at the difference between hula and tuning fork, on the order of 1 deg/s for a 0.5 g_{rms} 11-19 kHz random vibe.

- Random vibration levels of approximately 0.025 $g/\sqrt{Hz}$ in the 11-19 kHz band excite enough hula and sense motion to begin clipping AC-out.

- Random vibration levels of more than 0.005 $g/\sqrt{Hz}$ will shift the mean of rate-out by as much as 2 deg/s, and cause it to become very unstable.

- The gyro is most sensitive to sinusoidal vibration at the hula frequency. Vibration levels of 0.015 g_{pk-pk} at hula will begin to clip AC-out.

  - Vibration at hula of 0.015 g_{pk-pk} or more has a major effect on the mean of rate-out, causing shifts of up to 17 deg/s.

- Vibration at hula of approximately 7 g_{pk-pk} causes the motor loop to lose lock, and gyro operation ceases. This level of vibration is the level needed to produce a hula mode amplitude of 10 μm, the nominal tuning-fork amplitude.

- Vibration near the tuning fork frequency creates a low frequency signal on rate-out at the difference between the applied vibration and tuning-fork frequencies. This is probably due to angular vibration, and occurs at levels as low as $0.003 rad/s$.

7.2 High Frequency Random Vibration

Random vibration delivered in the 11-19 kHz band (which includes all four major gyro modes) has a substantial effect on rate out and can quickly rail AC-out. Figure 7-1 gives a PSD of a typical acceleration input spectrum. Most of the acceleration signal appears in the 11-19 kHz band. The noise is not white, due to fixture dynamics. When

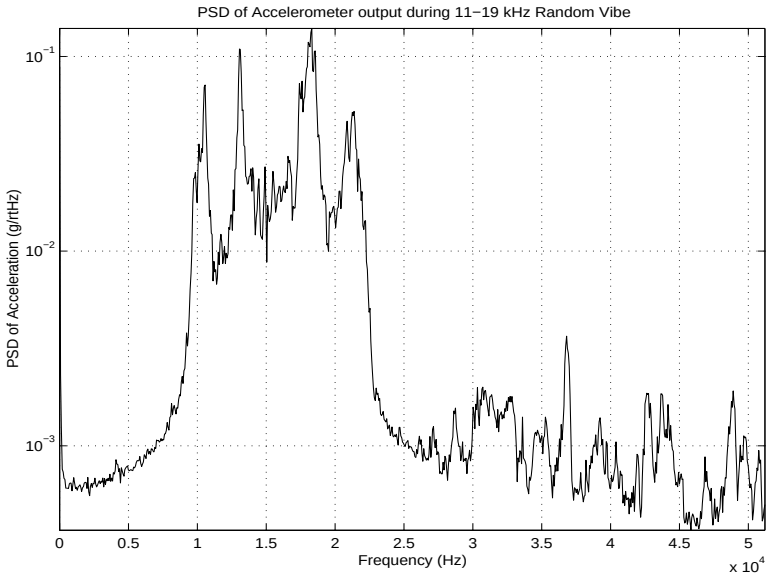

Figure 7-1: PSD of Accelerometer Output for High Frequency Random Vibration in 11-19 kHz band

determining response of a particular mode to random vibration, the PSD vibration level is measured near the modal frequency in question. Figure 7-2 gives a narrow band PSD of the same data.

All four main gyro modes are excited by random vibration, exactly as described for open loop operation in chapter 5. Hula and Out-of-Plane are excited most strongly. All of the modal frequencies can be seen on AC-out, although Out-of-Plane is attenuated due to common mode rejection in the sense biasing scheme. Demodulation with the velocity clock produces sidebands at the difference between each modal frequency and the tuning fork frequency. Since the hula frequency is closer to tuning-fork, it is attenuated less by the rate-out demod filter, and is strongly evident on rate-out. Figure 7-3 shows a PSD of rate-out for LCCC574 undergoing a 0.53 g_{rms} 11-19 kHz random vibration. The large component in rate out at $f_{tunefork} - f_{hula}$ integrates to 0.74 deg/sec.

For both LCCC574 and LCCC575 rate-out contains a substantial component at the difference between hula and tuning fork. In addition to errors in rate out, AC-out

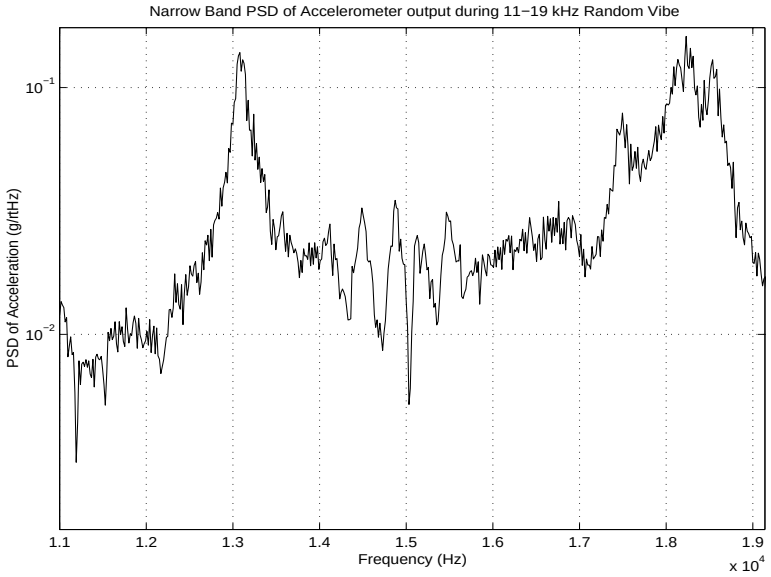

Figure 7-2: Narrow Band PSD of Accelerometer Output for High Frequency Random Vibration in 11-19 kHz band

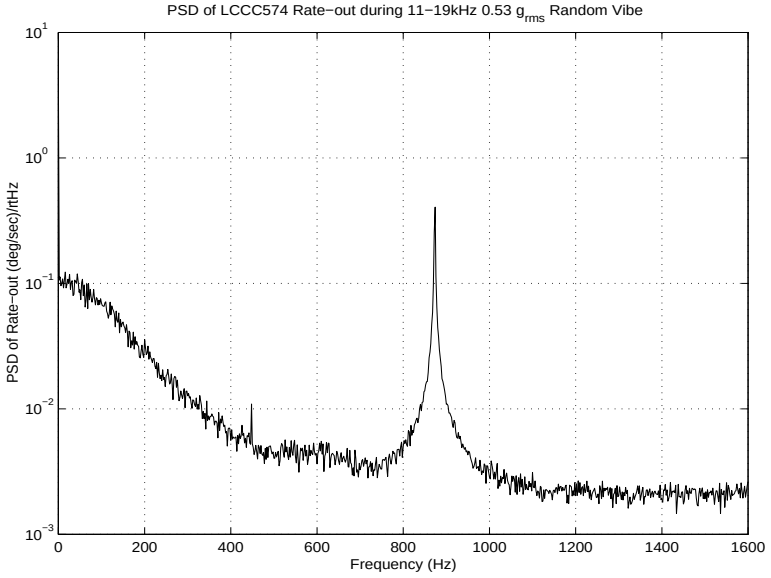

Figure 7-3: PSD of LCCC574 Rate-out During 11-19 kHz Random Vibe, 0.53 g_{rms}

Unit	Hula Mode (μm/(g/√Hz))	Tuning Fork Mode (μm/(g/√Hz))	Sense Mode (μm/(g/√Hz))	Out-of-Plane Mode (μm/(g/√Hz))
LCCC561, predicted	**82.99**	**3.47**	**0.68**	**14.69**
LCCC561, measured	**56.39**	**2.65**	**0.75**	**2.86**
LCCC574, predicted	**99.93**	**2.52**	**0.48**	**17.01**
LCCC574, measured	**234.49**	**2.52**	**2.04**	**10.48**
LCCC575, predicted	**106.05**	**0.14**	**0.88**	**18.03**
LCCC575, measured	**195.38**	**0.27**	**7.82**	**21.56**

Table 7.1: Summary of Steady State Open Loop Random Vibration

can be clipped. Table 7.1, taken from section 5.4, gives the open-loop response of each mode to white noise of a particular level. Sense mode differential motion of 0.1 μm (corresponding to 0.05 μm of each side) will cause AC-out to clip. (see section 2.4.1. For LCCC574, 2 $\mu m/\left(g/\sqrt{Hz}\right)$ was measured for one side, so, to avoid clipping, we must keep acceleration levels below 0.025 $g/\sqrt{Hz}$. This corresponds to 2.2 g_{rms} in the 11-19 kHz band. A random vibration test conducted at 4 g_{rms}, 11-19 kHz for LCCC574 does clip AC-out due to excitation of the sense and hula modes.

These are the two major effects of high frequency random vibration on closed loop performance. AC-out will clip with vibrations on the order of 0.025 $g/\sqrt{Hz}$, and an erroneous signal will appear on rate-out at $f_{tunefork} - f_{hula}$. The fixture rotation effects seen during low frequency random vibration are not evident, probably because the fixture modes are all below the 11-19 kHz band in which high frequency vibration was delivered.

Random vibration has a large effect on the mean of rate-out, causing substantial changes and a very unstable signal. Table 7.2 shows the change in rate-out mean for LCCC574 and LCCC575 during random vibration in the 11-17.4 kHz band.

Unit	Vibe Level	Mean of Rate Out (deg/sec)
LCCC574	**No Vibration**	**2.04**
LCCC574	**5E-3 g/rtHz = 0.4 g_{rms} in 6.4 kHz Band**	**-0.1, unstable**
LCCC574	**4E-2 g/rtHz = 3.16 g_{rms} in 6.4 kHz Band**	**-11 +/- 3, unstable**
LCCC575	**No Vibration**	**0.36**
LCCC575	**5E-3 g/rtHz = 0.4 g_{rms} in 6.4 kHz Band**	**0.33**
LCCC575	**4E-2 g/rtHz = 3.16 g_{rms} in 6.4 kHz Band**	***moving*: 25 second averages gave -0.58, 4.32, -1.79, -1.73, -2.01, 0.0, 3.17**

Table 7.2: Data Showing Change in Rate-out Mean During 11-17.4 kHz Random Vibration

7.3 Sinusoidal Vibration

Sinusoidal vibration at the gyro resonant frequencies caused shifts in rate-out and could cause the gyro to lose lock on the tuning-fork mode and shut down completely. The gyros were most sensitive to vibration at the hula frequency. Refer to section 5.3 for predictions and data showing the response of the various gyro modes to sinusoidal vibration at the natural frequencies. The sense and tuning fork modes are antiparallel, and thus not easily excited by vibration. The sense biasing scheme rejects the out-of-plane mode. Thus, during closed loop vibration the gyro is most sensitive to vibration of the hula mode.

7.3.1 Clipping of AC-out

Hula motion couples directly onto rate out due to charge injection effects. Since the two inner motor points are at $\pm$ 5 V, the charge injection cancels due to tuning fork motion, but adds during hula motion. The magnitude of the resulting signal on AC-out can be computed from equations 7.1 and 7.2. See sections 2.3.2 and 2.4.1 for an explanation of hula charge injection.

$$V_{out}(t) = \frac{1}{C_{sfb}} \int_0^t \frac{C_{im}}{x_0} \left(-5V \cdot \dot{x}_1(t) - 5V \cdot \dot{x}_2(t)\right)\ dt \tag{7.1}$$

Where:

V_{out} = sense preamp output

C_{sfb} = sense feedback capacitor

C_{im} = nominal inner motor capacitance (no motion)

x_0 = nominal comb overlap (no motion)

$x_1(t)$ = displacement of left proof mass relative to substrate

$x_2(t)$ = displacement of right proof mass relative to substrate

For the hula mode with x_1 and x_2 exactly in phase with each other, and oscillating at the hula frequency, this becomes

$$x_1(t) = X_1 \sin(\omega_{hula} t) x_2(t) = X_2 \sin(\omega_{hula} t)$$

$$V_{out} = \frac{C_{im}}{C_{sfb} x_0} \cdot (-5V(X_1 + X_2)) \sin(\omega t) \tag{7.2}$$

If we assume matched sides (i.e. for hula motion $X_1 = X_2$), then, taking the capacitor values for LCCC574 and LCCC575,

- LCCC574 has 82.4 mV/μm voltage at sense preamp output due to hula motion of some amplitude (amplitude of one side).
- LCCC575 has 80.4 mV/μm voltage at sense preamp output due to hula motion of some amplitude (amplitude of one side).

Since AC-out is gained up by a factor of 50 from sense preamp out, and clips at a voltage of 15 V, this means that hula amplitude of approximately 3.5-4.0 μm will clip AC-out. From the computations and measurements of section 5.3, summarized in table 7.3, this corresponds to a hula frequency vibration of 0.005 g for LCCC574, and 0.008 g for LCCC575. Recall that the values shown in table 7.3 are for vibration at the nonlinear resonance. Maintaining vibration at the nonlinear resonance requires a slow downward frequency sweep, creating enough amplitude to shift the frequency

Unit	Hula Mode (μm/g)	Tuning Fork Mode (μm/g)	Sense Mode (μm/g)	Out-of-Plane Mode (μm/g)	Deduced Flexure Spring Mismatch
LCCC561, predicted	**214**	**2%: 9.21**		**9.87**	
LCCC561, measured	**63**			**0.63**	
LCCC574, predicted	**300**	**1%: 8.62** **2%: 16.5**	**1%: 0.41** **2%: 0.84**	**12.03**	
LCCC574, measured	**826**	**7.54**	**0.30**	**4.36**	**motor: ~0.9%** **sense: ~0.72%**
LCCC575, predicted	**331**	**1%: 8.85** **2%: 16.87**	**1%: 0.35** **2%: 0.72**	**14.00**	
LCCC575, measured	**501**	**0.44**	**0.69**	**10.83**	**motor: ~0.05%** **sense: ~1.95%**

Table 7.3: Summary of Steady State Open Loop Sinusoidal Vibration

due to spring softening before moving down to a lower frequency excitation. (see sections 2.2.5 and 2.2.5)

During high frequency vibration testing, vibration was delivered directly at the closed loop resonant frequencies, no downward sweep was conducted. Thus, due to nonlinearities, less motion will be created than the measured results from table 7.3 indicate. If, instead of the measured nonlinear response, we use the linear values predicted by the model (given in the "predicted" rows of the table), we find that AC-out should clip due to hula charge injection at approximately 0.014 g_{pk}. Testing of LCCC574 indicates that AC-out clips at 0.015 g_{pk} due to hula vibration. LCCC575 also clips AC-out at approximately 0.015 g_{pk}. Thus, we seem to be operating at the linear resonance.

Hula vibration delivered at the linear resonant frequency creates hula motion of 3.5-4 μm, enough to begin clipping AC-out, at vibration levels of 0.015 g_{pk}. This agrees with the level of vibration predicted by the linear model, and corresponds to the experimentally determined vibration level needed to clip AC-out.

Unit and Mode	Frequency of Vibe (kHz)	Number of Vibe Levels Tested	Highest Acceleration Tested (g_{pk-pk})	Maximum Deviation of Rate out Mean from Nominal (deg/s)	Comments
LCCC574, Hula	**Motor Vibe 11.580**	**14**	**0.984**	**17.3**	**Most sensitive, see figure**
LCCC574, TuneFork	**Motor Vibe 12.454**	**2**	**0.37**	**0.3**	**Mean fairly insensitive, but much beating**
LCCC574, Sense	**Sense Vibe 14.419**	**6**	**1.66**	**0.03**	**Mean insensitive, AC-out clips at ~1.6 g_{pk-pk}**
LCCC574, OOP	**Sense Vibe 15.893**	**Many**	**0.1**	**<0.05**	**No response seen**
LCCC575, Hula	**Motor Vibe 11.964**	**19**	**0.064**	**14.2**	**Most Sensitive, see figure**
LCCC575, TuneFork	**Motor Vibe 12.930**	**2**	**1.27**	**0.18**	**Mean fairly insensitive, but much beating**
LCCC575, Sense	**Sense Vibe 14.670**	**6**	**4.13**	**0.22**	**Sudden jump in mean at ~1.4 g_{pk-pk}**
LCCC575, OOP	**Sense Vibe 16.240**	**5**	**0.54**	**1.1**	**Sudden jump in mean at ~0.45 g_{pk-pk}**

Table 7.4: Summary of Test Results, Closed Loop Resonant Sinusoidal Vibe

7.3.2 Shift of Rate Out Mean

Vibration at any of the resonant frequencies causes shifts in the mean of rate out. However, as before, the gyro is most sensitive to hula vibration. Table 7.4 summarizes the test results for LCCC574 and LCCC575.

The summary in table 7.4 shows that the gyro is most sensitive to vibration at the hula frequency. All other modes cause only small changes in rate-out mean, even at large accelerations. There is still the danger of damaging the gyro by overdriving a mode and causing contact in the combs or snapdown of the sense axis. The results of section 5 give the maximum safe levels of vibration to avoid such problems.

In both the out-of-plane and sense mode tests for LCCC575, there is a sudden jump in rate-out mean at a particular vibration level. This could perhaps be due to clipping of the AC-out signal at this vibration level. This is particularly likely for the sense mode, since data for LCCC574 indicates that AC-out clips at the vibration level where the rate-out mean jumps.

Vibration at hula causes a large change in the mean of rate out. During hula vibration, substantial hula signal appears on AC-out due to charge injection as described

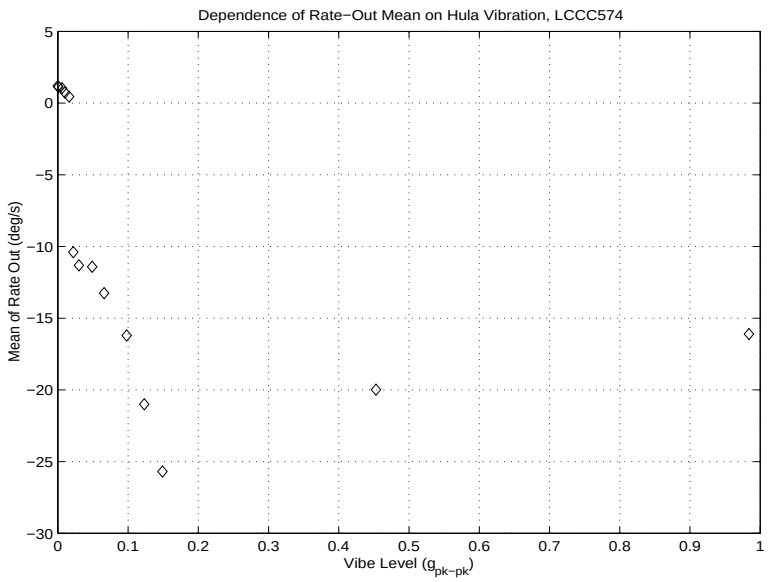

Figure 7-4: Dependence of Rate Mean on Hula Vibration, LCCC574

above. AC-out begins to clip at hula amplitudes of about 3-4 μm, corresponding to vibration levels at hula resonance of approximately 0.015 g_{pk}. (see section 2.4.1) However, the mean of rate out changes over the entire range of vibration levels delivered. The errors produced are substantial, sometimes more than 14 deg/s. Figures 7-4 and 7-5 show the change in rate out mean during hula vibration of LCCC574 and LCCC575. Note that there is a threshold level, approximately the acceleration level at which AC-out starts to clip, below which little change is seen. However, about this level the rate out mean changes substantially.

7.3.3 Vibration at Tuning Fork Frequency

Vibration at the tuning fork frequency creates a low frequency sinusoid on rate out at the difference between the vibration frequency and true tuning fork natural frequency. This occurs because motor axis motion is excited at the vibration frequency, which is close enough to tuning fork to have substantial gain. Due to capacitive mismatch or other amplitude mismatch, this signal appears in AC-out. It is demodulated with the tuning fork frequency, and low pass filtered with the 100 Hz demod filter. Since

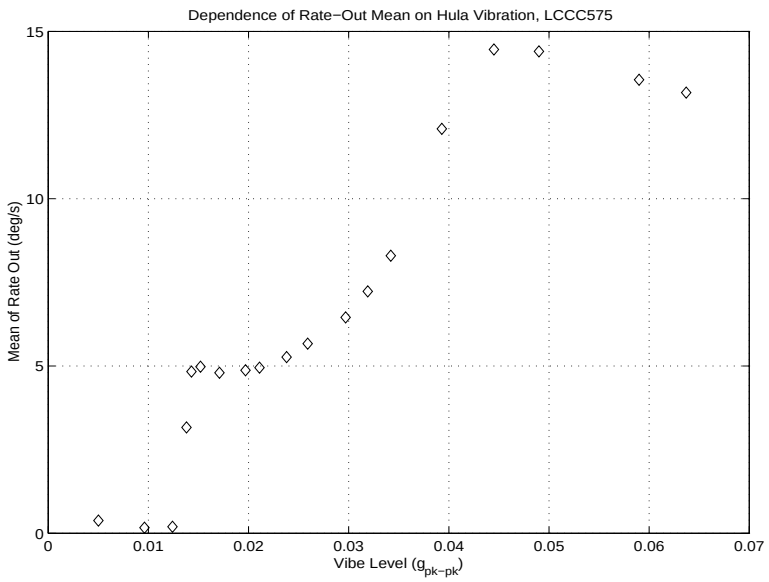

Figure 7-5: Dependence of Rate Mean on Hula Vibration, LCCC575

the applied vibration is well within 100 Hz of the tuning fork frequency, it is not attenuated at all by the filter, and appears strongly on rate-out. Figure 7-6 gives a typical example of rate-out for LCCC574 during a 0.2 g_{pk-pk} 12.454 kHz sinusoidal vibe. Note that the signal on rate-out has a frequency of about 0.7 Hz, so the applied vibration is 0.7 Hz away from the natural frequency.

The beating problem can be improved by reducing spring mismatch (and thereby reducing tuning fork response to vibration), or improving capacitor and amplitude matching between the two sides so that tuning fork charge injection to sense will more exactly cancel.

7.3.4 Hula Vibration Causes Motor Loop to Lose Lock

High vibration levels at the hula frequency produced enough hula mode motion that the motor loop would lose its lock on the tuning fork mode. For LCCC575, this caused all gyro signals to rail and locked up the device. Normal gyro operation could only be restored by shutting down power, waiting for 5-10 seconds to allow any motion to damp out, and turning power back on. When lock was lost on LCCC574, AC-out

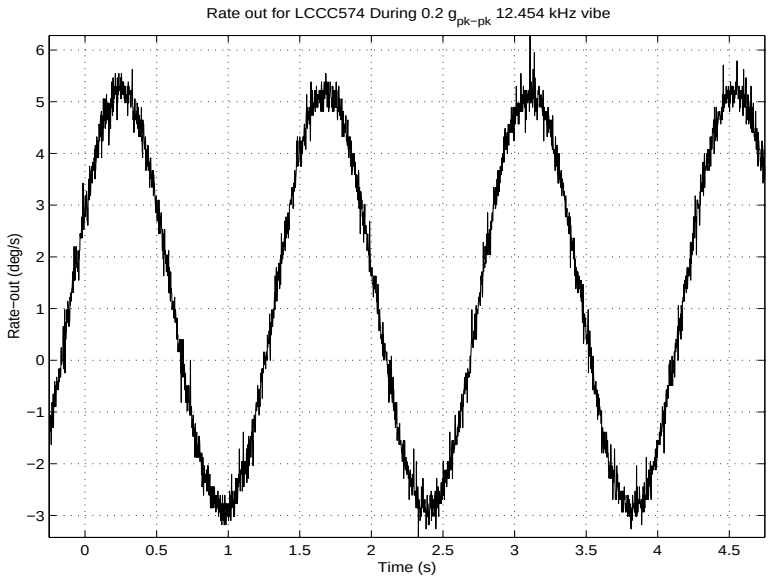

Figure 7-6: Rate-out for LCCC574 during 0.2 g_{pk-pk} vibe Near Tuning Fork

railed, but the position signal was a clean sinusoid at the hula frequency. Shutting off the vibration would allow the gyro to reacquire lock, and normal operation resumed after 10-20 seconds.

Lock was lost at a vibration level that created a hula amplitude equivalent to the driven tuning fork amplitude of 10 μm. For LCCC574, this occurred at a vibration input of 7.5 g_{pk-pk}, creating a hula amplitude of 9.76 μm. LCCC575 lost lock due to a vibration of 7 g_{pk-pk}, which drove hula at 9.4 μm. Figure 7-7 shows a PSD of the position signal just prior to loosing lock (7 g_{pk-pk}).

Driving the gyro at high enough amplitudes to lose lock did not seem to cause any serious permanent damage to the gyro. Hula motion was at most approximately 10 μm in amplitude, well with safe limits. The loss of lock was an electronic phenomenon, and although it saturated various components, no damage was done. Measurements of scale factor for both units before and after losing lock show no change; LCCC574 still maintains precisely 9.81 mV/(deg/s), and LCCC575 continues at 13.9 mV/(deg/s). Table 7.5 shows the values of a few closed loop parameters for the two units before and after they were driven to the point of loosing lock. Thus, although high levels of

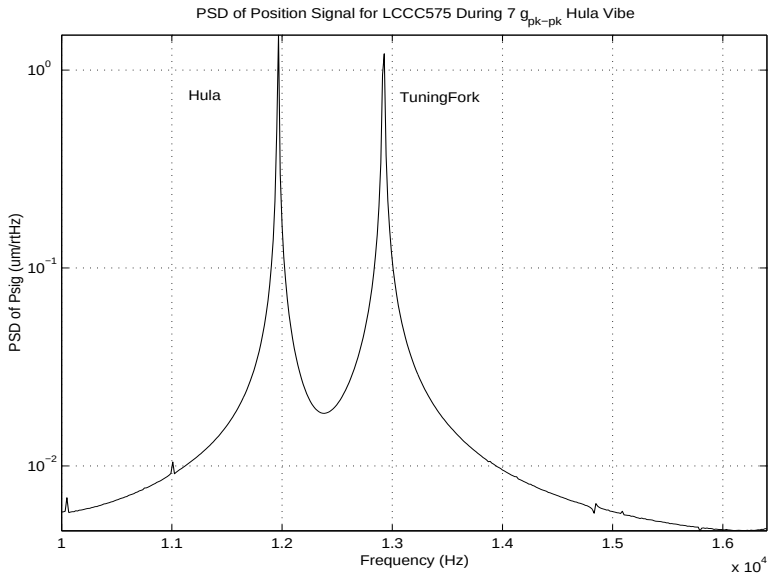

Figure 7-7: PSD of Position Signal for LCCC575 During 7 g_{pk-pk} 11.964 kHz Vibration

vibration can cause the gyro to shut down, normal operation can be restored with no permanent damage to the unit.

Parameter	LCCC574 Prior to Loosing Lock	LCCC574 After Loosing Lock and Reset	LCCC575 Prior to Loosing Lock	LCCC575 After Loosing Lock and Reset
Scale Factor (mV/(deg/s))	**9.8**	**9.8**	**13.9**	**13.9**
AGC (mV)	**493**	**470**	**444**	**429**
In-phase Bias (deg/s)	**2.041**	**1.306**	**0.360**	**0.402**

Table 7.5: Measurements of Characteristic Gyro Parameters before and After Lock Loss

Chapter 8

Impact Testing

Shock testing of the gyro when running open loop demonstrates the high-Q resonances of the tuning fork, and the coupling of structure resonances into gyro output. Since a shock excites mounting structure resonances, over a short time period the gyro is more correctly excited by the oscillating structure rather than a true delta function. The acceleration of the mounting structure after an impact was measured using the Endevco 2250A. Some data for fixture acceleration was shown in section 3.3.2 figures 3-10 and 3-11.

8.1 Summary

There are a few essential conclusions drawn from the results outlined in this chapter:

- Mounting structure resonances are excited by impact and drive the gyro. Thus, mechanical motion is produced not only at gyro resonances, but also at structural resonances. Structure vibration is more heavily damped than the high-Q gyro modes, and dies out more quickly.
- Mechanical response of the gyro to impact depends heavily on the width of the delivered pulse. A pulse more than 3 times the natural period of the gyro modes will excite very little response.

- Pulse sizes delivered by a steel on aluminum impact were on the order of 0.15-0.3 ms, about 2 or 3 times the gyro natural periods.

- Excellent agreement was observed between modeled and measured response of the gyro to impact, especially when accelerometer data was used as an input to the linear model. This increases confidence in the model.

- During closed loop operation, sense modal motion excited by impact is demodulated by tuning fork and appears at rate out. Thus, there is a strong erroneous signal at the difference frequency.

- AC-out can be easily clipped by impacts. (see section 2.4.1 for a discussion of clipping) Again, this depends heavily on impulse width and power, but displacement impulses delivered with the hand-held impact hammer on the order of $7.7{\cdot}10^{-10}\ m \cdot s$ in size and 0.15-0.3 ms in width clip AC-out.

- Sense mode response to impact causes the most problems during closed loop operation. Sense modal response to impact is heavily dependent on spring mismatch. With no mismatch, no sense response will be observed.

- As with all other gyro excitations, the effects of impact die out exponentially, with time constants determined by gyro Q. For the motor axis this is on the order of 1 s, for the sense axis on the order of 0.1 s.

8.2 Open Loop Testing

There are two main regions to gyro open loop impact response. The first region is a short region during which the structure is still ringing and driving the gyro at a resonance of the mounting structure. After this relatively low-Q ringing dies out, the gyro continues to oscillate at its own fundamental frequency, which has much lower damping. Both of these regions will be seen in gyro response to real environments; the resonances of the structure to which the gyro is mounted will appear on gyro outputs.

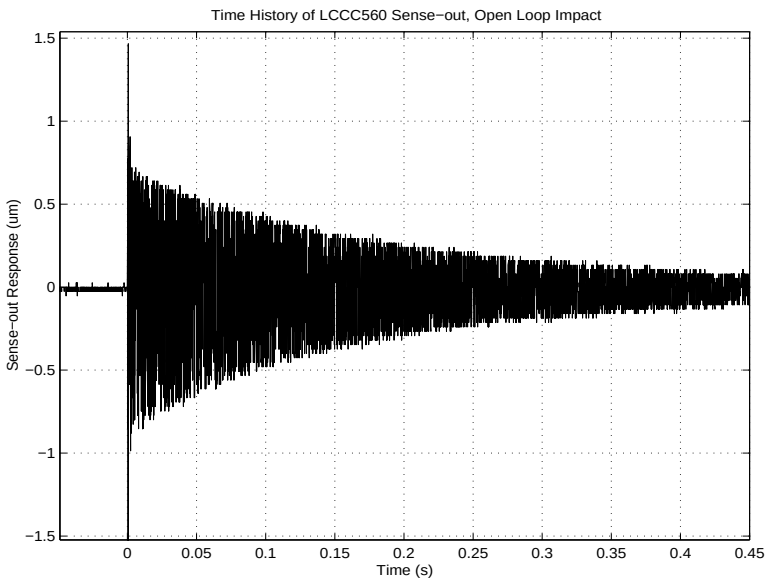

Figure 8-1: Time History of Sense Impact Response for LCCC560

8.2.1 Frequency Content of Open Loop Impact Response

Figure 8-1 gives a time history of sense-out for LCCC560 experiencing an impact at t=0. The initial region of the plot, from 0-4 ms, contains a lot of power at the fixture resonant frequencies. After this initial region, fixture response dies out, and only the high Q gyro modes remain in the response. Figure 8-2 shows a PSD of the sense-out signal during the first 10 ms. Figure 8-3 shows the PSD of sense-out for t>10 ms. There are some low frequency resonances (at 9.18 and 10.7 kHz) in the PSD for early times. These correspond to two of the strongest sense fixture modes listed in section 3.3.2. At later times, the only spike remaining in the PSD is at 16.677 kHz, which is the out-of-plane frequency for LCCC560.

Note also that impact does not excite the sense mode. For perfectly matched springs and masses, the two antiparallel modes (sense and tuning fork) will not be excited by any impact delivered to the gyro structure. Thus, impact will tend to excite the parallel modes (hula and out-of-plane).

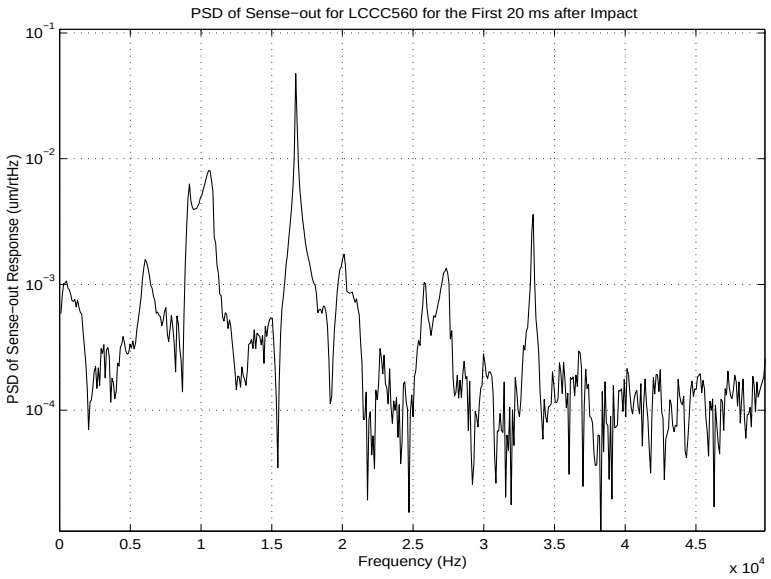

Figure 8-2: PSD of the first 15 ms of Sense Impact Response, LCCC560

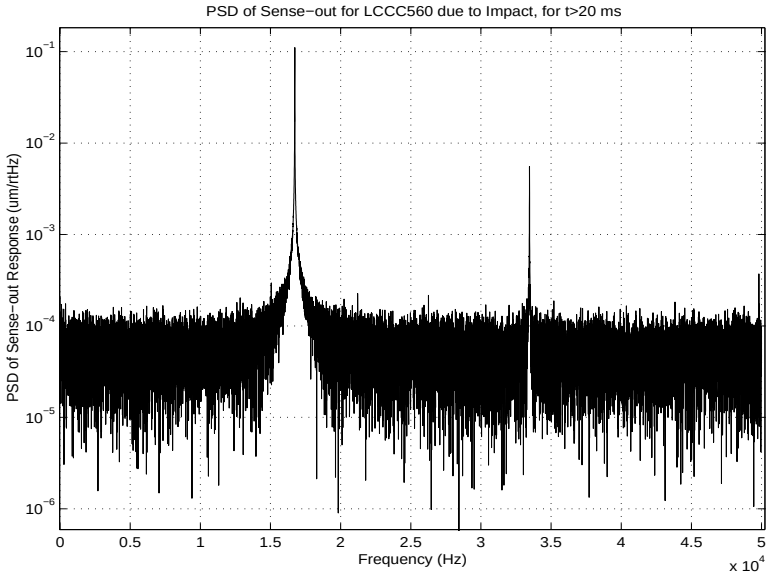

Figure 8-3: PSD of the Sense Impact Response after 7.5 ms, LCCC560

8.2.2 Simplified Modeling

It is important to know how large of a response will be seen due to a particular impact. To determine this, impact models must be developed. Refer to section 2.2.1 for the basic mechanical gyro model. If we assume matched springs and masses, the transfer function for the sense axis model reduced to (section 2.2.4)

$$\frac{Y_{1rel}}{Y_{ss}} = \frac{-ms^2}{ms^2 + b_y s + k_y} \tag{8.1}$$

Where:

Y_{1rel} is the displacement of the left proof mass out of the plane, measured relative to the substrate

Y_{ss} is the displacement of the substrate in the sense direction relative to inertial space

k_y is the sense flexure stiffness.

m is the proof mass mass.

b_y is the sense damping.

An identical derivation for the motor axis model, again with matched springs and masses, produces

$$\frac{X_{1rel}}{X_{ss}} = \frac{-ms^2}{ms^2 + b_x s + \frac{k_x k_{xf}}{k_x + 2k_{xf}}} \tag{8.2}$$

Where:

X_{1rel} is the motion of the left proof mass in the plane relative to the gyro substrate.

X_{ss} is the motion of the substrate in the motor direction relative to inertial space

k_{xf} is the sense flexure stiffness.

k_x is the basebeam to substrate anchor stiffness.

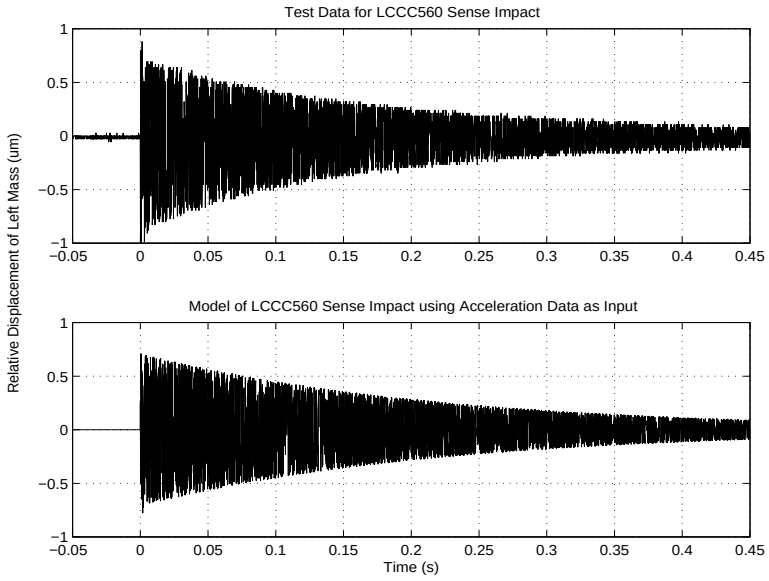

Figure 8-4: Comparison of Model of Sense Response to Actual Data, Acceleration Data Used as Input

m is the proof mass mass.

b_x is the motor damping.

Taking these transfer functions, we can compute the response of the linear system to any acceleration input. If the acceleration data taken by the reference accelerometer during a sense impact is used as the input to the linear model, excellent agreement is observed between model output and measured system response. Figure 8-4 shows the modeled and actual response.

8.2.3 Impact Modeling

For a true impact, the excitation will be a short input pulse in substrate position or acceleration. A pulse in substrate position is used for comparison with experiment rather than a pulse in acceleration, since during my experiments the structure undergoes no net displacement from the impact. Note that the model does not include the dynamics of the mounting structure, so will not reflect the early response where a lot

of fixture modes appear in gyro response.

The maximum output is highly dependent on the width of the pulse. A narrow pulse contains more power at high frequencies, which will excite the gyro resonances more effectively. The Dirac delta function models an infinitely narrow pulse. To compute the response to the delta function input, take the inverse Laplace transform of equations 8.1 and 8.2. The result is, for an infinitely narrow pulse in substrate position,

$$x_1(t) = -\delta(t) + \frac{\omega_n(1-2\zeta^2)}{\sqrt{1-\zeta^2}} e^{-\zeta\omega_n t} \sin(\omega_n\sqrt{1-\zeta^2}\ t) + 2\omega_n\zeta e^{-\zeta\omega_n t} cos(\omega_n\sqrt{1-\zeta^2}\ t) \tag{8.3}$$

Where:

$\delta(t)$ is the unit Dirac delta function.

ω_n is the natural frequency $= \sqrt{K/m}$ where $K = k_y$ for the sense axis, and $K = \frac{k_x k_{xf}}{k_x + 2k_{xf}}$ for the motor axis (see equations 8.2 and 8.1 above)

ζ is the damping coefficient, $= b/2\sqrt{mK} = 1/2Q$.

Note that, for $\zeta \ll 1$, equation 8.3 reduces to

$$x_1(t) = -\delta(t) + \frac{\omega_n}{\sqrt{1-\zeta^2}} e^{-\zeta\omega_n t} \sin(\omega_n\sqrt{1-\zeta^2}\ t) \tag{8.4}$$

The delta function in equation 8.3 indicates that with an infinitely thin displacement of the substrate, there is a delta function in the relative displacement of the proof mass and substrate. For a very narrow pulse this means that there will initially be a sharp spike in relative displacement, followed by the familiar exponentially decaying sine wave. Real inputs can never produce a true $\delta(t)$ in position, since the substrate and test structure have finite mass and thus cannot accelerate in zero time. Thus, for a real input function, we should use a smooth spike, which will allow the input to be spread over a finite time. The Gaussian curve serves well for this purpose. Thus, the theoretical position input signal, X_{ss} or Y_{ss}, will have the form

$$x(t) = \frac{1}{\sigma\sqrt{\pi}} e^{-\left(t^2/\sigma^2\right)} \tag{8.5}$$

Where:

σ^2 is the variance. The "width" of the pulse is approximately 4σ.

t is time.

$x(t)$ is the position input as a function of time.

This Gaussian is a unit Gaussian, the definite integral of the curve over the interval $t = [-\infty, +\infty]$ is exactly one. So, we will always deliver the same total impulse to the gyro model using the above input, but can vary the effective width of the pulse by varying σ. In the limit as the pulse gets very narrow, $\sigma \rightarrow 0$, the response will approach the case of the response to a delta function input, equation 8.3. The acceleration experienced by the substrate is the second derivative of equation 8.5,

$$a(t) = \frac{-2}{\sigma^3\sqrt{\pi}} e^{-\left(t^2/\sigma^2\right)} + \frac{4}{\sigma^5\sqrt{\pi}} t^2 e^{-\left(t^2/\sigma^2\right)} \tag{8.6}$$

Using this input function, we can model the response of the gyro plant to an impact. For an indicative case, take the system parameter values for LCCC560, and the input function shown in figure 8-5. The result of the linear simulation of sense axis motion is shown in figure 8-6.

A series of these results have been computed, determining the dependence of response size on impact pulse width. For LCCC560 sense axis, the simulation results are shown in figure 8-7. These should be typical of TFG14s in general. Figure 8-8 gives the results of an identical computation for the motor axis response of LCCC561 to impact. Note that at narrow impulse widths the response approaches the delta function response magnitude $\omega_n/\sqrt{1-\zeta^2}$. There is some threshold pulse width above which the response diminishes. The threshold is related to the natural frequency of the parallel resonant frequency for the direction of impact in question (that is, the hula or out-of-plane frequency). For impact pulses significantly wider than the natural period of oscillation, little response is seen.

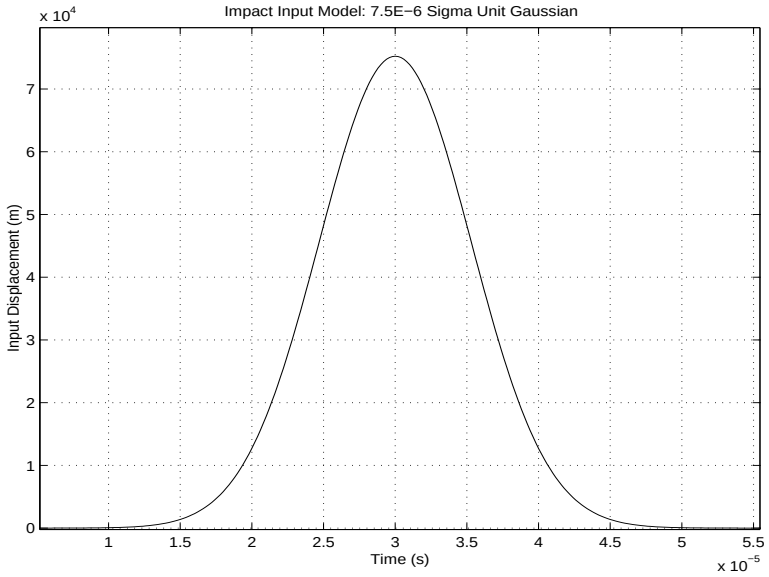

Figure 8-5: Typical Model Input, Unit Gaussian with Sigma=$7.5 \cdot 10^{-6}$ [second]

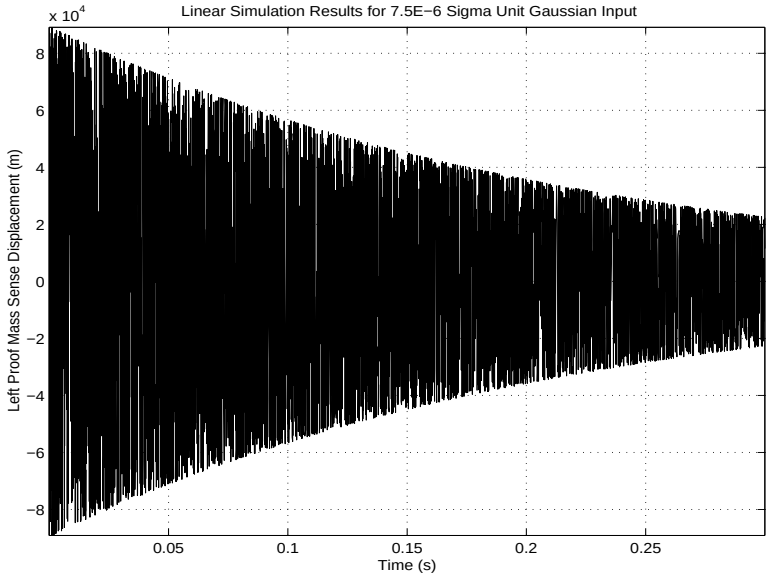

Figure 8-6: Linear Simulation Result for LCCC560 Left Sense Response to Gaussian Impact

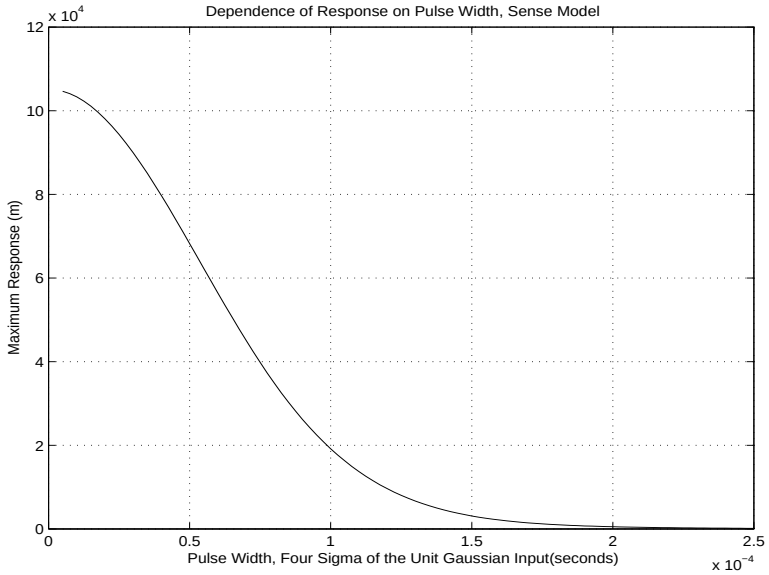

Figure 8-7: Modeled Dependence of Maximum Response on Position Pulse Width for LCCC560 Sense Axis

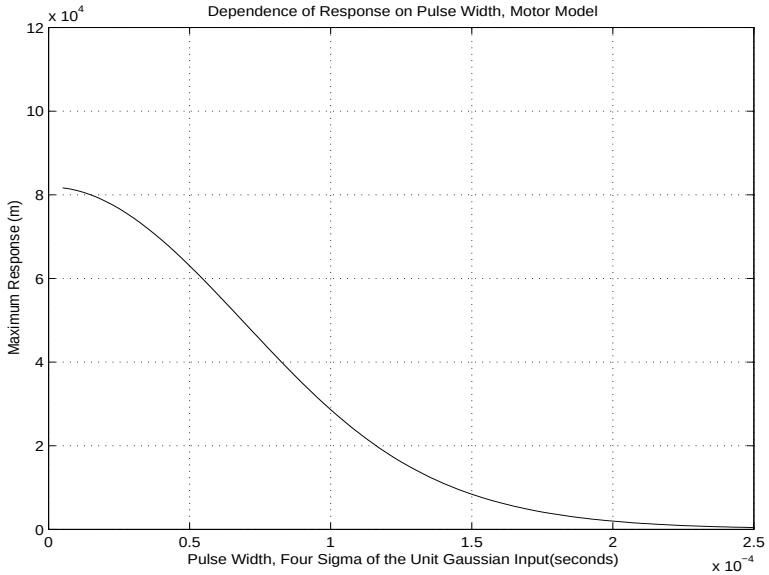

Figure 8-8: Modeled Dependence of Maximum Response on Position Pulse Width for LCCC561 Motor Axis

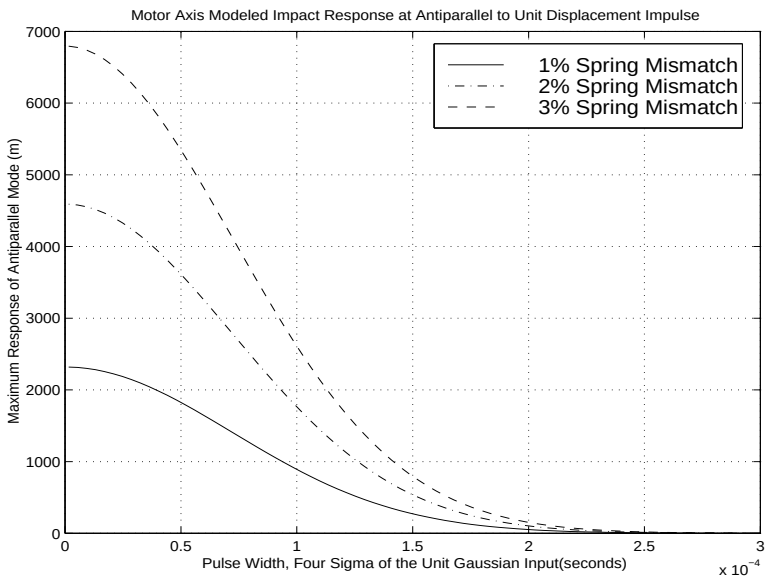

Figure 8-9: Model of Max Response to Position Impulse on Pulse Width for Motor Axis with Mismatch

With perfectly matched springs and masses, no response is generated at the antiparallel (sense and tuning-fork) modes due to impact. However, with spring mismatch, some motion at the antiparallel modes will be observed. Since motion out of the plane in the sense mode is preferentially detected by the sense chain, it is important to determine how large of a sense response can be expected. Including the effects of mismatched sense flexures, the response to impact can be computed. Figures 8-9 and 8-10 show the magnitude of response to impacts for various impact widths and spring mismatches. System parameters taken from data for LCCC575.

8.2.4 Response to Acceleration Impulse

Although all experiments conducted with the existing test setup deliver displacement impulses (there can be no net motion of the structure), the gyros may experience acceleration impulses in their operating environments. If, instead of a position input such as that given in equation 8.2 and 8.1, an acceleration input is considered, then the transfer functions become

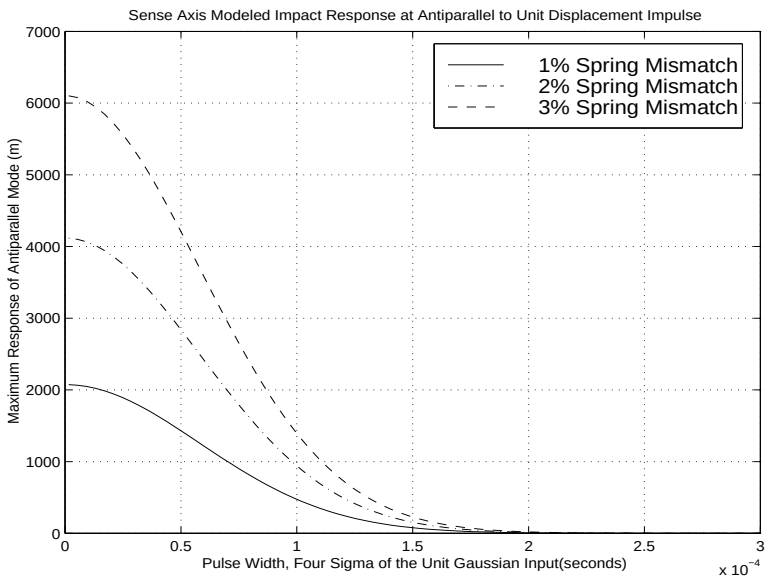

Figure 8-10: Model of Max Response to Position Impulse on Pulse Width for Sense Axis with Mismatch

$$\begin{aligned} \frac{X_{1rel}}{A_{xs}} &= \frac{-m}{ms^2 + b_x s + \frac{k_x k_{xf}}{k_x + 2k_{xf}}} \\ \frac{Y_{1rel}}{A_{ys}} &= \frac{-m}{ms^2 + b_y s + k_y} \end{aligned} \tag{8.7}$$

Where:

X_{1rel} is the motion of the left proof mass in the plane relative to the gyro substrate.

A_{xs} is the acceleration of the substrate in the motor direction relative to inertial space

Y_{1rel} is the displacement of the left proof mass out of the plane, measured relative to the substrate

A_{ys} is the acceleration of the substrate in the sense direction relative to inertial space

m is the proof mass mass.

k_{xf} is the sense flexure stiffness.

k_x is the basebeam to substrate anchor stiffness.

k_y is the sense flexure stiffness.

b_y is the sense damping.

b_x is the motor damping.

The inverse Laplace transform of 8.7 gives the response to a unit Dirac delta function acceleration impulse,

$$x(t) = -\frac{1}{\omega_n\sqrt{1-\zeta^2}}e^{-\zeta\omega_n t}\sin(\omega_n\sqrt{1-\zeta^2}t) \tag{8.8}$$

This is the limit for an extremely narrow impulse in substrate acceleration. Note that there is no delta function in the response for the acceleration impulse response. As done previously for the case of a position impulse, we can use the Gaussian function as a finite width impulse input. This allows examination of the dependence of the response on pulse width.

$$a(t) = \frac{1}{\sigma\sqrt{\pi}}e^{-(t^2/\sigma^2)}$$

Varying the pulse width, σ, but maintaining a total unit impulse, $\int_{-\infty}^{+\infty} a(t)\ dt = 1\ [m/s]$, we can generate a series of theoretical responses. The results are summarized in figures 8-11 to 8-14, where the maximum response is plotted verses the impulse width, always for a input acceleration Gaussian input. For the antiparallel modes, 3 cases are considered with different spring mismatch percentages.

From the results shown in the figures, we see that a narrow motor direction acceleration pulse with a total impulse of ≈ 0.5 m/s will begin to clip AC-out (3.5-4 μm of hula motion clips AC-out, see section 2.4.1). A narrow sense acceleration impulse of ≈ 0.1 m/s could clip AC-out depending on spring mismatch. With a 1% spring mismatch, 0.1 μm of differential motion (=0.05 μm amplitude) would be created by a 0.1 m/s acceleration impulse. An 0.2 m/s narrow sense acceleration impulse could create

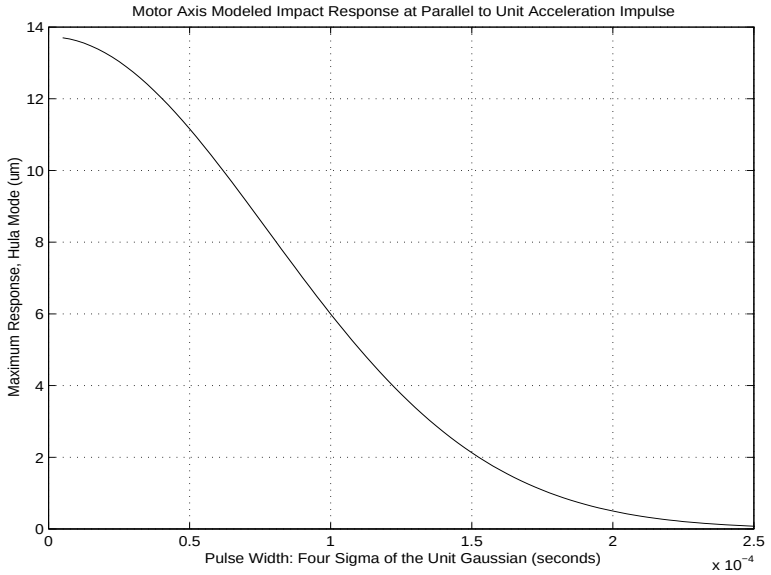

Figure 8-11: Modeled Dependence of Hula Mode Response to Motor Impact Pulse Width

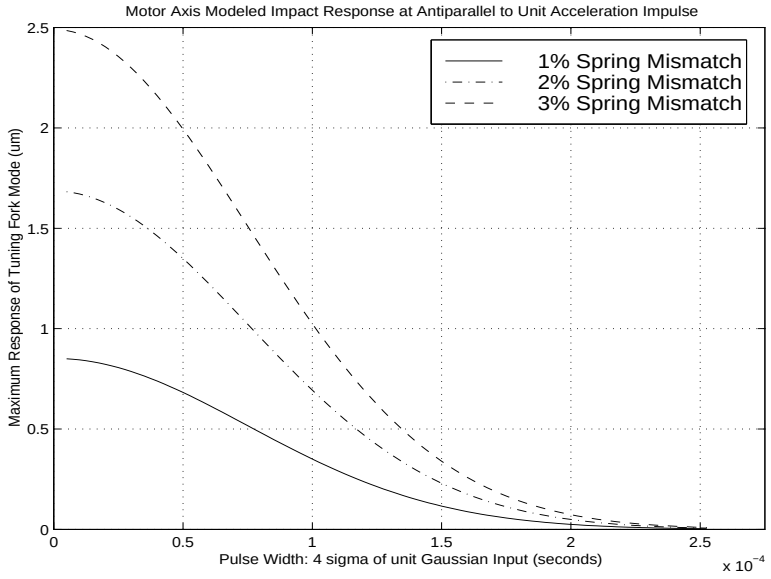

Figure 8-12: Modeled Dependence of Tuning Fork Mode Response to Motor Impact Pulse Width

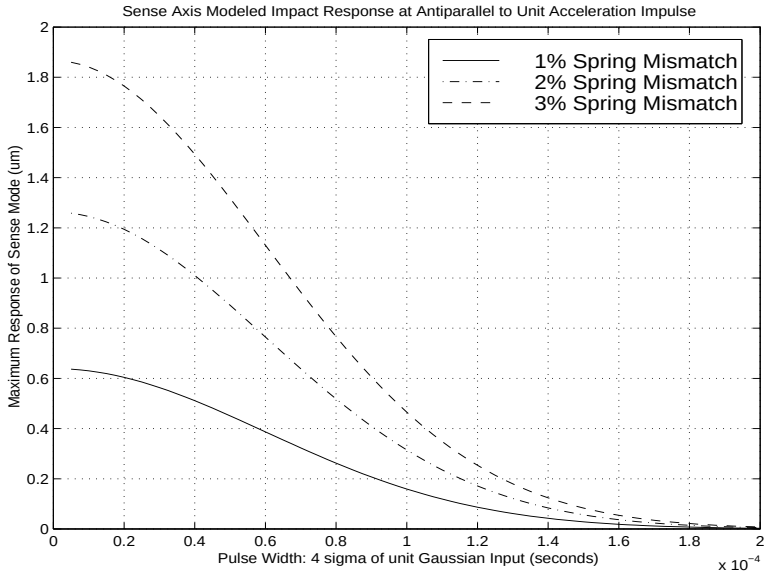

Figure 8-13: Modeled Dependence of Sense Mode Response to Sense Impact Pulse Width

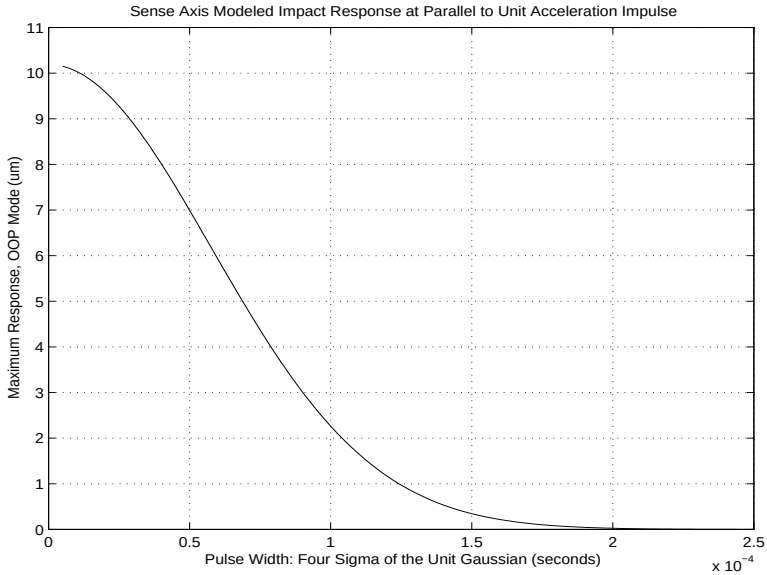

Figure 8-14: Modeled Dependence of Out-of-Plane Mode Response to Motor Impact Pulse Width

enough out-of-plane mode motion to cause snapdown. (2 μm) For wider impulses the level of response diminishes dramatically, as seen in the figures.

8.3 Experimental Closed Loop Impact Results

Experimentally, it was not possible to deliver impacts with widths less than approximately 0.2-0.3 ms, even with the hardest impulse hammer tip available. Thus, it was not possible to experimentally examine the extremely narrow pulse width limit predicted above in section 8.2.3. However, for verification of the theory presented above, experimental impact response could be measured at the available impact widths and compared to experiment. In this section the experimental closed loop impact responses are presented, and the effects of impact on the gyro outputs are considered.

8.3.1 Experimental Impact Frequency Content

As shown above, the magnitude of gyro response depends heavily on the frequency content of the impact. Impacts with the same total impulse (that is, the integral of force over time) have very different effects depending on whether the impulse is delivered over a short or long period of time. If there is little power in the impact at the gyro resonant frequencies, little response will be observed.

Measurements of the frequency content of various types of impacts have been recorded. The impulse hammer, as described in section 3.5.3, has a number of tips which can be used to determine the frequency content of a particular impact. Figure 8-15 is a PSD of the hammer force sensor output for the hard steel tip. This impact has the most high frequency content. Figure 8-16 is a PSD for the softest plastic bubble tip.

We can define the effective bandwidth of each tip as the frequency at which the force PSD in $N/\sqrt{Hz}$ has diminished by two orders of magnitude from its low frequency level.

- Black hard steel tip bandwidth = 11 kHz

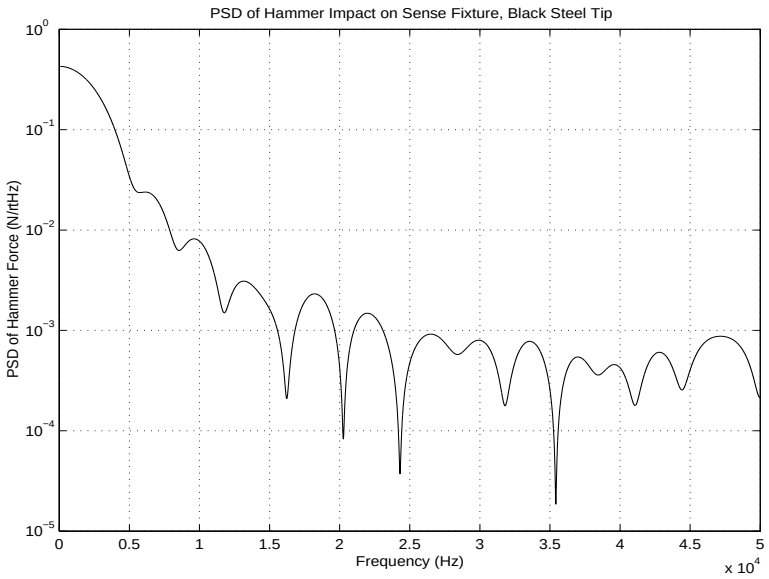

Figure 8-15: PSD of the Hammer Force Sensor, Black Steel Tip

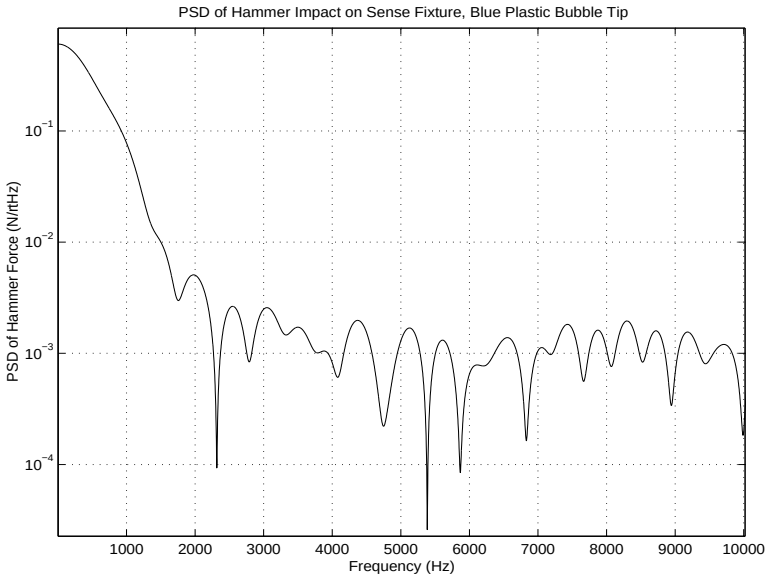

Figure 8-16: PSD of the Hammer Force Sensor, Soft Bubble Tip

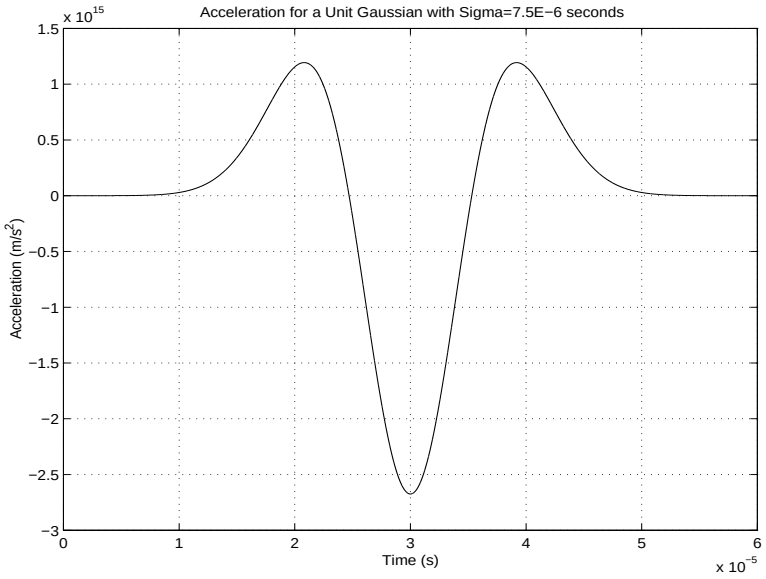

Figure 8-17: Acceleration For a 0.1 Sigma Unit Gaussian Displacement

- White hard plastic tip bandwidth = 5.7 kHz
- Red small soft bubble tip bandwidth = 1.6 kHz
- Blue large soft bubble tip bandwidth = 1.7 kHz

Impact with the hard steel tip was used for all impact testing, since it causes the largest gyro response.

To compare the measured results with the model, we need to determine how large of a displacement pulse is generated by a standard impact with the steel tip. Equation 8.6 gave the acceleration corresponding to a unit Gaussian displacement. Figure 8-17 shows a plot of this acceleration against time.

The acceleration delivered to the gyro is not so simple, however. The dynamics of the mounting structure significantly shape the acceleration signal. Figure 8-18 shows the fixture acceleration caused by an impact to the sense fixture. It is accelerations of this sort which actually end as the input to the gyro. It is extremely important to consider the structure resonances. As long as the structure resonances all have natural periods longer than the threshold pulse width discussed in section 8.2.3, there will

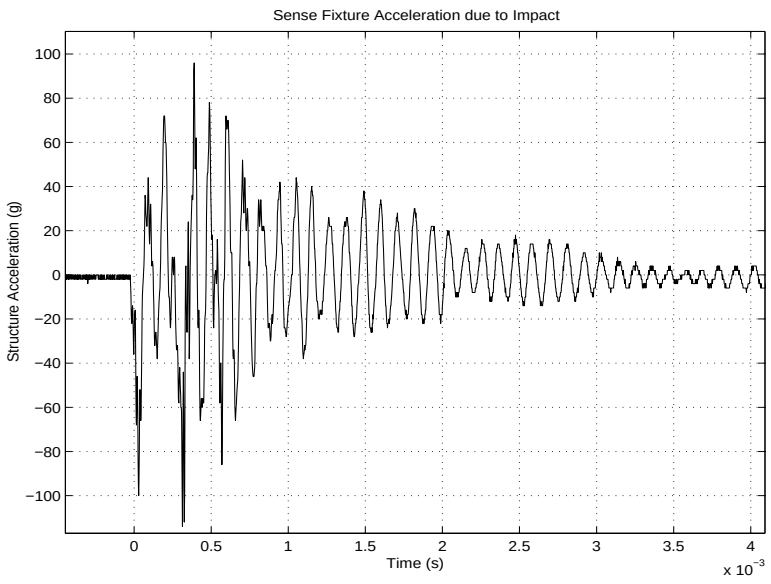

Figure 8-18: Typical Sense Fixture Acceleration due to Impact

be less gyro response. When designing mounting structures for the gyro, natural frequencies should be kept below the threshold, to avoid exciting gyro modes due to impacts to the mounting structure.

Although the fixture dynamics contribute to the forcing, it is convenient to consider the impact to be a pulse. The force delivered by the hammer during an impact has been recorded using the internal force sensor in the hammer. This force relates to acceleration of the mounting fixture as

$$a_{fixture} \approx \frac{F_{hammer}}{m_{fixture}}$$

The overhung fixture has mass, $m \approx 400g$. Using the above relationship, we can compute the initial acceleration of the structure from the hammer input. If this assumption is valid, the computed acceleration should approximate the first spike in the accelerometer measurement. Figure 8-19 shows that this is indeed true; the assumption seems to be at least approximately valid. From the figure, we can also see that the width of the impulse is approximately 0.3 ms.

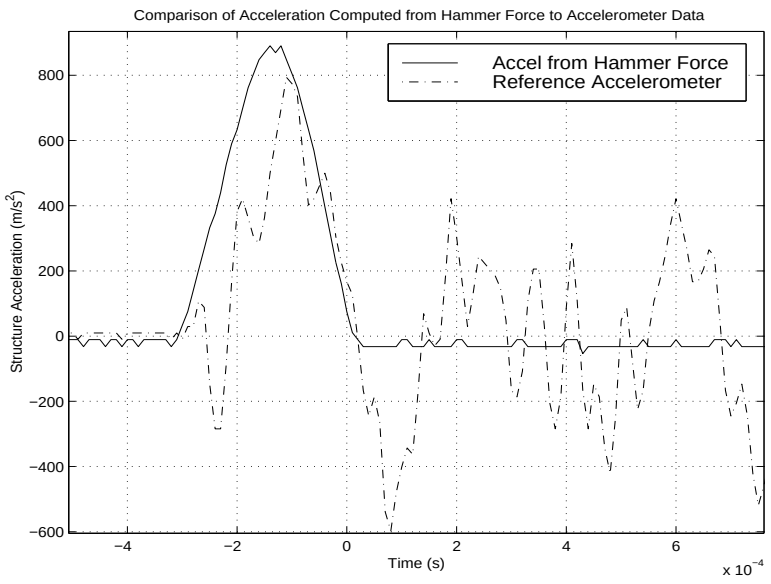

Figure 8-19: Acceleration Computed from Hammer Force Compared With Accelerometer Measurement

To get the total size of the position impulse (that is, the integral of the fixture displacement over the initial spike), we should integrate the acceleration from figure 8-19 three times,

$$I = \int_0^{0.3\text{ms}} \int\int a(t'')\ dt''\ dt'\ dt \approx 7.7 \cdot 10^{-10}[m \cdot s] \tag{8.9}$$

With an impulse size of approximately $8{\cdot}10^{-10}\ m \cdot s$,such as that seen in figure 8-4, a response of $\approx 0.5 - 1\ \ \mu m$ (this is the response size observed) would require a pulse width of approximately 0.15-0.23 ms. This is a shorter pulse than the one recorded by the hammer force sensor, but is about the same length as the spike seen in the accelerometer output. Thus, it is probably better to use the accelerometer as an indication of the size of the spike, especially since the hammer bandwidth is about 7.76 kHz, so some broadening of the peak is expected. However, considering the approximations that have been made, excellent agreement is seen between expected and measured response. This increases confidence in the model, and strongly supports the theoretical computations presented in this chapter.

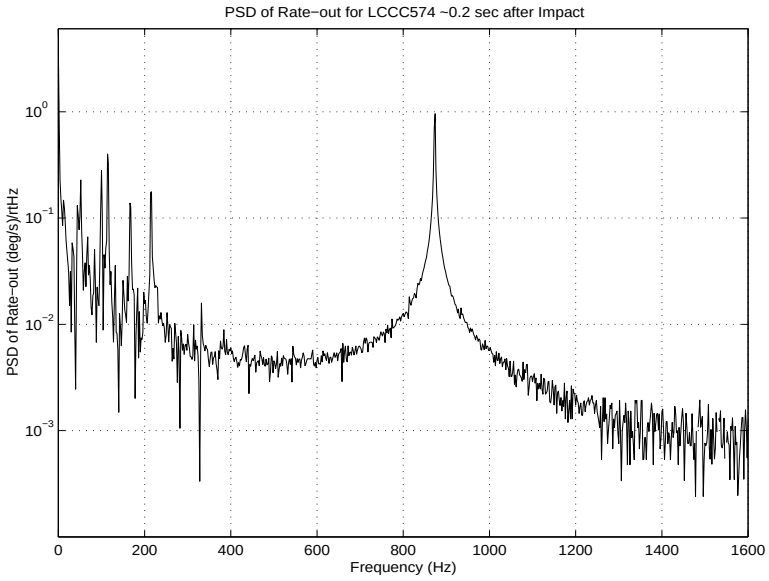

Figure 8-20: PSD of Rate-out for LCCC574 soon after Impact

8.3.2 Closed Loop Impact Testing

Impact during closed loop operation excites the same mechanical motion described above in section 8.2. Now, motion of the sense axis in the out-of-plane and sense modes appears as a signal on AC-out, and is demodulated with the velocity clock taken from the position signal. Although the out-of-plane mode is excited much more strongly by impact than the sense mode, the differential sense capacitance scheme nulls out most of the signal coming from out-of-plane.

Thus, the sense mode appears more strongly on AC-out, even though the amplitude of sense mode motion is lower. Some out-of-plane signal is also seen because of mismatched capacitors. The sense mode and out-of-plane mode signals are demodulated with the velocity clock, producing sidebands at the difference frequencies, $\omega_{sense} - \omega_{tunefork}$ and $\omega_{oop} - \omega_{tunefork}$. These sidebands are low-pass filtered by the four-pole rate-out filter. The resulting signal appears on rate-out.

A PSD of the rate-out signal soon after impact clearly shows the predominance of the $\omega_{sense} - \omega_{tunefork}$ frequency. Figure 8-20 gives the PSD of rate-out for LCCC574 0.2 s after impact.

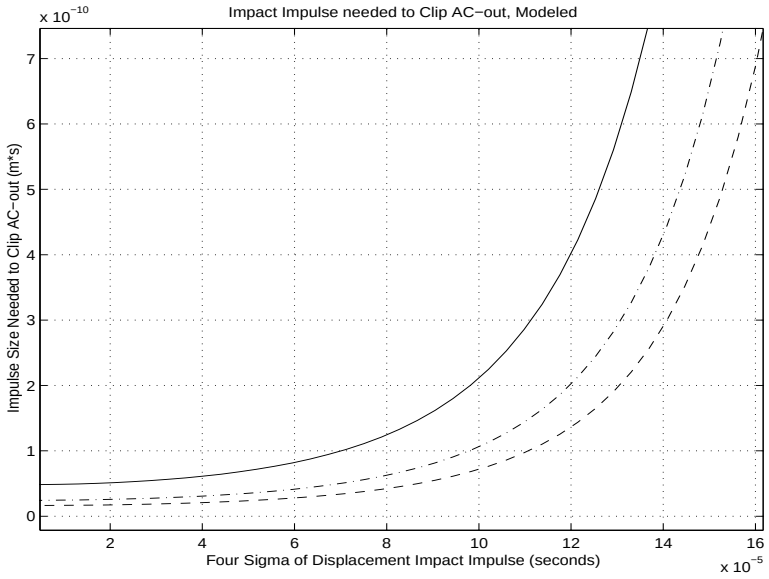

Figure 8-21: Theoretical Impulse Needed to Rail AC-out

Another danger during impact is clipping of AC-out. AC-out will saturate at the power supply level of 15 V. If the sense mode is excited at an amplitude of more than 0.1 μm peak, AC-out will clip. ($3V/(\mu m)$ of differential motion, and a gain of 50 in the sense-out chain). The results in section 8.2.3 indicate the levels of impact needed to cause this much motion. Figure 8-21 plots the impact impulse needed to clip AC-out against pulse width for a number of different spring mismatches.

One final issue to be considered is excitation of hula motion in the motor axis. The velocity clock is a square wave created from the position signal. Since the majority of the motor motion should still be in the tuning fork mode, it is unlikely that the velocity clock will be affected by impact. A large enough impact could cause the gyro to lose lock completely, but my test setup cannot deliver impacts of this magnitude.

Another way that hula motion could cause errors in rate readings is through Coriolis effects. If there is substantial hula motion of the masses, a DC rate will create a Coriolis acceleration at the hula frequency as well as at the tuning fork frequency. Thus, we would expect to see some output on rate-out at the difference between hula and drive. However, the Coriolis acceleration created due to hula motion will force

both masses out of the plane in phase with each other. Parallel sense motion of this type is rejected by the differential scheme used on the sense axis. So, hula effects on rate-out should be quite small. See section 2.2.3 for a discussion of coriolis effects, in particular equation 2.12 and figure 2-7. No signal is seen on rate out at the difference between hula and tuning fork during testing.

Chapter 9

Conclusions

The linear gyro models developed in section 2.2.1 account well for most of the vibration and impact effects seen. These models capture the essential modal behavior of the gyro, incorporating vibration effects and spring mismatch. Measurement of the model parameters was conducted for each unit, as described in section 4.

Testing indicated gyro Q of approximately 12,000 on the sense axis, and 180,000 on the motor axis. Measurements of cubic spring nonlinearities showed that cubic spring softening occurs, with cubic spring constants on the order of -4·10^9 N/m^3, which results in a reduction in spring stiffness of approximately 0.14 % at an amplitude of 10 μm. Since cubic spring softening is small, it will be neglected in the model. However, it does become important in considering the response of a particular gyro mode to vibration at resonance, since the resonant peak will shift down slightly with increasing amplitude. Chapter 4 goes into more detail on these issues.

Open loop testing was conducted to verify modeling, determine spring mismatch, and measure the actual response of various gyro modes to sinusoidal and random vibration. The mechanical models of section 2.2.1 predict the correct order of magnitude for gyro open loop response to both sinusoidal and open loop vibration. However, differences of as much as 250% are seen between expected and observed response in the worst case. It is not clear where this error is coming from.

Response of the anti-parallel modes to open loop vibration gave an estimate of motor and sense spring mismatch. Spring mismatch is between 0 and 2%.

During applied mechanical vibration, it is important to consider not only gyro resonant modes, but also modal response of the mounting structure. In addition to gyro modal frequencies, fixture modal frequencies are seen in gyro response. This will be true not only for my test fixture, but for any mounting system used during normal gyro operation.

The time constant for the growth of gyro response to open loop vibration is on the order of 1 s for the motor axis, and 0.1 s for the sense axis. These values were predicted from gyro Q measurements and observed during ringup tests.

Estimates for the maximum safe levels for both random and sinusoidal vibrations near each modal frequency were determined. The values presented in table 9.1 are the maximum vibrations that can be sustained without clipping AC-out, causing the gyro to lose lock on the tuning-fork mode, or causing permanent damage due to snapdown or contact in the motor combs. Chapter 5 describes the open-loop testing results in depth.

Low frequency vibration of the closed loop system showed that the gyro was insensitive to vibration at every frequency in the 0-3 kHz band with the important exception of vibration at the difference between the sense and drive frequencies. Vibration at this frequency excites substantial sense mode motion, and can cause AC-out to rail. The sense mode is excited due to rocking of the structure at the applied vibration frequency. Measurements of fixture rocking indicate that rocking at the difference frequency with amplitude on the order of 0.1-0.3 $(rad/s)_{pk-pk}$ will cause AC-out to clip.

Angular vibration at this difference frequency causes errors on rate-out at the difference frequency and at the sense frequency, for levels above 0.1 $(rad/s)_{pk-pk}$. These erroneous components of rate-out have magnitude on the order of 0.1-0.2 deg/s. The mean of rate out also changes due to vibration at the difference frequency, drifting on the order of 0.01 (deg/s) of measured vibration per deg/s of fixture rocking.

Low frequency random vibration in the 0-6.4 kHz band causes substantial response on rate out. However, almost all of the signal on rate-out during low frequency random vibration comes from real rotation of the test structure at structure resonances.

Erroneous signals do appear due to excitation of the hula and sense modes (particularly hula), which are driven by high frequency components in the applied random vibration. These couple through into rate-out and are demodulated, creating errors on rate-out at the difference between tuning fork and hula, and tuning fork and sense. Low frequency testing is detailed in chapter 6.

The gyro is insensitive to high frequency vibration except near gyro resonant frequencies. In particular, the tuning fork gyro is very sensitive to vibration at the hula frequency. Vibration levels of 0.015 g_{pk-pk} at hula will begin to clip AC-out. Amplitudes of more than 0.015 g_{pk-pk} have a major effect on the mean of rate-out, causing shifts of up to 17 deg/s. Sinusoidal vibration at the hula frequency of approximately 7 g_{pk-pk} causes the motor loop to lose lock completely, and gyro operation ceases. This level of vibration is the level needed to produce a hula mode amplitude of 10 μm, the nominal tuning-fork amplitude. Although no permanent damage to the gyro is incurred, the gyro can lock up until power is shut off.

Vibration near the tuning fork frequency creates a low frequency signal on rate-out at the difference between the applied vibration and tuning-fork frequencies, even at low acceleration levels (<0.1 g_{pk-pk}). This component can become quite large, 40 $(deg/s)/g_{pk-pk}$ was observed.

High frequency random vibration in the 11-19 kHz band excites all four major modes. Due to sensing schemes and mechanical gains the sense modal and hula modal frequencies are predominant on AC-out. Random vibration creates an erroneous rate-out component at the difference between hula and tuning fork, on the order of 1 deg/s for a 0.5 g_{rms} 11-19 kHz random vibe. Levels of approximately 0.025 $g/\sqrt{Hz}$ in the 11-19 kHz band excite enough hula and sense motion to begin clipping AC-out. Random vibration levels of more than 0.005 $g/\sqrt{Hz}$ will shift the mean of rate-out by as much as 2 deg/s, and cause it to become very unstable, shifting randomly as much as 6 (deg/s) in 30 seconds. All of the high frequency test results are presented in chapter 7.

Impact testing indicated that mounting structure resonances are excited by impact and drive the gyro. Thus, mechanical motion is produced not only at gyro resonances,

but also at structural resonances. Structure vibration dies out much more quickly than the high-Q gyro modes.

Mechanical response of the gyro to impact depends heavily on the width of the delivered displacement pulse. A pulse more than 3 times the natural period of the gyro modes will excite very little response. Pulse sizes delivered by a steel on aluminum impact were on the order of 0.15-0.3 ms, about 2 or 3 times the gyro natural periods.

During closed loop operation, sense modal motion excited by impact is demodulated by tuning fork and appears at rate out. Thus, there is a strong erroneous signal at the difference frequency. In addition, AC-out can be easily railed by impacts. Again, this depends heavily on impulse width and power, but impulses delivered with the hand-held impact hammer on the order of $7.7{\cdot}10^{-10}\ m \cdot s$ in size and 0.15-0.3 ms in width rail AC-out. Sense modal response to impact is heavily dependent on spring mismatch. With no mismatch, no sense response will be observed. Chapter 8 describes all impact test results in depth.

For all mechanical gyro excitations, the effects die out exponentially, with time constants determined by gyro Q. For the motor axis this time constant is on the order of 1 s, for the sense axis on the order of 0.1 s. Thus, within 10 seconds of an applied mechanical excitation, gyro operation returns to normal, unless lock was lost on the tuning fork mode due to an excessively large excitation.

Table 9.1 gives a summary of the various types of vibration excitation that cause errors or could potentially damage the gyro. Approximate values for the maximum levels of vibration that can be sustained are given, for three cases: the amount of vibration that will start to clip AC-out (this occurs at 0.1 μm of sense motion, or 3-4 μm of hula motion), the amount of vibration needed to lose tuning fork lock (caused by 10 μm of hula motion), and the levels at which permanent damage could be incurred (greater than 25 μm of motor axis amplitude, or 2 μm of sense axis amplitude). Response will vary from unit to unit, particularly due to spring mismatch. The data in the table is determined from theory and test results as presented throughout.

Table 9.2 gives similar results for safe levels of impact (total impulse delivered). Two cases are considered: short pulses (less that 0.01 ms in duration), and pulses

Type of Excitation	Motion Produced per Input	Maximum Level without Clipping AC-out (assumes gain of 50 between preamp out and AC-out)	Maximum Level without Causing Gyro to Lose Lock	Maximum Level without Causing Potentially Permanent Damage
Sinusoidal Rocking at f_{sense}-$f_{tunefork}$	**2 μm/(rad/s) of sense mode**	**0.05 $(rad/sec)_{peak}$**	**Will not lose lock**	**0.5 rad/s**
Sinusoidal Vibration at Hula	**100-800 μm/g hula motion at nonlinear resonance**	**0.005 g_{pk-pk} at low amplitude resonant frequency. (Corresponds to 3-4 μm_{pk-pk} hula motion)**	**6.5 g_{pk-pk} at resonant frequency, measured experimentally for two units**	**0.03 g_{pk} at nonlinear resonance**
Sinusoidal Vibration at Tuning Fork	**creates tuning fork motion, depends on spring mismatch, 1% = 8 μm/g 2% = 16 μm/g**	**high levels, depending on capacitor mismatch**	**Will not lose lock**	**2.5 g_{pk} at nonlinear resonance**
Sinusoidal Vibration at Sense	**creates sense mode motion, depends on spring mismatch, 1% = 0.4 μm/g 2% = 0.8 μm/g**	**depends on spring mismatch, 1% = 0.25 g_{pk-pk} 2% = 0.12 g_{pk-pk}**	**Will not lose lock**	**depends on spring mismatch, 1% = 5 g_{pk-pk} 2% = 2.5 g_{pk-pk}**
Sinusoidal Vibration at Out-of-plane	**10 μm/g, out-of-plane mode**	**1% sense capacitor mismatch, clips AC-out at 1 g_{pk}**	**Will not lose lock**	**0.2 g_{pk}**
Random Vibration in High Frequency Band along Drive Direction	**Hula: 50-250 μm/g/√Hz Tunefork:0-3.5 μm/g/√Hz**	**0.015 g/√Hz causes 3.75 μm_{pk} hula motion, clips AC-out**	**0.05 g/√Hz, due to hula motion**	**0.1 g/√Hz causes 25 μm_{pk} hula motion**
Random Vibration in High Frequency Band along Sense Direction	**Sense:0-8 μm/g/√Hz OOP:3-20 μm/g/√Hz**	**0.013 g/√Hz, createsμm_{pk} 0.1 much sense mode**	**Will not lose lock**	**0.1 g/√Hz could cause snapdown**

Table 9.1: Summary of Safe Vibration Levels

of the width generated by steel on aluminum hammer impacts. Longer impacts than this will generate substantially less response; the response falls off exponentially with the width of the pulse. Both displacement and acceleration impulse excitations are presented. These results, although supported by experiment as demonstrated in chapter 8, are more theoretical.

Type of Excitation	Motion Produced Divided by Total Impulse Delivered in m·s or m/s as appropriate	Maximum Level without Clipping AC-out	Maximum Level without Causing Gyro to Loose Lock	Maximum Level without Causing Potentially Permanent Damage
Motor Direction Narrow Position Impulse (<0.01 ms)	**Hula:$8\cdot10^{10}$ μm_{pk}/m·s TuneFork: $2\cdot10^{9}$ -$7\cdot10^{9}$ μm_{pk}/m·s, 1%-3% mismatch**	**$4\cdot10^{-11}$ m·s creates 3.75 μm_{pk} hula motion, clips AC-out**	**$1.3\cdot10^{-10}$ m·s creates 10 μm_{pk} hula motion**	**$3\cdot10^{-10}$ m·s creates 25 μm_{pk} hula motion**
Sense Direction Narrow Position Impulse (<0.01 ms)	**Sense:$2\cdot10^{9}$ -$8\cdot10^{9}$ μm_{pk}/m·s 1%-3% mismatch OOP: $1\cdot10^{11}$ μm_{pk}/m·s**	**$6\cdot10^{-12}$ m·s could create 0.1 $\mu m_{pk\text{-}pk}$ sense mode motion, clips AC-out**	**Will not lose lock**	**$2\cdot10^{-11}$ m·s could cause snapdown due to 2 μm_{pk} out-of-plane mode**
Motor Direction Steel on Aluminum Position Impulse (~0.2 ms)	**Hula:$3\cdot10^{9}$ μm_{pk}/m·s TuneFork:$0.5\cdot10^{8}$ -$1.5\cdot10^{8}$ μm_{pk}/m·s, 1%-3% mismatch**	**$1.3\cdot10^{-9}$ m·s creates 3.75 μm_{pk} hula motion, clips AC-out**	**$3.3\cdot10^{-9}$ m·s creates 10 μm_{pk} hula motion**	**$8.7\cdot10^{-9}$ m·s creates 25 μm_{pk} hula motion**
Sense Direction Steel on Aluminum Position Impulse (~0.2 ms)	**Sense: $5\cdot10^{6}$ -$2\cdot10^{7}$ μm_{pk}/m·s 1%-3% mismatch OOP: $5\cdot10^{8}$ μm_{pk}/m·s**	**$2.5\cdot10^{-9}$ m·s could create 0.1 $\mu m_{pk\text{-}pk}$ sense mode motion, clips AC-out**	**Will not lose lock**	**$4\cdot10^{-9}$ m·s could cause snapdown due to 2 μm_{pk} out-of-plane mode**
Motor Direction Narrow Acceleration Impulse(<0.01 ms)	**Hula:14 μm_{pk}/m/s TuneFork: 0.7-2.5 μm_{pk}/m/s, 1%-3% spring mismatch**	**0.27 m/s creates 3.75 μm_{pk} hula motion, clips AC-out**	**0.72 m/s creates 10 μm_{pk} hula motion**	**1.8 m/s creates 25 μm_{pk} hula motion**
Sense Direction Narrow Acceleration Impulse(<0.01 ms)	**Sense:0.6-1.9 μm_{pk}/m/s 1%-3% spring mismatch OOP: 10 μm_{pk}/m/s**	**0.025 m/s could create 0.1 $\mu m_{pk\text{-}pk}$ sense mode motion, clips AC-out**	**Will not lose lock**	**0.2 m/s could cause snapdown due to 2 μm_{pk} out-of-plane mode**
Motor Direction Steel on Aluminum Acceleration Impulse (~0.2 ms)	**Hula: 0.5 μm_{pk}/m/s TuneFork:0.02-0.08 μm_{pk}/m/s, 1%-3% spring mismatch**	**7.5 m/s creates 3.75 μm_{pk} hula motion, clips AC-out**	**20 m/s creates 10 μm_{pk} hula motion**	**50 m/s creates 25 μm_{pk} hula motion**
Sense Direction Steel on Aluminum Acceleration Impulse (~0.2 ms)	**Sense: $2\cdot10^{-3}$ -$8\cdot10^{-3}$ μm_{pk}/m/s 1%-3% spring mismatch OOP: 0.025 μm_{pk}/m/s**	**6.25 m/s could create 0.1 $\mu m_{pk\text{-}pk}$ sense mode motion, clips AC-out**	**Will not lose lock**	**8 m/s could cause snapdown due to 2 μm_{pk} out-of-plane mode**

Table 9.2: Summary of Safe Impact Levels

Appendix A

Derivation of Linear Models

The linear models used in this thesis are derived in more detail here.

A.1 Motor Model

The motor model is taken from the lumped element model in figure A-1.

Where

x_1 = displacement of the left proof mass in the plane with respect to inertial space

x_2 = displacement of the right proof mass in the plane with respect to inertial space

x_{bb} = displacement of the basebeam with respect to inertial space

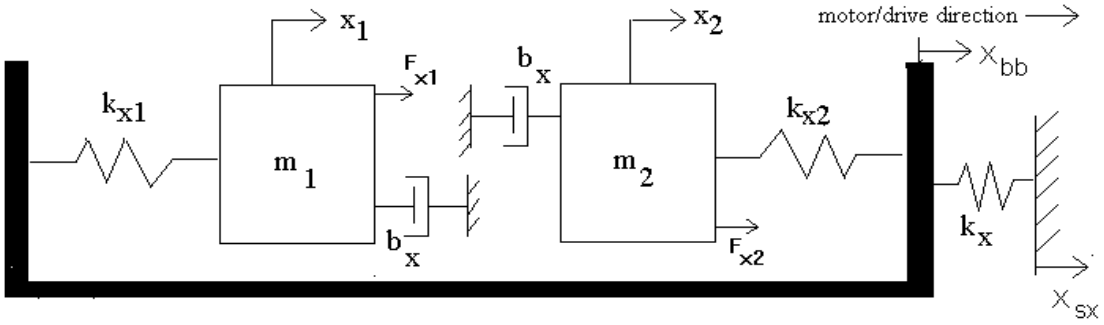

Figure A-1: Motor Axis Lumped Element Model

x_{sx} = displacement of the substrate with respect to inertial space

F_{x1} = additional force applied to left proof mass

F_{x2} = additional force applied to the right proof mass

b_x = linear dashpot between proof mass and substrate

k_{x1} = linear spring between left proof mass and basebeam

k_{x2} = linear spring between right proof mass and basebeam

k_x = linear spring between basebeam and substrate

m_1 = mass of left proof mass

m_2 = mass of right proof mass

A force balance on each mass and on the basebeam produces,

$$m_1\ddot{x}_1 = F_{x1} - k_{x1}(x_1 - x_{bb}) - b_x(\dot{x}_1 - \dot{x}_{sx}) \quad \text{(A.1)}$$

$$m_2\ddot{x}_2 = F_{x2} - k_{x2}(x_2 - x_{bb}) - b_x(\dot{x}_2 - \dot{x}_{sx}) \quad \text{(A.2)}$$

$$0 = k_x(x_{sx} - xbb) + k_{x1}(x_1 - x_{bb}) + k_{x2}(x_2 - x_{bb}) \quad \text{(A.3)}$$

Solving equation A.3 for x_{bb} produces

$$x_{bb} = \frac{k_x x_{sx} + k_{x1}x_1 + k_{x2}x_2}{k_x + k_{x2} + k_{x1}} \quad \text{(A.4)}$$

Substituting into A.1 and A.2 to eliminate x_{bb}, then rearranging to group the coefficients of x_{sx}, x_1, x_2, $\dot{x}_1$ and $\dot{x}_2$, we recover,

$$m_1\ddot{x}_1 = F_{x1} - b_x(\dot{x}_1 - \dot{x}_{sx}) - K_{x11}x_1 + K_{x12}x_2 + K_{xb1}x_{sx} \quad \text{(A.5)}$$

$$m_2\ddot{x}_2 = F_{x2} - b_x(\dot{x}_2 - \dot{x}_{sx}) - K_{x22}x_2 + K_{x21}x_1 + K_{xb2}x_{sx} \quad \text{(A.6)}$$

Where:

$$K_{x11} = \frac{k_{x1}k_x + k_{x2}k_{x1}}{k_x + k_{x1} + k_{x2}}$$

$$K_{x12} = K_{x21} = \frac{k_{x1}k_{x2}}{k_{x1} + k_{x2} + k_x}$$

$$K_{x22} = \frac{k_{x2}k_x + k_{x2}k_{x1}}{k_x + k_{x1} + k_{x2}}$$

$$K_{xb1} = \frac{k_x k_{x1}}{k_x + k_{x1} + k_{x2}}$$

$$K_{xb2} = \frac{k_x k_{x2}}{k_x + k_{x1} + k_{x2}}$$

However, it is more useful to use the relative displacements of the proof masses with respect to the substrate, since this is the quantity measured by the gyro readouts. Thus, defining new variables,

$$\begin{aligned} x_{1rel} &= x_1 - x_{sx} \\ x_{2rel} &= x_2 - x_{sx} \end{aligned} \tag{A.7}$$

and substituting back into A.5 and A.6 gives,

$$m_1\ddot{x}_{1rel} = F_{x1} - b_x\dot{x}_{1rel} - K_{x11}x_{1rel} + K_{x12}x_{2rel} - m_1\ddot{x}_{sx} \tag{A.8}$$

$$m_2\ddot{x}_{2rel} = F_{x2} - b_x\dot{x}_{2rel} - K_{x22}x_{2rel} + K_{x21}x_{1rel} - m_2\ddot{x}_{sx} \tag{A.9}$$

Where all the definitions stand as before. If we consider the forces F_{x1} and F_{x2} to be zero, as well as the acceleration of the substrate, $\ddot{x}_{sx}$, then this produces the unforced state space formulation presented as equation 2.1 of section 2.2.1, where $x_1 = x_{1rel}$ and $x_2 = x_{2rel}$ since the substrate is not allowed to translate,

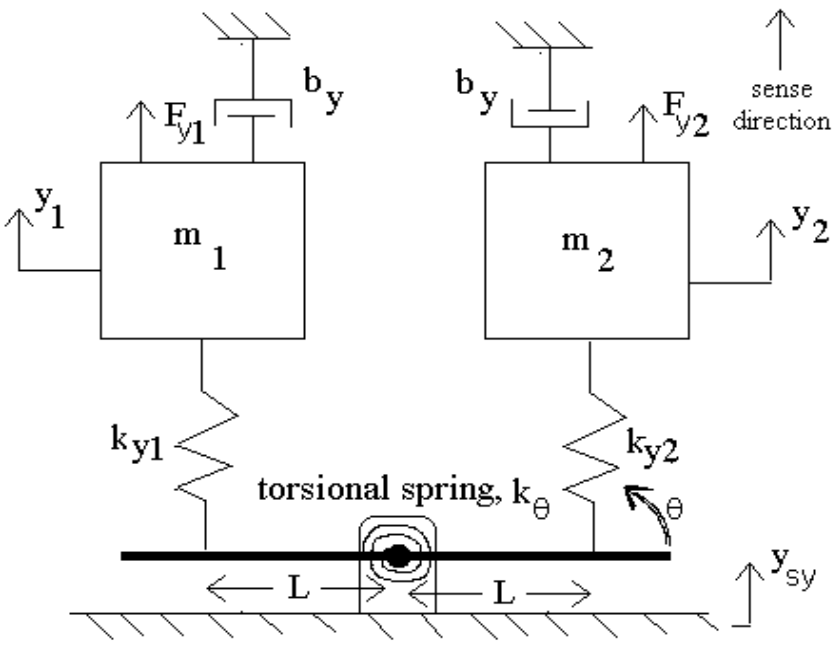

Figure A-2: Sense Axis Lumped Element Model

$$\frac{d}{dt}\begin{bmatrix} \dot{x_1} \\ x_1 \\ \dot{x_2} \\ x_2 \end{bmatrix} = \begin{bmatrix} -\frac{b_x}{m_1} & \frac{-K_{x11}}{m_1} & 0 & \frac{K_{x12}}{m_1} \\ 1 & 0 & 0 & 0 \\ 0 & \frac{K_{x21}}{m_2} & -\frac{b_x}{m_2} & \frac{-K_{x22}}{m_2} \\ 0 & 0 & 1 & 0 \end{bmatrix} \cdot \begin{bmatrix} \dot{x_1} \\ x_1 \\ \dot{x_2} \\ x_2 \end{bmatrix} \tag{A.10}$$

A.2 Sense Model

A similar derivation of the sense model is taken from the lumped element model in figure A-2.

Where

y_1 = displacement of the left proof mass out of the plane with respect to inertial space

y_2 = displacement of the right proof mass out of the plane with respect to inertial space

θ = angular displacement of the basebeam with respect to the substrate

y_{sy} = displacement of the substrate with respect to inertial space

F_{y1} = additional force applied to left proof mass

F_{y2} = additional force applied to the right proof mass

b_y = linear dashpot between proof mass and substrate

k_{y1} = linear spring between left proof mass and basebeam

k_{y2} = linear spring between right proof mass and basebeam

k_θ = torsional spring between basebeam and substrate

m_1 = mass of left proof mass

m_2 = mass of right proof mass

L = effective length of the basebeam from the center substrate anchor to the flexure

A force balance on each mass and a torque balance on the basebeam produces,

$$m_1\ddot{y}_1 = F_{y1} - k_{y1}(y_1 + \sin(\theta)L) - b_y(\dot{y}_1 - \dot{y}_{sy}) \quad \text{(A.11)}$$

$$m_2\ddot{y}_2 = F_{y2} - k_{y2}(y_2 - \sin(\theta)L) - b_y(\dot{y}_2 - \dot{y}_{sy}) \quad \text{(A.12)}$$

$$0 = -k_\theta\theta - k_{y1}L(y_1 - y_{sy} + L\sin(\theta)) + k_{y2}L(y_2 - y_{sy} - L\sin(\theta)) \quad \text{(A.13)}$$

If we assume θ is small, and make the approximation $\sin(\theta) \approx \theta$, and then solve equation A.13 for θ, we produce

$$\theta = -L\frac{k_{y1}(y_1 - y_{sy}) - k_{y2}(y_2 - ysy)}{k_\theta + L^2k_{y1} + L^2k_{y2}} \quad \text{(A.14)}$$

Substituting into A.11 and A.12 to eliminate θ, then rearranging to group the coefficients of y_{sy}, y_1, y_2, $\dot{y}_1$ and $\dot{y}_2$, we recover,

$$m_1\ddot{y}_1 = F_{y1} - b_y(\dot{y}_1 - \dot{y}_{sy}) - K_{y11}y_1 + K_{y12}y_2 + K_{yb1}y_{sy} \quad (A.15)$$

$$m_2\ddot{y}_2 = F_{y2} - b_y(\dot{y}_2 - \dot{y}_{sy}) - K_{y22}y_2 + K_{y21}y_1 + K_{yb2}y_{sy} \quad (A.16)$$

Where:

$K_{y11} = \frac{k_{y1}k_\theta + L^2k_{y1}k_{y2}}{k_\theta + L^2(k_{y1}+k_{y2})}$

$K_{y12} = K_{y21} = \frac{-L^2k_{y1}k_{y2}}{k_\theta + L^2k_{y1} + L^2k_{y2}}$

$K_{y22} = \frac{k_{y2}k_\theta + L^2k_{y2}k_{y1}}{k_\theta + L^2(k_{y1}+k_{y2})}$

$K_{yb1} = \frac{k_{y1}k_\theta + 2L^2k_{y1}k_{y2}}{k_\theta + L^2k_{y1} + L^2k_{y2}}$

$K_{yb2} = \frac{k_{y2}k_\theta + 2L^2k_{y1}k_{y2}}{k_\theta + L^2k_{y1} + L^2k_{y2}}$

Again, it is more useful to use the relative displacements of the proof masses with respect to the substrate, since this is the quantity measured by the gyro readouts. Thus, defining new variables,

$$\begin{aligned} y_{1rel} &= y_1 - y_{sy} \\ y_{2rel} &= y_2 - y_{sy} \end{aligned} \quad (A.17)$$

and substituting back into A.15 and A.16 gives,

$$m_1\ddot{y}_{1rel} = F_{y1} - b_y\dot{y}_{1rel} - K_{y11}y_{1rel} + K_{y12}y_{2rel} - m_1\ddot{y}_{sy} \quad (A.18)$$

$$m_2\ddot{y}_{2rel} = F_{y2} - b_y\dot{y}_{2rel} - K_{y22}y_{2rel} + K_{y21}y_{1rel} - m_2\ddot{y}_{sy} \quad (A.19)$$

Where all the definitions stand as before. If we consider the forces F_{y1} and F_{y2} to be zero, as well as the acceleration of the substrate, $\ddot{y}_{sy}$, then this produces the

unforced state space formulation presented as equation 2.2 of section 2.2.1, where $y_1 = y_{1rel}$ and $y_2 = y_{2rel}$ since the substrate is not allowed to translate,

$$\frac{d}{dt}\begin{bmatrix} \dot{y_1} \\ y_1 \\ \dot{y_2} \\ y_2 \end{bmatrix} = \begin{bmatrix} -\frac{b_y}{m_1} & \frac{-K_{y11}}{m_1} & 0 & \frac{K_{y12}}{m_1} \\ 1 & 0 & 0 & 0 \\ 0 & \frac{K_{y21}}{m_2} & -\frac{b_y}{m_2} & \frac{-K_{y22}}{m_2} \\ 0 & 0 & 1 & 0 \end{bmatrix} \cdot \begin{bmatrix} \dot{y_1} \\ y_1 \\ \dot{y_2} \\ y_2 \end{bmatrix} \tag{A.20}$$

A.3 Combined Model

The two axis model is a combination of these two models in equations A.10 and A.20, adding in crosscoupling terms k_{xy} and b_{xy}, and considering the forces F_{x1},F_{x2},F_{y1}, F_{y2}, and accelerations $A_{coriolis}$,$a_{xs} = \ddot{x}_{sx}$ and $a_{ys} = \ddot{y}_{sy}$ as inputs. The Coriolis acceleration, $A_{coriolis}$ is an acceleration in the frame of the gyro produced by rotation of the frame with respect to inertial space. See section 2.2.3. This produces the full linear model used in this thesis, as described in section 2.2.4.

$$\frac{d}{dt}\begin{bmatrix} \dot{x}_{1rel} \\ x_{1rel} \\ \dot{x}_{2rel} \\ x_{2rel} \\ \dot{y}_{1rel} \\ y_{1rel} \\ \dot{y}_{2rel} \\ y_{2rel} \end{bmatrix} = [A] \cdot \begin{bmatrix} \dot{x}_{1rel} \\ x_{1rel} \\ \dot{x}_{2rel} \\ x_{2rel} \\ \dot{y}_{1rel} \\ y_{1rel} \\ \dot{y}_{2rel} \\ y_{2rel} \end{bmatrix} + [B] \cdot \begin{bmatrix} a_{xs} \\ a_{ys} \\ F_{x1} \\ F_{x2} \\ F_{y1} \\ F_{y2} \\ A_{Coriolis} \end{bmatrix} \tag{A.21}$$

Where A is the system matrix, given in equation A.22, and B is the input matrix, given in equation A.23.

$$A = \left[\begin{array}{cccc|cccc} -\frac{b_x}{m_1} & \frac{-K_{x11}}{m_1} & 0 & \frac{K_{x12}}{m_1} & \frac{b_{xy1}}{m_1} & \frac{k_{xy1}}{m_1} & 0 & 0 \\ 1 & 0 & 0 & 0 & 0 & 0 & 0 & 0 \\ 0 & \frac{K_{x21}}{m_2} & -\frac{b_x}{m_2} & \frac{-K_{x22}}{m_2} & 0 & 0 & \frac{b_{xy2}}{m_2} & \frac{k_{xy2}}{m_2} \\ 0 & 0 & 1 & 0 & 0 & 0 & 0 & 0 \\ \hline \frac{b_{xy1}}{m_1} & \frac{k_{xy1}}{m_1} & 0 & 0 & -\frac{b_y}{m_1} & \frac{-K_{y11}}{m_1} & 0 & \frac{K_{y12}}{m_1} \\ 0 & 0 & 0 & 0 & 1 & 0 & 0 & 0 \\ 0 & 0 & \frac{b_{xy2}}{m_2} & \frac{k_{xy2}}{m_2} & 0 & \frac{K_{y21}}{m_2} & -\frac{b_y}{m_2} & \frac{-K_{y22}}{m_2} \\ 0 & 0 & 0 & 0 & 0 & 0 & 1 & 0 \end{array}\right] \tag{A.22}$$

And the input matrix,

$$B = \begin{bmatrix} -1 & 0 & \frac{1}{m_1} & 0 & 0 & 0 & 0 \\ 0 & 0 & 0 & 0 & 0 & 0 & 0 \\ -1 & 0 & 0 & \frac{1}{m_2} & 0 & 0 & 0 \\ 0 & 0 & 0 & 0 & 0 & 0 & 0 \\ 0 & -1 & 0 & 0 & \frac{1}{m_1} & 0 & 1 \\ 0 & 0 & 0 & 0 & 0 & 0 & 0 \\ 0 & -1 & 0 & 0 & 0 & \frac{1}{m_2} & -1 \\ 0 & 0 & 0 & 0 & 0 & 0 & 0 \end{bmatrix} \tag{A.23}$$

Section 2.2.4 also gives some transfer functions relating the relative displacement of a single mass in a single direction to a particular input. The simplified cases of matched springs $K_{x11} = K_{x22}$, etc. and matched masses $m_1 = m_2$ are also considered there. Section 2.2.2 derives the normal modes of the system, and gives relationships allowing the determination of the various spring constants from the experimentally measured modal frequencies.

Appendix B

Mechanical Drawings

The mechanical drawings used for construction of the vibration fixtures are presented here. This includes the overhung fixture, the sense fixture, the adapter plate used for attaching to the Labworks electromagnetic shaker, the clamping plate, and the TFG cover. These were the final iterations of a process which went through the construction of 3 sets of fixturing.

B.1 Overhung Fixture

The overhung fixture is used for motor directed vibration delivered by the piezoshaker.

B.2 Sense Fixture

The sense fixture, along with the baseplate adapter, allows sense axis vibration to be delivered by the piezoshaker. It also bolts directly to the electromagnetic shaker for low frequency sense directed vibration. Two mounting brackets allow 90 degree rotation on the electromagnetic shaker for delivery of low frequency motor directed vibration.

Mechancial drawings of the sense fixture are unavailable.

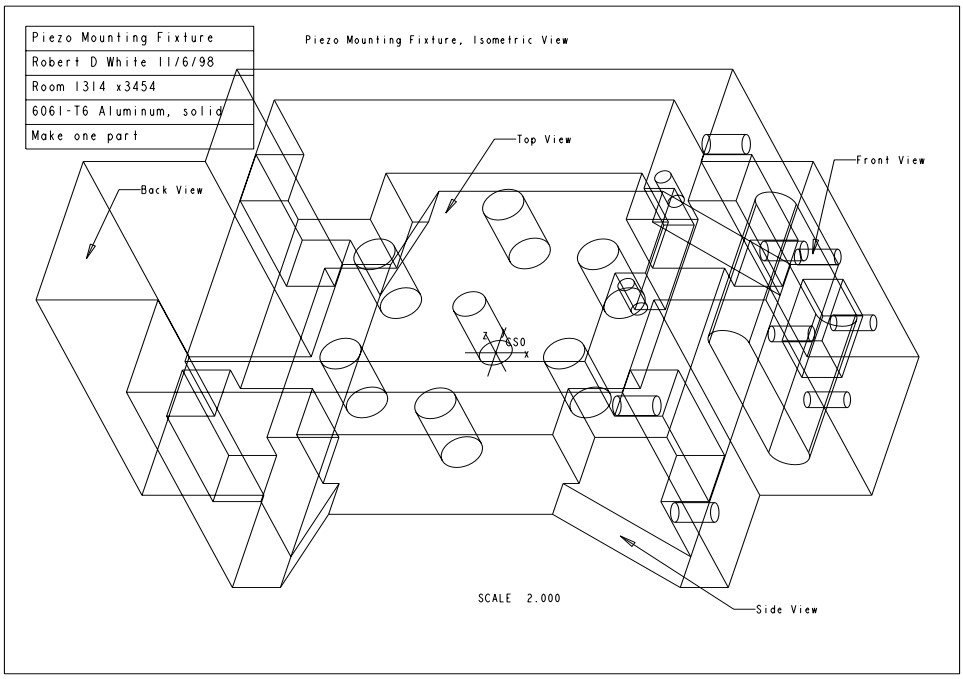
Piezo Mounting Fixture
Robert D White 11/6/98
Room 1314 x3454
6061-T6 Aluminum, solid
Make one part
Piezo Mounting Fixture, Isometric View
Top View
Front View
Back View
CS0
SCALE 2.000
Side View

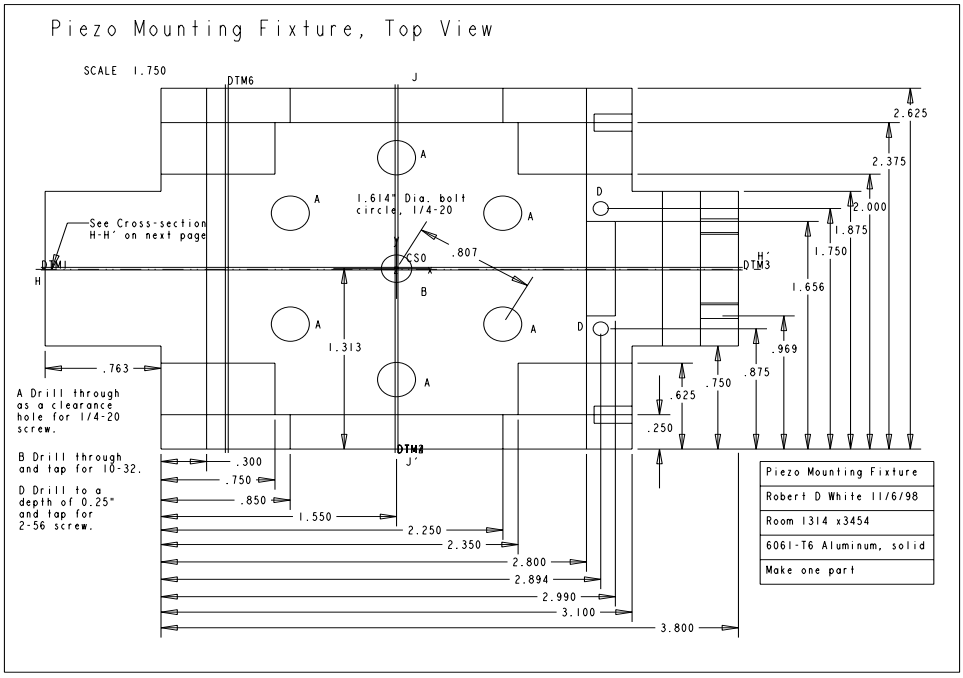
Piezo Mounting Fixture, Top View
SCALE 1.750
DTM6
J
2.625
2.375
2.000
1.875
1.750
1.656
.969
.875
.750
.625
.250
A
D
1.6141 Dia. bolt circle, 1/4-20
See Cross-section H-H' on next page
CS0
.807
B
DTM1
DTM3
H
H'
1.313
.763
A Drill through as a clearance hole for 1/4-20 screw.
B Drill through and tap for 10-32.
D Drill to a depth of 0.25" and tap for 2-56 screw.
DTM2
J'
.300
.750
.850
1.550
2.250
2.350
2.800
2.894
2.990
3.100
3.800
Piezo Mounting Fixture
Robert D White 11/6/98
Room 1314 x3454
6061-T6 Aluminum, solid
Make one part

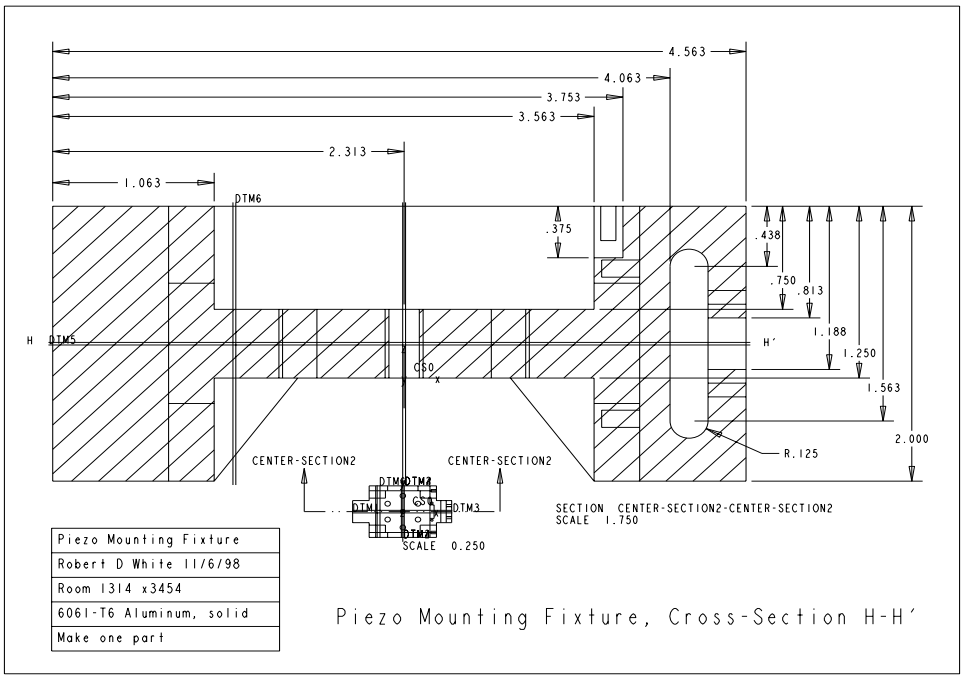
4.563
4.063
3.753
3.563
2.313
1.063
DTM6
.375
.438
.750
.813
1.188
1.250
1.563
2.000
H
DTM5
H'
CS0
x
R.125
CENTER-SECTION2
CENTER-SECTION2
DTM4
DTM2
DTM1
DTM3
SECTION CENTER-SECTION2-CENTER-SECTION2
SCALE 1.750
SCALE 0.250
Piezo Mounting Fixture
Robert D White 11/6/98
Room 1314 x3454
6061-T6 Aluminum, solid
Make one part
Piezo Mounting Fixture, Cross-Section H-H'

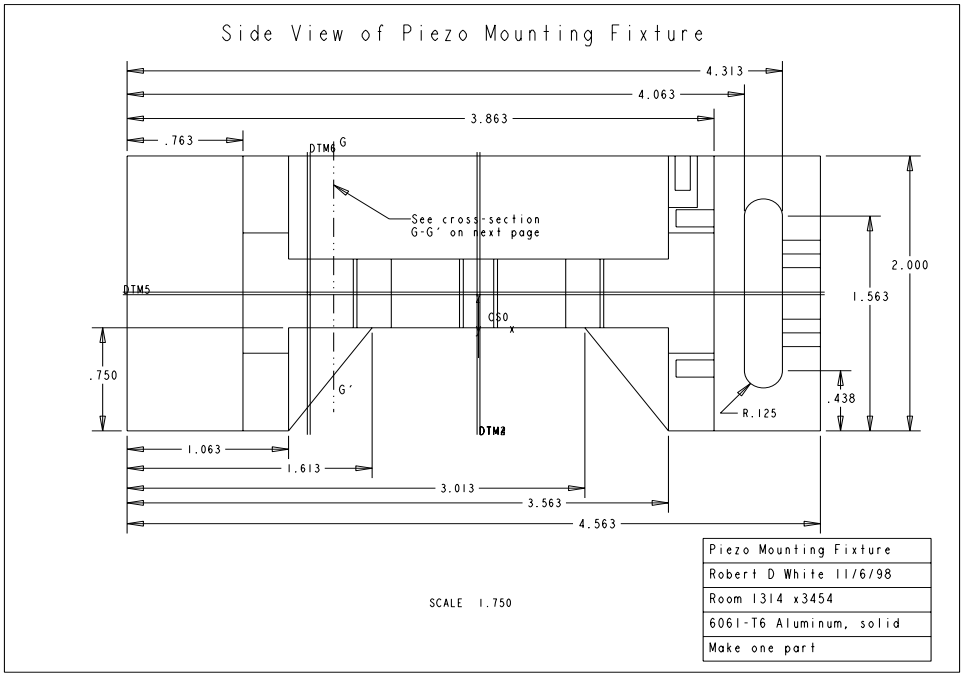
Side View of Piezo Mounting Fixture
4.313
4.063
3.863
.763
DTM6
G
See cross-section
G-G' on next page
2.000
1.563
DTM5
CS0
x
.750
G'
.438
R.125
DTM2
1.063
1.613
3.013
3.563
4.563
SCALE 1.750
Piezo Mounting Fixture
Robert D White 11/6/98
Room 1314 x3454
6061-T6 Aluminum, solid
Make one part

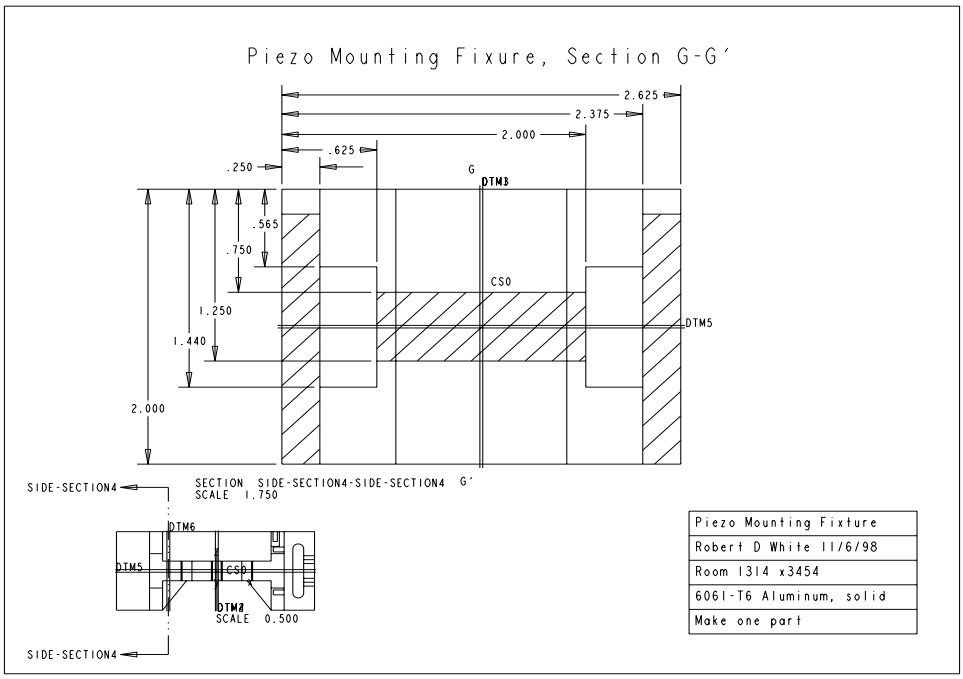
Piezo Mounting Fixure, Section G-G´
2.625
2.375
2.000
.625
.250
G
DTM3
.565
.750
CS0
1.250
DTM5
1.440
2.000
SIDE-SECTION4
SECTION SIDE-SECTION4-SIDE-SECTION4 G´
SCALE 1.750
DTM6
DTM5
CS0
DTM3
SCALE 0.500
SIDE-SECTION4
Piezo Mounting Fixture
Robert D White 11/6/98
Room 1314 x3454
6061-T6 Aluminum, solid
Make one part

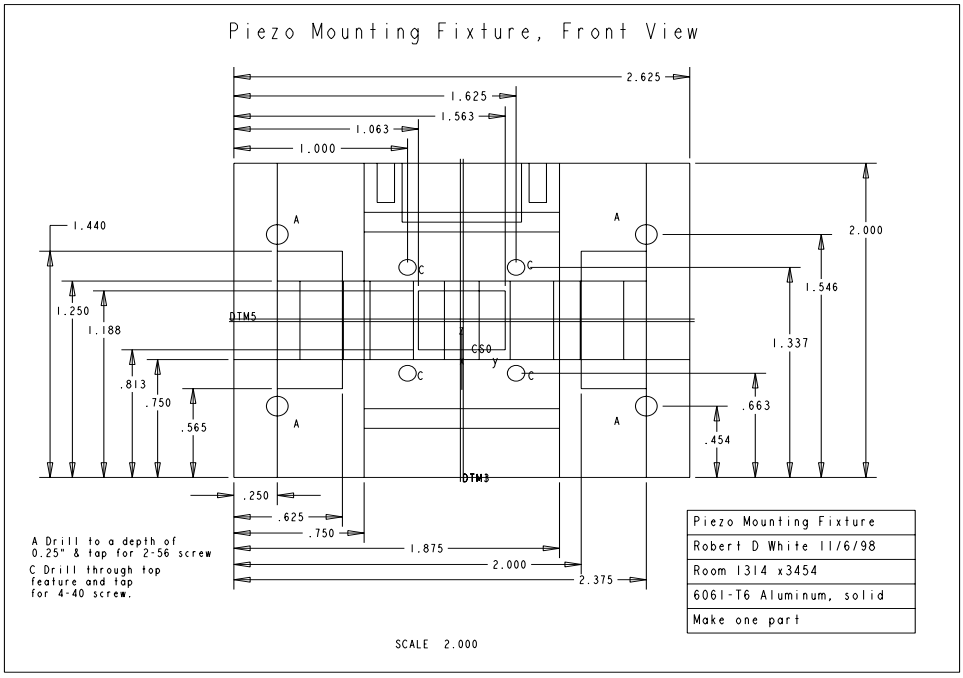
Piezo Mounting Fixture, Front View
2.625
1.625
1.563
1.063
1.000
1.440
A
A
2.000
C
C
1.546
1.250
1.188
DTM5
CS0
y
1.337
.813
.750
.565
C
C
.663
A
A
.454
DTM3
.250
.625
.750
1.875
2.000
2.375
A Drill to a depth of 0.25" & tap for 2-56 screw
C Drill through top feature and tap for 4-40 screw.
SCALE 2.000
Piezo Mounting Fixture
Robert D White 11/6/98
Room 1314 x3454
6061-T6 Aluminum, solid
Make one part

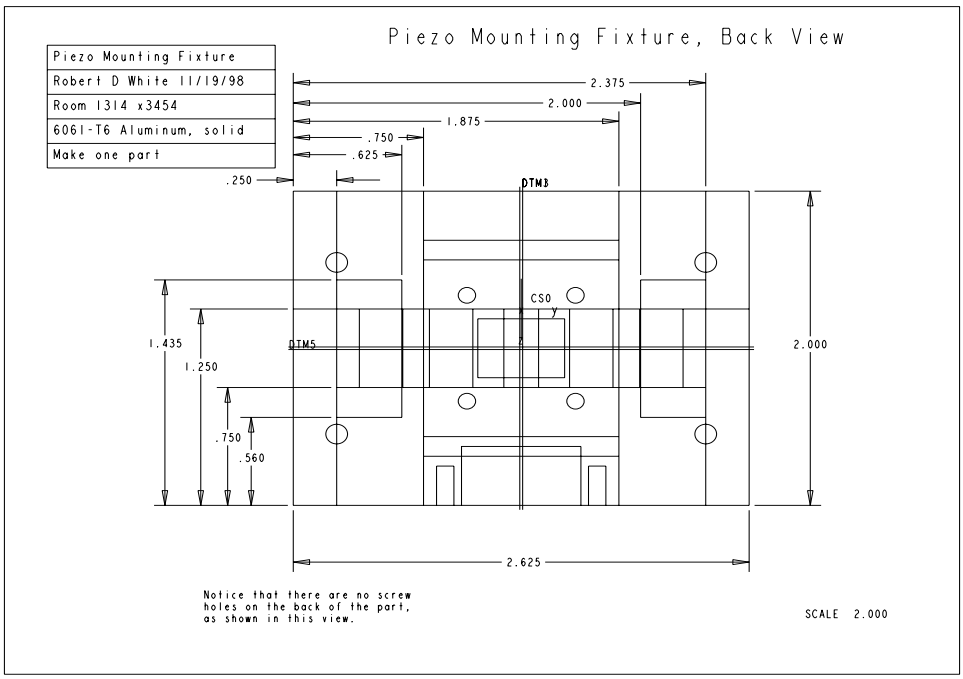

B.3 Baseplate Adapter

This baseplate allows the sense axis fixture to mate with the bolt pattern on the piezoshaker; the sense fixture bolt pattern mates directly with the electromagnetic shaker.

Baseplate, Rev 3

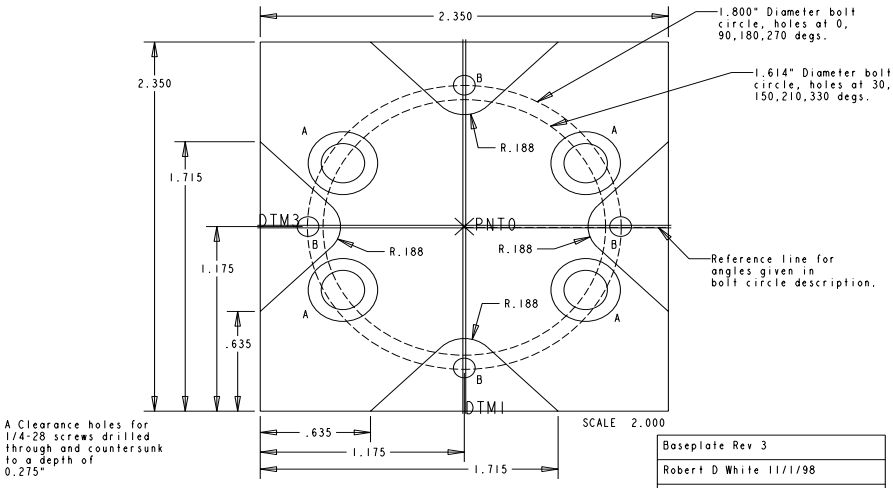

A Clearance holes for 1/4-28 screws drilled through and countersunk to a depth of 0.275"

B Holes drilled and tapped for 6-32 screws. Through.

Build from 0.75" thick plate

Baseplate Rev 3
Robert D White 11/1/98
Room 1314 x3454
6061-T6 Aluminum, solid
Make one part

Baseplate, Rev 3, Side View

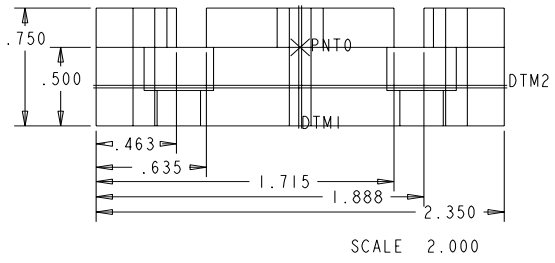

Baseplate, Rev 3
Robert D White 11/1/98
Room 1314 x3454
6061-T6 Aluminum, solid
Make one part

Baseplate, Rev 3. Isometric View

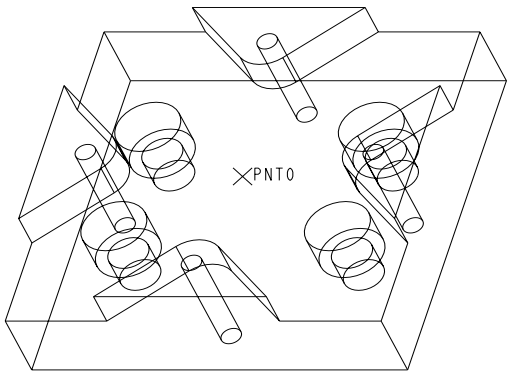

SCALE 2.000

Baseplate, Rev3
Robert D White 11/1/98
Room 1314 x3454
6061-T6 Aluminum, solid
Make one part

Appendix C

Matlab Models

The modeling results used throughout were often generated using the matlab systems toolbox. This toolbox allows manipulation of linear models described in state-space or transfer function form. The m-file listed below creates a state-space model representing the mechanical gyro system derived in section 2.2.1. The user fills in system parameters such as modal frequencies and Q, depending on the unit being modeled.

```
%This m-file constructs a SS model for the entire TFG system.
%The model is of two masses each with a motor and sense
%motion allowed, connected via translational springs to a rigid
%basebeam which connects to the substrate via a third spring
%with both translational and rotational stiffness.
%It linearizes everything, including the readout electronics,
%which do not include any feedback effects.
%The electrostatic spring is currently not taken into account
%Parameters estimated from some physical
%dimensions and also from data.

%****Approximate values for system parameters, user must supply****
```

```
%Masses
mass_mismatch=0;        %Fractional mismatch in the masses
mbar=3.6e-8;            %Average mass of proof masses (kg). Nominal TFG14

%Flexure springs
y_spring_mismatch=0.0;  %Fractional mismatch in the sense springs
x_spring_mismatch=0.0;  %Fractional mismatch in the motor springs

%Q
Qmotor=157000;   %Motor Q (measurements available for each unit)
Qsense=12000;    %Sense Q  "

%Frequencies
fhula=13035;     %Hula Frequency (Hz) (measurements available)
ftunefork=14250; %Tuning fork frequency (Hz) (measurements available)
fsense=15556;    %Sense frequency (Hz)                  "
foop=17352;      %Out of plane frequency (Hz)  "

%Crosscoupling
kxy1=0;          %Coupling between sense and motor, left proof mass (N/m)
kxy2=kxy1;       %Coupling between sense and motor, left proof mass (N/m)
bxy1=0;          %Surfboarding coupling  (In-phase)
bxy2=bxy1;


%Biasing and electronic components
%Sense:
Vs1=-5.0;        %Voltage on left sense plate (V)
Vs2=0;           %Voltage on right sense plate (V)
Cs1=2.64e-12;    %Left sense capacitance (F) (Measurements available
```

```
                %for each unit)
Csr=2.70e-12;   %Right sense capacitance (F) (Measurements available
                %for each unit)
y0=2.8E-6;      %Nominal sense gap. (m) Typical TFG14From Marc
Csf=1.8889E-12; %Sense preamp feedback capacitance. (F) (Measured
                %available)
Gs=-1;          %Gain of any additional gain stages before output is
                %read.

%Motor:
Vil=-5.0;       %Voltage on left inner motor comb
Vir=5.0;        %Voltage on right inner comb
Vol=0;          %Voltage on left outer comb
Vor=0;          %Voltage on right outer comb
Cil=0.42e-12;   %Nominal left inner motor capacitance (F) Taken from
                %outer motor cap measurements on LCCC575
Cir_mismatch=0; %capacitor mismatches from left inner motor for all
                %motor caps.
Col_mismatch=0;
Cor_mismatch=0;
Cmf=1.83E-12;   %Motor preamp feedback capacitance. (F) Measured LCCC490
Gm=-10;         %Gain of any additional gain stages before output is
                %read.
SFmotor=0.0366e6;%Motor scale factor (V/m)


%****End of user supplied constants****

%Mass
m1=2*mbar/(2+mass_mismatch);    %Mass of left proof mass. (kg)
```

```
m2=m1*(1+mass_mismatch);        %Mass of right proof mass. (kg)


%Spring computations
kybar=4*(foop^2)*(pi^2)*mbar;           %Average sense flexure (N/m)
ky1=2*kybar/(2+y_spring_mismatch);      %sense flexure for left proof
                                        %mass. (N/m)
ky2=ky1*(1+y_spring_mismatch);          %sense flexure for right proof
                                        %mass. (N/m)

kxbar=mbar*4*(pi^2)*(ftunefork^2);      %average motor flexure
                                        %stiffness  (N/m)
kx1=2*kxbar/(2+x_spring_mismatch);      %left motor flexure (N/m)
kx2=kx1*(1+x_spring_mismatch);          %Right motor flexure (N/m)


%Damping
by=sqrt(kybar*mbar)/Qsense;             %Sense axis
                                        %damping. (N*s/m)Computed to
                                        %get correct sense Q
bx=sqrt(kxbar*mbar)/Qmotor;             %Motor
                                        %damping. (N*s/m)Computed to
                                        %produce correct motor Q.

%Basebeam to substrate stiffness
%Basebeam to substrate motor axis spring (N/m) computed to get fhula
kxb=((8*(pi*fhula)^2)*mbar)/(1-((2*fhula*pi)^2)*mbar/kxbar);

%Basebeam to substrate torsional spring (N*m/radian) computed to get
%fsense
```

```
P=(1/8)*((foop^2)-(fsense^2))/((foop^4)*((pi^2)*mbar));

%Computations of openloop readout scalefactors:

motor_il=SFmotor*Cmf/5;              %Linearized dC/dx about no
                                     %deflection from motor equilibrium
                                     %(F/m)
                                     %Computed based on nominal TFG 5 V
                                     %inner motor bias and V/m SF
motor_ol=motor_il*(1+Col_mismatch); %Outer left motor cap scaling (F/m)
motor_or=motor_il*(1+Cor_mismatch); %Outer left motor cap scaling (F/m)
motor_ir=motor_il*(1+Cir_mismatch); %Outer left motor cap scaling (F/m)

lin_sense_SF_left=(-Csl)/(y0);       %Linearized dC/dx for left sense
                                     %about no deflection from nominal
                                     %gap (F/m).
lin_sense_SF_right=(-Csr)/(y0);      %Linearized dC/dx for right sense
                                     %about no deflection from nominal
                                     %gap (F/m).

Klm=motor_ol*0.5;                    %Left motor force/volt^2 constant
                                     %(N/V^2)
Krm=motor_or*0.5;                    %Right motor force/volt^2 constant
                                     %(N/V^2)


%Computations of stiffnesses to go in the state matrix:
%Motor axis:
Kx11=kx1*(1-(kx1/(kxb+kx1+kx2))); Kx22=kx2*(1-(kx2/(kxb+kx1+kx2)));
Kx12=kx2*kx1/(kx1+kx2+kxb); Kx21=Kx12; Kx1b=kxb*kx1/(kx1+kx2+kxb);
```

```
Kx2b=kxb*kx2/(kx1+kx2+kxb);

%Sense axis:
Ky11=ky1*(1-P*ky1); Ky22=ky2*(1-P*ky2); Ky12=-ky1*ky2*P; Ky21=Ky12;
Ky1b=ky1; Ky2b=ky2;

%State variables:Motor velocity of left mass, motor position of left mass,
%Motor velocity of right mass , motor position of right mass,
%sense velocity of left mass, sense position of left mass,
%sense velocity of right mass , sense position of right mass, motor velocity
%of substrate, motor position of substrate, sense velocity of substrate
%sense position of substrate

A=[ -bx/m1 -Kx11/m1 0 Kx12/m1 bxy1/m1 kxy1/m1 0 0 bx/m1 Kx1b/m1 0 0; 1
        0 0 0 0 0 0 0 0 0 0 0; 0 Kx21/m2 -bx/m2 -Kx22/m2 0 0 bxy2/m2
        kxy2/m2 bx/m2 Kx2b/m2 0 0; 0 0 1 0 0 0 0 0 0 0 0 0; bxy1/m1
        kxy1/m1 0 0 -by/m1 -Ky11/m1 0 Ky12/m1 0 0 by/m1 Ky1b/m1; 0 0 0
        0 1 0 0 0 0 0 0 0; 0 0 bxy2/m2 kxy2/m2 0 Ky21/m2 -by/m2
        -Ky22/m2 0 0 by/m2 Ky2b/m2; 0 0 0 0 0 0 1 0 0 0 0 0; 0 0 0 0 0
        0 0 0 0 0 0 0 0; 0 0 0 0 0 0 0 0 1 0 0 0; 0 0 0 0 0 0 0 0 0 0 0
        0; 0 0 0 0 0 0 0 0 0 0 1 0;];

%Inputs: Acceleration of substrate in motor direction, acceleration
%of substrate in sense direction, %voltage squared on left drive,
%voltage squared on right drive, additional motor forces on left mass,
%additional motor forces on right mass,additional sense forces on left
%mass, additional sense forces %on right mass, coriolis
%forces.... these will be in Newtons, acting on %both masses in the
%sense direction in opposite directions
```

```
 B=[0 0 -Klm/m1 0 1/m1 0 0 0 0; 0 0 0 0 0 0 0 0 0; 0 0 0 Krm/m2 0 1/m2
   0 0 0; 0 0 0 0 0 0 0 0 0; 0 0 0 0 0 0 1/m1 0 1/m1; 0 0 0 0 0 0 0 0
   0; 0 0 0 0 0 0 0 1/m2 -1/m2; 0 0 0 0 0 0 0 0 0; 1 0 0 0 0 0 0 0 0;
   0 0 0 0 0 0 0 0 0; 0 1 0 0 0 0 0 0 0; 0 0 0 0 0 0 0 0 0;];

%Outputs:Left mass motor position, right mass motor position, left mass ...
%    sense position, right mass sense position, motor_outx10, sense_out,
%    relative left mass motor displacement (relative to substrate), relative
%    left mass sense displacement
C=[0 1 0 0 0 0 0 0 0 0 0; 0 0 0 1 0 0 0 0 0 0 0; 0 0 0 0 0 1 0 0 0
   0 0 0; 0 0 0 0 0 0 0 1 0 0 0 0; 0 Gm*motor_il*Vil/Cmf 0 0 0 0 0 0 0
   (-1*Gm*motor_il*Vil/Cmf) 0 0; 0 Gs*(-motor_il*Vil+motor_ol*Vol)/Csf
   0 Gs*(motor_ir*Vir-motor_or*Vor)/Csf 0 Gs*lin_sense_SF_left*Vs1/Csf
   0 Gs*lin_sense_SF_right*Vs2/Csf 0
   -Gs*(((-motor_il*Vil+motor_ol*Vol)/Csf)+((motor_ir*Vir-motor_or*Vor)/Csf))
   0
   (-1*Gs*lin_sense_SF_left*Vs1/Csf)+(-1*Gs*lin_sense_SF_right*Vs2/Csf);
   0 1 0 0 0 0 0 0 0 -1 0 0; 0 0 0 0 0 1 0 0 0 0 0 -1; ];

D=zeros(8,9);  %Note that I am *not* taking into account
%charge injection from the motor drive signal

sys=ss(A,B,C,D); disp('System defined')
```

Bibliography

[1] Stephen A. Campbell. *The Science and Engineering of Microelectronic Fabrication.* Oxford University Press, New York, 1996.

[2] Halliday, Resnick, and Krane. *Physics: 4th Edition.* John Wiley and Sons, Inc., New York, 1992.

[3] J.Bernstein, S. Cho, A. T. King, A. Kourepenis, P. Maciel, and M. Weinberg. A micromachined comb-drive tuning fork rate gyroscope. *IEEE Micro Electro Mechanical Systems, Proceedings of the 1993 IEEE Micro Electro Mechanical Systems - MEMS*, Feb 1993.

[4] Marc Madou. *Fundamentals of Microfabrication.* CRC Press, Boca Raton, Fla., 1997.

[5] Katsuhiko Ogata. *Modern Control Engineering, 3rd Edition.* Prentice Hall, Inc., New Jersey, 1997.

[6] Andrei Shkel, Roberto Horowitz, Ashwin A. Seshia, Sungsu Park, and Roger T. Howe. Dynamics and control of micromachined gyroscopes. *The American Control Conference*, June 1999.

[7] James H. Jr. Williams. *Fundamentals of Applied Dynamics.* John Wiley and Sons, Inc., New York, 1996.